Combined Theoretical and Experimental Studies of Proton Migration and Transfer in the Solid State

David Manuel Silva Martins

Doctor *of* Philosophy

The University *of* Edinburgh

2008

Declaration

This thesis has not been previously submitted, in whole or in part, for any degree at this or any other university. The work is original and my own, carried out under the supervision of Dr. Carole A. Morrison and Dr. Colin R. Pulham; where this is not so, credit has been duly given.

David Martins

Acknowledgments

I would like to thank my supervisors Carole, Colin and Chick first and foremost for giving me this fantastic opportunity. Secondly, for their supervision, drive and what seamed at some times endless knowledge. Finally, I would also like to thank them for all the English and structural writing lessons.

An enormous thanks must also go to Martin, Chris, Alistair, Patty, Dell, Francesca, Iain, Phil, Stuart, Anthony, Rob, Sarah, Derek, Tom, Kay, Andy, Lynsey/Ana and Costas Millios for their help with calculations and experiments, helpful discussions, general banter and laughs! Of these, I would like to specially thank Martin and Phil for being true comrades in times of need, *i.e.* in Cardiff when they took on the less hygienic hands and not to forget the conference haircuts, which I think Phil still has one in him ;)

I would also like to thank my office mates and the folk from the CSEC open plan office for the helpful discussions and help with everyday problems. In particular Dario for the chocolate cheesecake that fuelled the last day/nigh/day of writing.

A bit shout goes out to the various people that I had the benefit and pleasure to have collaborated with directly during the research undertaken for the production of this thesis. A special thanks has to go out to Norman Shankland for introducing me to *Old Speckled Hen* pies and other precious gems ;)

"Mano"[1] Denny and Patricia were simply IMENSE for the fact they worked as a bridge [*i.e.* H atom along a SSSHB (super short, strong hydrogen bond) in order to keep it scientific] between myself and everything that I was missing. So just want you to know that a place in my heart will forever belong to you.

Other friends that made living abroad something manageable but so hard at the same were: Jaime, "Maninha"[2] Diana, Suzana, Rita Canas and Catinha so to them I am thankful. The other six in "Os sete maravilha"[3] – Malino, Petrucci, Cartaxo, Gê Hugo, Gê Nuno and João Vasco also find a place here because with them I had the tremendous pleasure of seeing/meeting Croacia, Dona Wilma (and the never ending 2nd gear), William Wallace, freshly brewed Guinness, etc… :P

To the members of my "tuna"[4], the grand DESERTUNA, I would like to say that I am very proud of what you have been achieving and would like to thank for all the laughter and music that has helped me quite a lot.

Georgios the crazy'esk Greek that when I met and after knowing where I was from just couldn't stop saying "EURO2004 … you were a very good host nation…"…Anyways in the end he is not that bad of a guy and turned out to be quite a good flatmate :P

Sega the crazy'esk Italian that can't get enough of blues and other things… And that in the writing stage made some really nice cheesy bites pizza that enabled me to keep going into the night…

Pinto and Eduardo showed in the last stretch… and I mean LAST and LONG stretch… A sense of true friendship that I hope to repay and for sure will never forget. By the way guys I think I know what I should do after this, open a pizza place that doesn't close ;)

[1] Bro
[2] Little sister
[3] Literally 'The seven wonder' but probably better translated as 'The Magnificent Seven'
[4] Academic orchestra although this translation does not do it justice

Nardão, that although only came to visit for a year, has become a good friend that I really hope to get the chance to see again many times. To him I thank for putting up with all my mumbling about the joys of writing and for teaching me general chemical and Brazilian knowledge.

Bea, Pedro, Fifi, João, Espe, Eli, Mridul and Samira were some of the people that I very much enjoyed meeting during my stay in the British Isles and that I found to be good friends, so I will for ever associate this time with them.

Most importantly my whole family for being… well… themselves really! In particular the people that I most love in the world and without whom I would neither be the person that they taught me to be nor this thesis would be finished. These are my mom - Lucinda, dad – Manuel, sister – Monica and "avós"[5] – Joaquim, Lucinda, Teresa, Angelina and Francisco (who unfortunately passed away during this PhD. I believe he was a great man and I know that he has never stopped looking out for me). To them I send a big kiss.

To all of you I hope that our roads keep crossing for many years. Furthermore, I think the best way to end would be using words that I found to mean so much to me when I was studying in my university in a corner of Portugal (UBI[6]) which were:

To all

"Bem Haja"[7]

[5] Grandparents
[6] Universidade da Beira Interior, Covilhã, Portugal
[7] Literally would mean 'Well there' but probably better translated as 'Wishing you the best'

"*If I have seen further than others, it is by standing upon the shoulders of giants.*"

Sir Isaac Newton

To my grandparent, parents and sister…

Francisco Martins, Angelina Martins, Joaquim Silva, Lucinda Silva, Teresa Rodrigues, Lucinda Martins, Manuel Martins and Monica Santarem

Abstract

Hydrogen bonds are of great interest in the solid state due to their importance in structural, functional and dynamical properties of chemical systems. Moderate hydrogen bonds have been linked with proton transfer, whereas the short, strong hydrogen bonds enable proton migration.

Previous work in our group on relatively simple hydrogen bonded adducts relied on the combination of *ab initio* computational modelling (molecular dynamics) with variable temperature diffraction results (X-ray and neutron). These demonstrated that the interplay of these techniques was successful in studying the phenomena of proton transfer and migration.

The present work follows on from that, and focuses on the effects of temperature and pressure on proton transfer and migration using both experimental and computational methods. The systems studied continue to encapsulate adducts with N···O and O···O hydrogen bonds.

The study of the adduct formed between squaric acid and 4,4'-bipyridine was found to exhibit proton transfer associated with a single-crystal to single-crystal phase transition at 450 K that is coupled to a colour change (yellow to red). X-ray and neutron diffraction initially revealed the heavy atom structure and secondly the location of the hydrogen atoms along the moderate N···O hydrogen bond (*ca.* 2.6 Å). Computational modelling supported this and deduced the reason for the striking colour change. Pressure studies also determined that the adduct underwent two phase-transitions with a similar colour change, indicating that proton transfer is also

a factor here, but with powder patterns different from the high temperature form, indicating that further polymorphs for this interesting system must exist.

In an attempt to lower the temperature at which proton transfer would occur the base was changed to one of a more basic nature, *i.e.* co-crystallisation of squaric acid and 2,2'-dimethyl–4,4'-bipyridine was pursued. This lead to the formation of two red crystals that were found to posses the base doubly protonated at all temperatures studied (from 300 K to 100 K).

The adduct of N,N-dimethylurea with phosphoric acid was obtained from a systematic study designed to follow the success of a previously reported system that showed proton migration (the adduct of urea and phosphoric acid). The new material was found to crystallise as the 2:1 adduct and maintained the short, strong hydrogen bonds characteristic of the parent structure.

As part of the systematic approach undertaken throughout the research presented here, co-crystallisation of a combination of acids and bases were attempted in order to synthesise new materials containing short, strong hydrogen bonds. These yielded the adducts between oxalic acid and 2,2'-dimethyl-4,4'-bipyridine, and oxamic acid and 4,4'-bipyridine. In addition to these adducts some compounds ended up reacting to create new ones, *e.g.* the fusing of dimethyl urea and squaric acid to give N-(2-hydroxycyclobutene-3,4-dione)-N',N'-dimethylurea and N-(2-hydroxycyclobutene-3,4-dione)-N,N'-dimethylurea, while a new polymorphs of one of the precursors on its own was also obtained (N,N'-dimethylurea). The resulting co-crystallisations did not all follow the design quite as intended. They did, however, yield interesting new structures, some of which have the potential to be proton migration and transfer systems.

Contents

CHAPTER 1

General Introduction

The structural arrangement of molecular solids is mainly dominated by the formation of intermolecular interactions between the constituent molecules.[1, 2] Included in these interactions are hydrogen bonds, which are generally considered weak but nevertheless are of extreme importance. As Linus Pauling stated some thirty years ago:

"Although the hydrogen bond is not a strong bond… it has great significance in determining the properties of substances… I believe as the methods of structural chemistry are further applied… that the significance of the hydrogen bond… <will be> *greater than that of any other single structural feature."*[3]

The importance of hydrogen bonding cannot be underestimated as it plays a pivotal role in the existence of life on earth. It is because of this phenomenon that water exhibits its unique properties (*e.g.* high melting and boiling points when compared to similar substances not connected by hydrogen bonds) and that base-pairing in DNA occurs.[3, 4]

As this work is directly concerned with this type of interaction a more detailed description follows. A hydrogen bond (D–H···A) is an interaction in which a hydrogen atom is attracted to two atoms, D (donor) and A (acceptor), which are typically oxygen or nitrogen, thereby acting as a bridge between them (see Figure 1.1). Hydrogen bonds have been recognised since early times to show a direct

proportionality relationship between bond strength and increasing electronegativity of D and A, suggesting the widely accepted concept that they are primarily electrostatic in origin. However, the hydrogen bond is now known to be a much broader phenomenon that ranges from weak (similar to van der Waals or dispersion interactions) to strong (quasi-covalent) interactions. A summary of the properties for the range of hydrogen bond interactions is given in Table 1.1.[5]

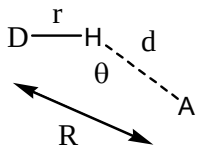

Figure 1.1. Diagrams of a hydrogen bond with the geometrical parameters *r, d* and *R* that represent the distances D**–**H, H···A and D···A respectively, whereas θ denotes the angle D**–**H···A.

Table 1.1. Some properties of strong, moderate and weak hydrogen bonds. The numerical data are to be taken as a guide leading to flexible borderlines.[6]

	Weak	**Moderate**	**Strong**
interaction type	electrostatic / dispersive	mostly electrostatic	strongly covalent
bond lengths of H···A [Å]	>2.2	1.5-2.2	1.2-1.5
lengthening of D–H [Å]	<0.02	0.02-0.08	0.08-0.25
D–H versus D···A	D–H << H···A	D–H < H···A	D–H ≈ H···A
D···A [Å]	>3.2	2.5-3.2	2.2-2.5
directionality	weak	moderate	strong
bond angles [°]	>90	>130	170-180
bond energy [kJ mol^{-1}]	<15	15-60	60-170
relat. IR shift $\Delta\upsilon_{D\text{-}H}$ [cm^{-1}]	<10%	10-25%	25%

Weak hydrogen bonds are also characterised by possessing an underlying double well potential energy surface. Shortening the donor/acceptor distance results in the central barrier lowering until a single well is obtained for a strong hydrogen bond (see Figure 1.2).[7-9] As a consequence weak to moderate hydrogen bonds have been linked to proton transfer while short, strong hydrogen bonds (SSHBs) have been linked with proton migration.

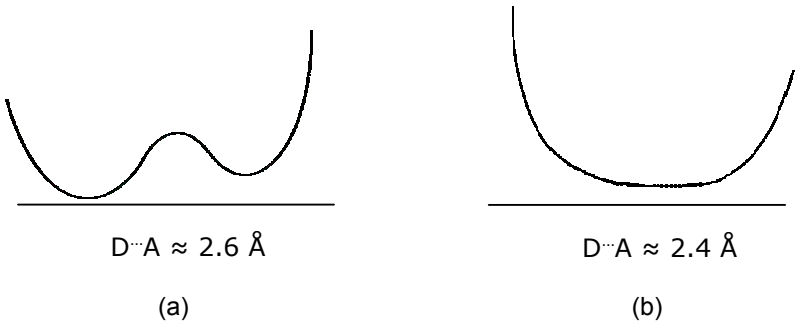

Figure 1.2. Diagrams of arbitrary potential energy surfaces of (a) moderate and (b) strong hydrogen bonds.

A double well potential energy surface supports the presence of two stable proton positions. Depending on the height of the barrier facile proton interconversion or relatively stable locked-in structures may occur.[10] This phenomenon is known as proton transfer and is of paramount importance in many aspects of chemistry and biology. From a fundamental perspective it is the mechanism by which nature achieves cell pH stabilisation and converts energy from one form into another.[11] From a technological perspective it underpins many of the current challenges for materials chemistry, including hydrogen storage and fuel cells.[12] In an attempt to gain deeper insight into these complex problems, simple models systems have been widely studied, *e.g.* in tautomerism-driven systems such as benzoic acid where the two forms that are involved in the transfer alternate between the keto and enol conformations [see Figure 1.3 (a)].[10, 13-15] The case of small organic compounds in the solid state where both structures are stable and proton transfer is achieved as a response to an external stimulus have, however, been rather neglected. Precedents in the literature are rare and include 1-phenyl-3-methyl-4-(4-methylbenzoyl)-5-pyrazolone 4-ethylthiosemicarbazone (PM4MBP-ETSC).[16] In this case proton transfer is thought to be induced by UV light along S···N linkages in the range 2.7-3.3 Å [see Figure 1.3 (b)]. Also, in the 1:1 adduct of squaric acid with 4,4'-bipyridine (SQBP),[17] temperature and pressure have been postulated to cause a phase transition involving proton transfer along N···O hydrogen bonds of length *ca.* 2.6 Å [see Figure 1.3 (c)].

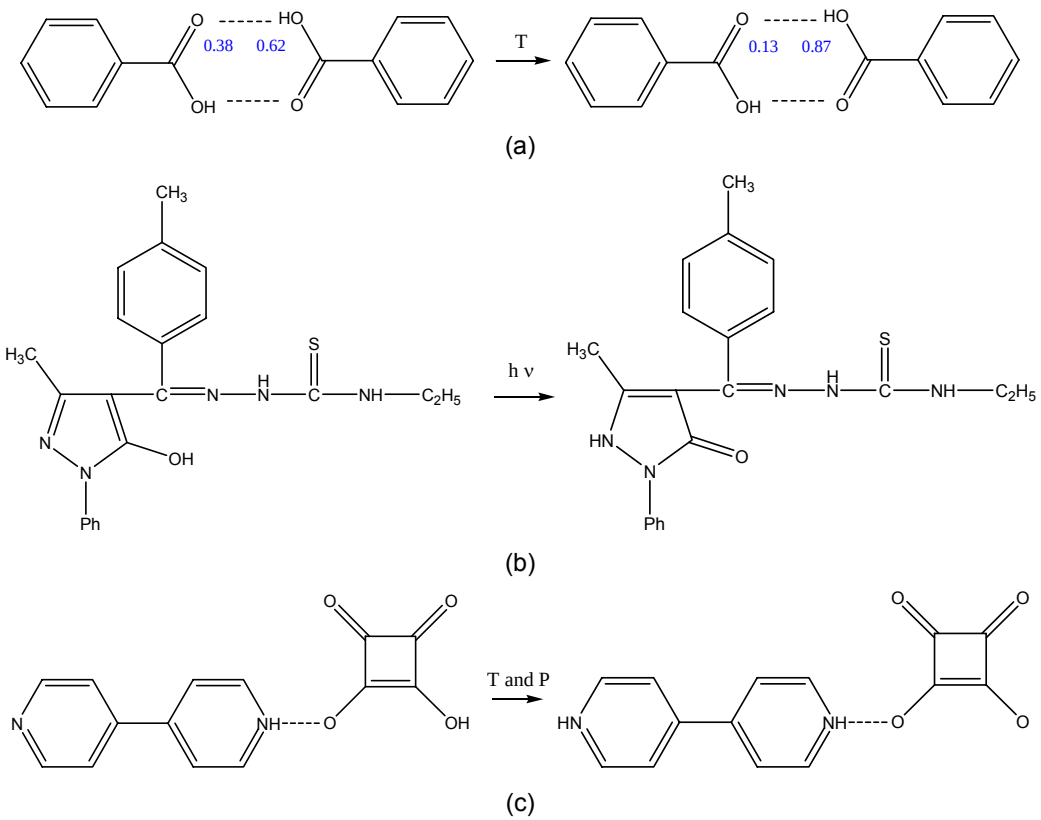

Figure 1.3. Diagrams of proton transfer for (a) benzoic acid dimers with the site occupancies of the hydrogen atoms shown in blue as temperature was decreased;[13] (b) PM4MBP-ETSC; and (c) SQBP.

An asymmetric single well potential energy surface supports the phenomenon of proton migration in the solid-state. Changes in external stimuli lead to subtle changes, which in turn lead the time-averaged position of the hydrogen atoms to shift (migrate) along the SSHB. It is a much rarer event than proton transfer. The occurrence of SSHBs in the Cambridge Structural Database[18] is limited to just *ca.* 1 % (1880 structures) of the total relevant structural entries.[19] Of these only a few cases have been reported to show proton migration. As shown in Figure 1.4, these include the 1:1 adduct of urea with phosphoric acid (UPA),[7, 20-24] pyridine-3,5-dicarboxylic acid (PDA),[25] the 1:2 adduct of benzene-1,2,4,5-tetracarboxylic acid with 4,4'-bipyridine (BTA)[26] and the 1:1 adduct of 4-methylpyridine with pentachlorophenol (4-MePy.PCP).[27] The D···A (O···O/N) distances in these

compounds range from 2.4 to 2.5 Å and the migration effect was observed following systematic variable temperature diffraction studies and of variable pressure in the case of UPA.

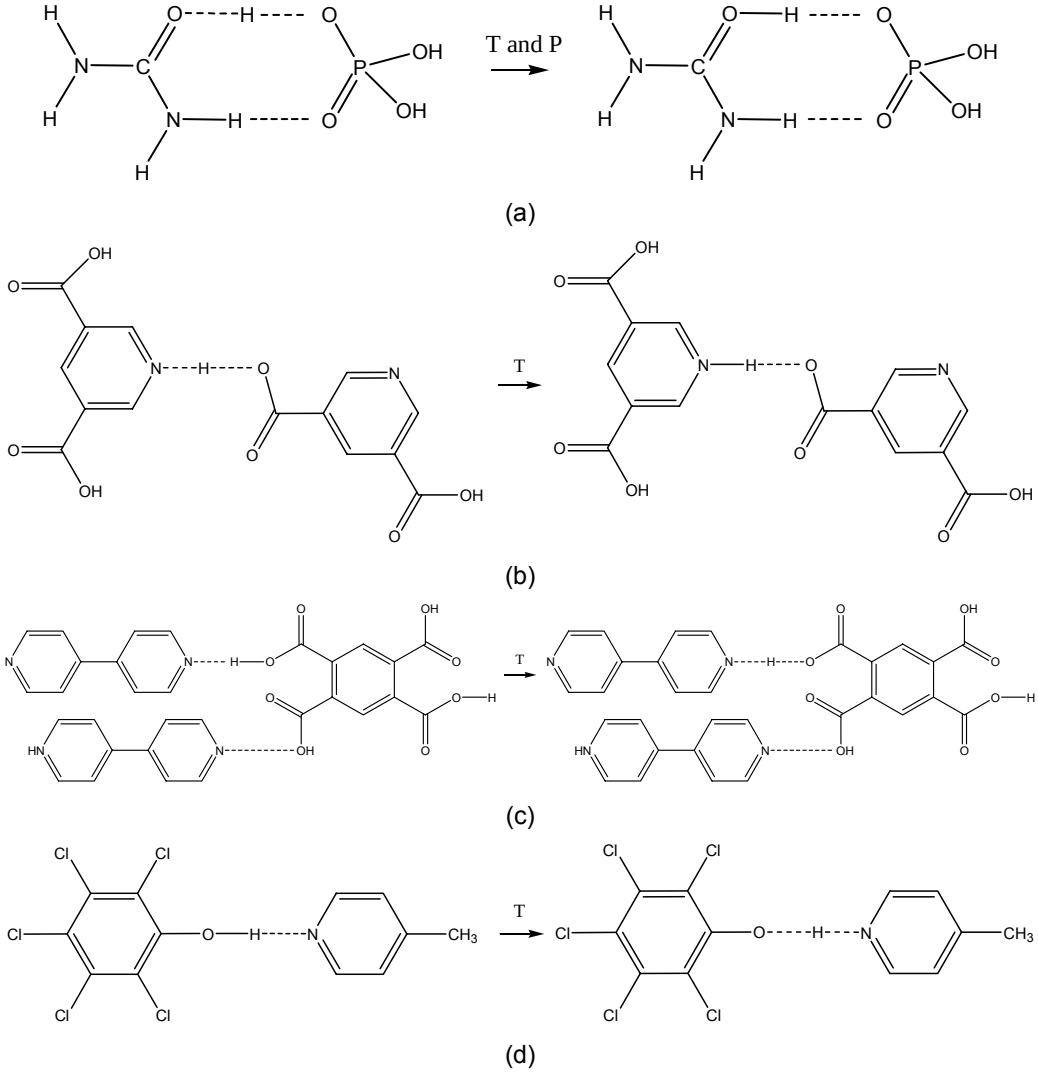

Figure 1.4. Diagrams of proton migration with decreasing temperature for (a) UPA, (b) PDA, (c) BTA and (d) 4-MePy.PCP.

The study of the 1:1 adduct of UPA [see Figure 1.4(a)] is worth special mention, as it is the most widely studied proton migration material. The SSHB (O¨¨O) linking the acid and base components of the complex is around 2.41 Å for the hydrogen-containing compound, and 2.42 Å for the perdeuterated compound. Single-crystal neutron diffraction showed proton migration was induced from the base to the centre of the bond by as much as 0.05 Å for the hydrogen-containing compound (and 0.1 Å for the perdeuterated compound) as temperature was raised from 15 K to 335 K.[7, 21, 22, 24] Furthermore, *ab initio* calculations reported results consistent with the experimental results, thus offering the attraction of having a reliable model that can be interrogated at the atomistic level.[20, 23] On the basis of these simulations it is thought that the effect of temperature is to modulate the low frequency lattice vibrations of the crystal structure which cause changes in the underlying hydrogen-bond potential that result in a shift in proton position.

The work carried out for the preparation of this thesis followed on directly from the original studies performed on the UPA adduct. Specific aims were to:

- Design and synthesise new hydrogen-bonded molecular crystals with the potential to exhibit proton migration and transfer;
- Characterise these new materials using a range of parametric diffraction techniques including single-crystal, powder, X-ray and neutron diffraction techniques, along with a range of physical chemistry techniques such as differential scanning calorimetry and spectroscopy.
- Rationalise the interesting proton behaviour using advanced computational modelling techniques to identify stable protonation sites, extract underlying potential energy surfaces and offer useful insight into general material properties.

After the fundamentals of the methods used throughout the research undertaken for this thesis are discussed (see Chapter 2), experimental results on the proton transfer study of the 1:1 adduct of squaric acid with 4,4’-bipyridine will be addressed (Chapter 3). Chapter 4 focuses on the study of co-crystals that were

designed with the use of a stronger base than that used in Chapter 3, with the design aim of reducing the temperature at which proton transfer occurred. Chapter 5 discusses work on a new derivative of the parent UPA adduct. The study of various compounds that were designed to yield SSHBs (but for one reason or another did not) are presented in Chapter 6. Finally, conclusions and trends that were encountered throughout the research presented in this thesis are summarised in Chapter 7, along with comments of where this research should go next.

Bibliography

[1] C. B. Aakeröy, K. R. Seddon, *Chem. Soc. Rev.* **1993**, *22*, 397.

[2] G. R. Desiraju, *Curr. Sci.* **2001**, *81*, 1038.

[3] L. Pauling, *The Chemical Bond - A Brief Introduction to Modern Structural Chemistry*, 3rd ed., Cornell University Press, Ithaca, **1967**.

[4] J. D. Watson, F. H. C. Crick, *Nature (London, U. K.)* **1953**, *171*, 737.

[5] T. Steiner, *Angew. Chem. Int. Ed.* **2002**, *41*, 48.

[6] G. A. Jeffrey, *An Introduction to Hydrogen Bonding*, Oxford University Press, Oxford, **1997**.

[7] C. C. Wilson, *Acta Cryst. B* **2001**, *57*, 435.

[8] C. C. Wilson, L. H. Thomas, *C. R. Chimie* **2005**, *8*, 1434.

[9] C. C. Wilson, L. H. Thomas, C. A. Morrison, *Chem. Phys. Lett.* **2003**, *381*, 102.

[10] P. Gilli, V. Bertolasi, L. Pretto, A. Lycka, G. Gilli, *J. Am. Chem. Soc.* **2002**, *124*, 13554.

[11] R. J. P. Williams, *Annu. Rev. Biophys. Biophys. Chem.* **1988**, *17*, 71.

[12] K.-D. Kreuer, *Chem. Mater.* **1996**, *8*, 610.

[13] C. C. Wilson, N. Shankland, A. J. Florence, *Chem. Phys. Lett.* **1996**, *253*, 103.

[14] C. C. Wilson, X. Xu, A. J. Florence, N. Shankland, *New J. Chem.* **2006**, *30*, 979.

[15] P. Durlak, C. A. Morrison, D. S. Middlemiss, Z. Latajka, *J. Chem. Phys.* **2007**, *127*, 064304/1.

[16] B. H. Peng, G. F. Liu, L. Liu, D. Z. Jia, *Tetrahedron* **2005**, *61*, 5926.

[17] M. T. Reetz, S. Hoger, K. Harms, *Angew. Chem. Int. Ed. Engl.* **1994**, *33*, 181.

[18] F. H. Allen, W. D. S. Motherwell, *Acta Cryst. B* **2002**, *58*, 407.

[19] For this study the D---A distance was restricted to be in the range 2.3-2.55 A and the DHA angle to 150-180 degrees, where D and A were oxygen or nitrogen. Furthermore only organic structures with Ar as the heaviest atom were considered.

[20] C. A. Morrison, M. M. Siddick, P. J. Camp, C. C. Wilson, *J. Am. Chem. Soc.* **2005**, *127*, 4042.

[21] C. C. Wilson, C. A. Morrison, *Chem. Phys. Lett.* **2002**, *362*, 85.

[22] C. C. Wilson, K. Shankland, N. Shankland, *Z. Kristallogr.* **2001**, *216*, 303.

[23] F. Fontaine-Vive, M. R. Johnson, G. J. Kearley, J. A. K. Howard, S. F. Parker, *J. Am. Chem. Soc.* **2006**, *128*, 2963.

[24] C. R. Pulham, C. Spanswick, D. S. Middlemiss, C. A. Morrison, R. M. Ibberson, K. S. Knight, *To be submitted.*

[25] J. A. Cowan, J. A. K. Howard, G. J. McIntyre, S. M.-F. Lo, I. D. Williams, *Acta Cryst. B* **2005**, *61*, 724.

[26] J. A. Cowan, J. A. K. Howard, G. J. McIntyre, S. M.-F. Lo, I. D. Williams, *Acta Cryst. B* **2003**, *59*, 794.

[27] T. Steiner, I. Majerz, C. C. Wilson, *Angew. Chem. Int. Ed.* **2001**, *40*, 2651.

CHAPTER 2

Experimental and Computational Methods

2.1. Introduction

In this chapter the basic concepts of the techniques used in this thesis to study the structure of both isolated molecules and molecular crystals will be described. These include: general characterisation methods such as electronic and vibrational spectroscopies[1] that identify local structural information, *e.g.* functional groups; diffraction techniques[2-4] that give longer range information *e.g.* molecular packing arrangements; and differential scanning calorimetry, which probes the response of materials to heat. Computational modelling[5, 6] was used to complement experimental measurements and to aid in their interpretation.

2.2. Experimental methods

2.2.1. Electronic and vibrational spectroscopies

In general terms spectroscopy is concerned with the interaction of electromagnetic radiation with matter. The electromagnetic spectrum (see Figure 2.1) can be divided into various regions, each one characterised in terms of the molecular response it invokes (e.g. rotational, vibrational, electronic or some ionization process). The basic experimental set-up involves monitoring the absorption of radiation to give a characteristic spectrum which is subsequently analysed to yield structural information.

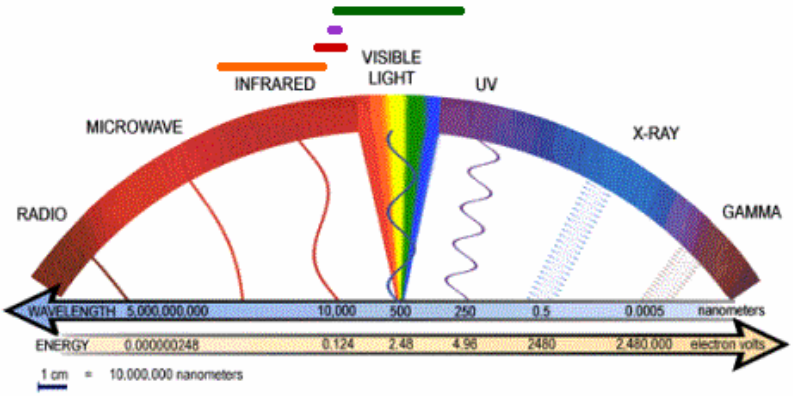

Figure 2.1. The electromagnetic spectrum.[7]

To turn now to the specific methods applied in this work, the ultraviolet and visible (UV-visible) regions of the electromagnetic spectrum (200–800 nm) can be used to characterise electronic transitions of valence electrons in molecules, *e.g.* from the highest occupied molecular orbitals (HOMO) to the lowest unoccupied molecular orbitals (LUMO). In organic molecules, absorption of UV-visible radiation is restricted to certain functional groups (chromophores) that generally contain an unsaturated group in the molecule. The spectrum of a molecule containing these chromophores is often complex due to the superposition of rotational and vibrational transitions on the electronic transitions, which gives a combination of overlapping lines and consequently leads to continuous absorption bands.

Mid-infrared (IR) spectroscopy (400-4000 cm^{-1}) can be used to probe molecular structures because different functional groups vibrate at different frequencies.

Technological advances for both UV-visible and IR spectrometers, enabled data collections to be performed directly on single-crystals, instead of the more standard approaches using solutions, KBr pellets or Nujol mulls. Furthermore, the availability of a variable temperature stage allowed proton transfer and migration processes to be studied as a function of temperature.

2.2.2. Differential scanning calorimetry

Differential scanning calorimetry (DSC) is a thermoanalytical technique in which the difference in the amount of heat required to increase the temperature of a sample and a reference sample, is measured as a function of temperature. This allows the monitoring of phase changes such as melting and crystallisation temperatures, as well as those associated with rearrangements of molecules in the solid state (*i.e.* phase transitions). Consequently, transition temperatures can be identified, and a direct measure of phase stability and estimate of the energy difference between phases, can be obtained.

2.2.3. X-ray diffraction

The aim of diffraction methods is to enable the detailed visualisation of atoms and molecules. As a result, access to large amounts of information, including connectivity and conformation is obtained. In order to achieve this it is necessary to use radiation of a wavelength comparable to the interatomic separation (*ca.* 10^{-10} m). Such radiation is readily available from X-rays produced by most standard diffractometers possessing sealed high-vacuum tubes where a flat plate of a very pure metal – usually Mo (giving rise to X-rays of wavelength 0.7135 Å), Cu (1.5443 Å) or Cr (2.2935 Å) – is bombarded with a beam of electrons generated by an applied voltage of 30-60 kV.

The reason why diffraction studies are performed on crystalline materials is because this state has a very high degree of internal order that is periodic in three dimensions. The smallest building block that is repeated in space is known as a unit cell, and is characterised by the lattice constants *a*, *b*, *c* and the angles between them α, β, γ (see Figure 2.2).

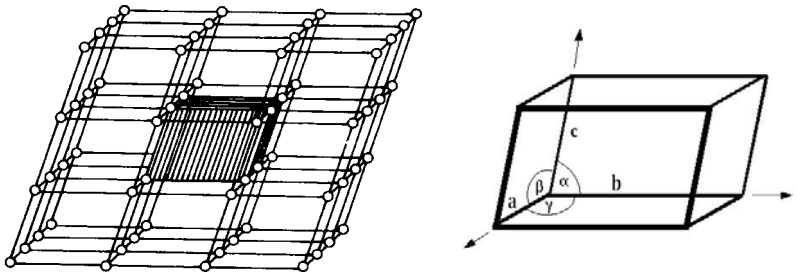

Figure 2.2. Portion of a lattice where a unit cell is shaded (left) and expanded on the right.[8, 9]

It was the realisation that the lattice (*i.e.* the periodicity of the crystal structure) could be used as a three-dimensional diffraction grating for X-rays that led von Laue to suggest to Friedrich and Knipping to try diffracting X-rays by crystals in order to test the hypothesis that such waves had wavelengths of the order of 10^{-10} m.[10] The resulting experiment performed in 1912 was revolutionary and was followed shortly by the first structure determination by X-rays methods carried out by W. L. Bragg on sodium chloride.[11]

Bragg postulated that the scattered radiation from a crystal behaved as if the diffracted beam was "reflected" from planes passing through points of the lattice (*cf.* light by a mirror, for which the angle of incidence is equal to the angle of reflection). This is illustrated in Figure 2.3, which shows the path difference (AB + BC = $2d\sin\theta$) between waves scattered from adjacent parallel lattice planes. For diffraction maxima to occur, these two waves have to be completely in phase, which can only happen if the path difference is equal to an integral number of wavelengths ($n\lambda$). This leads to Bragg's Law (Equation 2.1):

$$n\lambda = 2d\sin\theta \qquad \text{Equation 2.1}$$

where d is the separation between the planes and, λ and θ are the wavelength and scattering angle of the X-rays, respectively. The angles of incidence that do not satisfy the equation yield out of phase waves with consequent destructive interference. As a result, diffraction is observed over small areas and in specific arrangements.

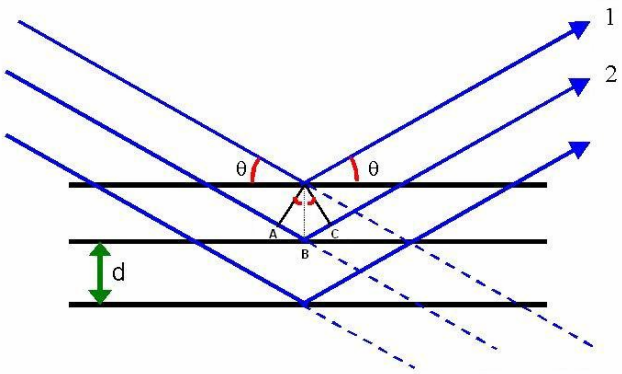

Figure 2.3. – Diagram of the Bragg construction for diffraction.

The arrangement of a diffraction pattern depends only on the dimensions of the crystal lattice; while the intensities of the diffracted beams are related to the arrangement and nature of atoms in a crystal by Fourier transformations (see Figure 2.4).

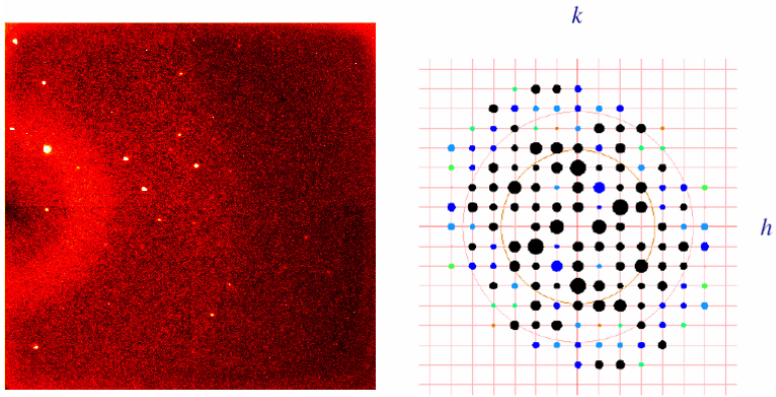

Figure 2.4. Experimental and computer-generated single-crystal diffraction patterns.

The diffraction pattern is the Fourier transform of the electron density. For the purpose of crystallography these transformations can be regarded as a convenient way to collapse both the amplitude (|F|) and the phase (φ) of the diffracted waves into a complex quantity, denoted F, the structure factor (see Figure 2.5). Each reflection can therefore be mathematically translated as shown by Equation 2.2.

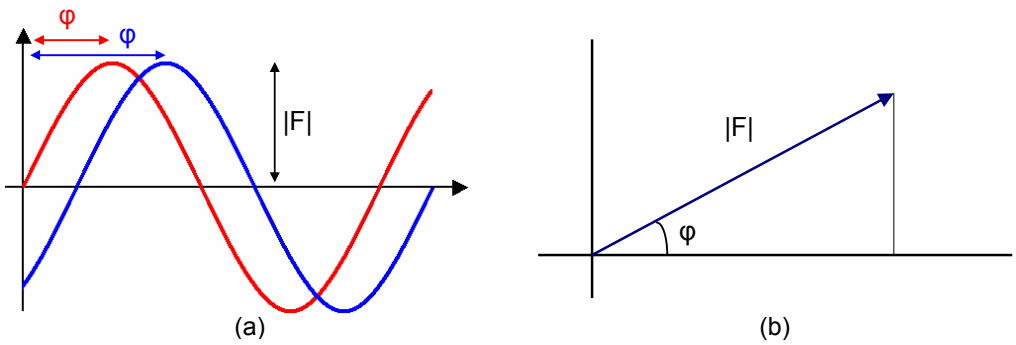

Figure 2.5. (a) Amplitude and phases of two waves; (b) Relationship between waves and vectors.

$$F_{hkl} = |F_{hkl}| \cdot \exp(i\varphi_{hkl}) \qquad \text{Equation 2.2}$$

The intensities observed maintain the information about the amplitudes of the waves ($I \propto |F|^2$), but unfortunately the knowledge of the relative phases of the waves that compose each reflection is lost. This is a central problem in crystallography, since both of these are required for accurate structure determination to be achieved. It is known as 'the phase problem', and one possible solution to it is to adopt an iterative process whereby phases are linked to a model (a trial structure) determined from a structure solution method (*e.g.* Patterson[12, 13] or direct methods[14]). Both of these are consequently refined in order to achieve the best possible agreement between observed and calculated amplitudes or intensities. The result of this process leads to the determination of the crystal structure.

Since X-rays are scattered by the electronic cloud of atoms, the scattering factor is proportional to the atomic number. Because atoms have a finite size, X-rays are not only scattered at the surface of a single point but throughout it. This results in partial destructive interference (as the radiation travels different pathways through the atom and hence recombines in slightly different phases). Therefore the scattering factor will also be dependent on the scattered angle of radiation (2θ), where the atoms possessing bigger electron clouds have a more pronounced fall-off in intensity at higher angle (see Figure 2.6).

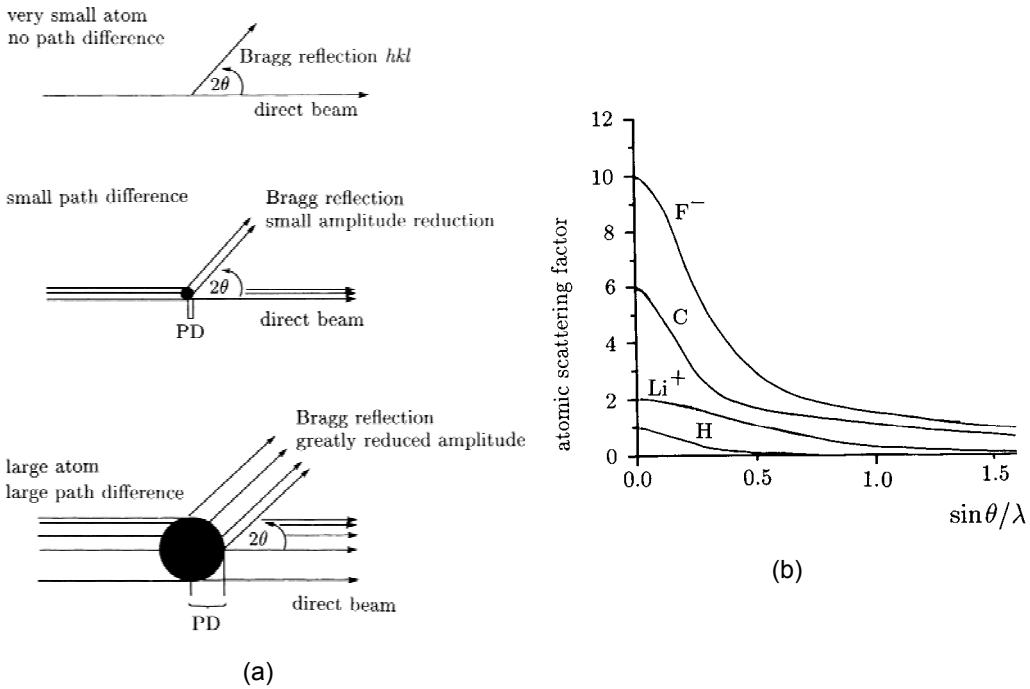

Figure 2.6. (a) The effect of the size of an atom on the intensities of diffracted beams as a function of the scattering angle. (b) X-ray scattering power for selected atoms (H, Li, C, F) as a function of the Bragg angle θ and the wavelength.[3]

Another factor that also has a similar effect on the scattering power of the atoms is their inherent vibrational motion, which is affected by temperature (see Figure 2.7). As atoms vibrate, and considering only the case that they do so equally in all directions (isotopically), they can be represented in three dimensions by a sphere. The more an atom vibrates the larger the sphere becomes, and this causes a decrease of the scattering factor. It is for this reason that routine collection of X-ray data is usually undertaken at low temperature.

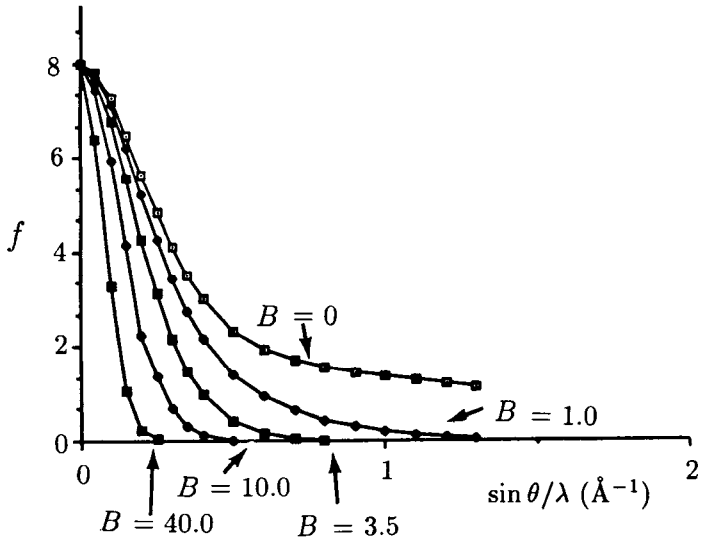

Figure 2.7. The effect of atomic thermal motion on the oxygen scattering factor. It should be noted that *B* is the displacement parameter for an atom so it is a measure of the size of the atom and is presented in ascending order.[3]

2.2.4. High-pressure X-ray diffraction

Pressure is another thermodynamic variable that can be combined with X-ray diffraction studies. Studies of the structural response of systems to this external stimulus give insight into intermolecular forces and packing arrangements and have therefore been found to be an efficient method for the exploration of polymorphism.[15] Most of the progress of this area of crystallography has been due to the development of simple devices that can be used in combination with the available diffraction apparatus, such as the Merrill-Bassett diamond-anvil cell (DAC) in the mid 1970s.[16] This cell (see Figure 2.8) is composed of two gem-cut diamonds with flat faces mounted on two beryllium discs, placed opposite to each other. A tungsten gasket is drilled to accommodate the sample, a ruby chip[17, 18] (used as a pressure calibrate) and a pressure transmitting medium (to ensure hydrostatic pressures). The gasket is then aligned between the diamonds and the whole structure is bound in a steel casing. Pressure is subsequently applied by tightening the screws attached to the steel casing. Because of the configuration, very little force is required to create extremely large pressures in the sample chamber.

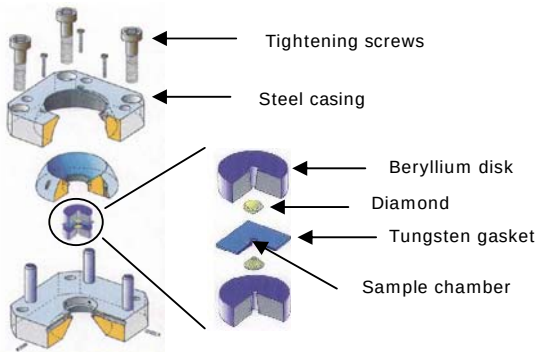

(a)

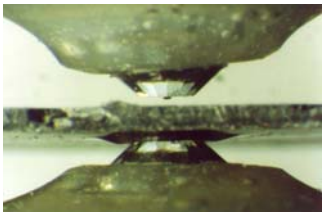

(b)

Figure 2.8. (a) Diagram of the DAC;[19] (b) optical image of the diamonds approaching, when closing the DAC.[20]

There are, however, limitations in using the DAC which include: (i) the reduced volume of the sample chamber; (ii) the diamond anvils and the beryllium discs are not as transparent to X-rays as desirable, and for these reasons some background scattering is inherent to this technique; and (iii) the steel casing limits the sampling of reciprocal space to about 40 %, whereby the higher angle data (short *d*-spacing) cannot be measured, making location of hydrogen atoms difficult. In order to overcome some of these limitations the experiments generally take place at synchrotron radiation facilities. In these installations electrons are accelerated at speeds close to that of light in closed orbits of very large radii. The electromagnetic radiation emitted tangentially from the ring is continuous in wavelength (covering a wide range of X-ray wavelengths) with the benefits of possessing much greater intensity and focus than that obtained from standard laboratory X-ray sources.

2.2.5. Other types of diffraction experiments

So far, the subject of diffraction has focused on the interaction of X-rays with a single crystal. However, during the studies that will be presented in this thesis powdered samples and neutron radiation were also used. The general principles of diffraction discussed so far, also apply to both of these experiments, and therefore only the most pertinent differences are highlighted below.

2.2.5.1. Powder diffraction

In a powder diffraction experiment the sample that is measured is multicrystalline generally composed of a very large number of tiny crystals orientated in a random fashion. As such, when the sample is irradiated by X-rays the individual crystals will diffract in accordance with the Bragg equation, and the overall pattern obtained is the result of the superposition of each of those of the individual crystals. The resulting pattern is therefore composed of a series of concentric rings, which can be thought of as the result obtained from rotating a single-crystal pattern through 360° (see Figure 2.9).

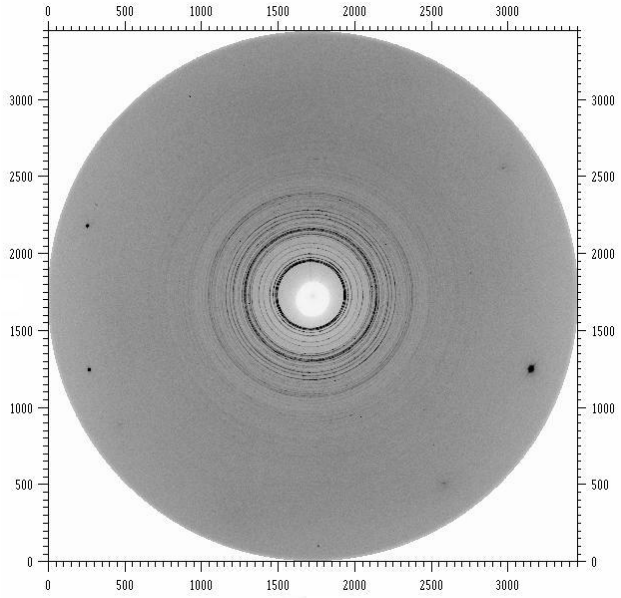

Figure 2.9. Powder pattern obtained from Station 9.5 at the STFC Daresbury Laboratory using an image plate.

In powder diffraction experiments, the information contained in the three-dimensional distribution of the reflections is collapsed into a one-dimensional pattern, where the remaining variable is the scattering angle (θ). This reduction in available data makes the problem of structure determination rather difficult. Nevertheless it does have the advantage that the sample preparation is much easier than that required for single-crystal experiments, as growing suitable single-crystals can be notoriously difficult. In addition, the data-collection times are much shorter

when compared to those performed on single-crystals. For these reasons this technique is very powerful and finds application in qualitative analysis, where the information that is collected sheds light on bulk-sample properties, such as phase identification and studying the reversibility of phase transitions.[2]

2.2.5.2. Neutron diffraction

The basis by which neutrons can also be used in structure determination comes from the fact that these particles can exhibit wavelengths commensurate to interatomic distances, according to de Broglie's relationship (Equation 2.3):

$$\lambda = \frac{h}{p} = \frac{h}{mv} \qquad \text{Equation 2.3}$$

where p is the momentum, m is the mass and v is the velocity of the particle, λ the wavelength of the corresponding wave, and h Planck's constant. Thus neutrons accelerated to thermal velocities in the range 2500-8000 ms^{-1}, typically obtained in neutron sources, will have wavelengths in the range 1.5-0.5 Å.[2]

Neutrons and X-rays interact differently with crystalline samples, and can therefore been seen as complementary techniques. Whilst X-rays are scattered by the electrons of an atom, neutrons are scattered by the nuclei of atoms. The chances of a nucleus scattering a neutron are much lower than an electron cloud scattering an X-ray, and consequently neutron diffraction intensities are on average much lower than those obtained by X-ray diffraction measurements. For this reason neutron diffraction experiments require larger samples and longer data-collection times compared to their X-ray counterparts. Alongside these difficulties is the uncertainty of availability of time at a neutron source. On the other hand, neutron scattering is not dependent on the scattering angle, as observed for X-rays, but it should be noted that there is no longer a relationship between the scattering power and atomic number. In the case of neutrons the scattering power varies randomly across the periodic table (see Figure 2.10).

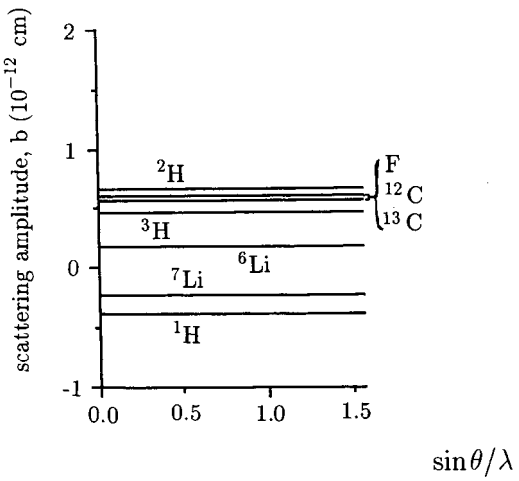

Figure 2.10. Neutron scattering power for selected atoms (H, Li, C, F and certain isotopes) as a function of the Bragg angle θ and wavelength.[3]

The main advantage in performing neutron diffraction experiments in the course of this work is the ability to locate accurately light (*i.e.* hydrogen or deuterium) atoms. This comes from the fact that these atoms scatter neutrons strongly, in contrast to X-rays. It should be noted that hydrogen is a strong incoherent scatterer of neutrons (that is, the phase of the outgoing wave is not determined by that of the incident wave) and as a result the diffraction of a hydrogenous sample can be seen to have a low peak to background ratio. This problem is generally avoided by deuteration of the sample, which gives a much improved background, or if possible by resorting to a source with an extremely high flux source (*e.g.* the D20 beamline at the Institut Laue-Langevin).

2.3. Computational modelling

Computational modelling is nowadays commonly used in chemistry. It aims to represent, understand and manipulate the structures of molecules and the properties that are dependent on them. In order to achieve this there are two main approaches that can be adopted: one where the electron distribution is neglected (molecular mechanics) and the other where it is described in detail (quantum mechanics, also known as *ab initio* calculations, derived from the Latin 'from the

beginning'). The nature of the work undertaken for this thesis required the latter approach, and for this reason, the fundamentals of this method are described below.

Quantum mechanical calculations deal with the descriptions of electrons which, based on de Broglie's wave-particle duality and the Heisenberg uncertainty principles, can be substituted by a function that determines the probability of the electrons being at a particular position (Ψ). This allowed Schrödinger in 1926 to derive what is referred to as the Schrödinger wave equation or simply Schrödinger equation (see Equation 2.4).[21]

$$\mathrm{H}\psi = E\psi \qquad \text{Equation 2.4}$$

Solving this equation requires finding a value of E (the energy of the system) and corresponding Ψ (the molecular wavefunction) subject to certain constraints.[22] The symbol H denotes the Hamiltonian operator, which 'operates' on the wavefunction to return the wavefunction multiplied by the energy.[23] The Hamiltonian operator comprises the kinetic and potential energy terms of the system, namely: (i) the kinetic energy of the electrons, (ii) the kinetic energy of the nuclei, (iii) the potential energy of nuclear-electronic attraction, (iv) the potential energy of electronic repulsion and (v) the potential energy of nuclear repulsion, as formally represented in Equation 2.5.

$$\mathrm{H} = -\sum_i \frac{\hbar^2}{2m_e}\nabla_i^{\,2} - \sum_k \frac{\hbar^2}{2m_n}\nabla_k^{\,2} - \sum_l \sum_k \frac{e^2 \mathrm{Z}_k}{4\pi\varepsilon_0 r_{lk}} + \sum_{i<j} \frac{e^2}{4\pi\varepsilon_0 r_{ij}} + \sum_{k<l} \frac{e^2 \mathrm{Z}_k \mathrm{Z}_l}{4\pi\varepsilon_0 r_{kl}} \qquad \text{Equation 2.5}$$

Where *i* and *j* run over all electrons, *k* and *l* run over all nuclei, $\hbar$ is Plank's constant divided by 2π, m_e is the mass of an electron, m_n is the mass of a nucleus, ∇ is the Laplacian operator, *e* is the charge of an electron, *Z* is the atomic number of an atom and r_{ab} is the distance between particles *a* and *b*.

The solution of this equation for a particular system gives rise to not only the structure, but also other fundamental properties of such a system such as energies (*e.g.* of polymorphs and of bonds), band gaps, atomic charges and vibrational frequencies. The remarkable fact is that all of this is achieved with impressive

accuracy. Results are comparable with experiment in the cases where these can be determined experimentally.

It is important to realise that for quantum mechanical calculations to have reached this point a series of approximations had to be done. Paul Dirac's famous words (1929),[24] on Schrödinger's original formulation say it best: "*...The underlying physical laws necessary for the mathematical theory of a large part of physics and the whole of chemistry are thus completely known, and the difficulty is only that the exact application of these laws leads to equations much too complicated to be soluble...*"

One such approximation that brought us closer to the practical application of Schrödinger's work is the Born-Oppenheimer[25] approximation, which assumes that the nuclear and electronic properties of a system may be treated independently. This is due to the fact that electrons travel at far greater speeds than the nuclei. As a consequence the electrons can respond instantaneously to any perturbation of the nuclear positions. By employing this approximation the nuclear kinetic energy falls to zero, and the nuclear potential energy is replaced by a constant based on Coulomb's law. Thus Equation 2.5 can be recast as the electronic Schrödinger equation (Equation 2.6):

$$\left(-\sum_i \frac{\hbar^2}{2m_e} \nabla_i^{\,2} - \sum_l \sum_k \frac{e^2 Z_k}{4\pi\varepsilon_0 r_{lk}} + \sum_{i<j} \frac{e^2}{4\pi\varepsilon_0 r_{ij}} \right) \Psi(R,r) = E(R)\Psi(R,r) \qquad \text{Equation 2.6}$$

Although this represents a significant simplification, it only yields an equation that can be solved exactly for one-electron systems (*i.e.* H, He^+ and H_2^+). The difficulty lies with the electron – electron potential energy term (the third term of the Hamiltonian operator in Equation 2.6), which cannot be solved directly for any system containing more than one electron. This problem represents the greatest challenge in modelling atomic systems at the quantum level. In effect two separate electron behaviours have to be described: (i) correlation, in essence the fact that electrons repel each other, such that the motion of one affects all others, and (ii) exchange, the idea that two electrons can 'pair-up' and occupy the same region of space (*i.e.* possess the same principle quantum numbers n, l and m) if they have

opposite spin, *s*. In addition, the practicalities of running the calculations on computers must be borne in mind. In order to give rise to successful software, the approximations must translate into algorithms that are computationally efficient. The most successful approach here has been demonstrated to be to reduce the *n*-electron Schrödinger equation to *n* one-electron Schrödinger equations. The following two sections describe two fundamentally different approaches that have found success in approximating the electronic Schrödinger equation.

2.3.1. Hartree-Fock theory

The Hartee-Fock (HF) method is the most basic level of theory employed in *ab initio* calculations, and is the starting point upon which the more elaborated levels of theory are built. The central principle in HF calculations is that electron correlation is simply ignored. This is done by allowing each electron to move in a uniform electronic field created by all the other electrons present. Electron exchange is on the other hand treated exactly by imposing the condition of an anti-symmetric wavefunction, which for a two electron system can be formulated as shown below (Equation 2.7).

$$\psi(r_1, r_2) = \psi_{a\uparrow}(r_1)\psi_{b\uparrow}(r_2) - \psi_{a\uparrow}(r_2)\psi_{b\uparrow}(r_1) \qquad \text{Equation 2.7}$$

Thus, if two electrons with the same spin are in the same place (*i.e.* $r_1 = r_2$) the wavefunction (and therefore the probability) collapses to zero, obeying Pauli's exclusion principle.

Hartree-Fock theory thus provides a simple mechanism to reformulate the *n*-electron system into *n* one-electron Schrödinger equations, which are then summed to give one overall solution. In practice the equations are solved in an iterative [self-consistent field (SCF)] process starting from a set of guessed orbitals. The calculated orbitals are gradually improved until a convergence criterion is met. Although ignoring electron correlation is a drastic measure, HF theory can perform extremely well, recovering around 90-99 % of the overall energy depending upon the nature of the system. However, the missing interactions can have dramatic influences

on calculated properties which is the reason post-HF methods (*e.g.* MPx, CI, CC) as well as other theories (*e.g.* DFT), have been developed to attempt to include electron correlation behaviour.

2.3.2. Density functional theory

Density functional theory (DFT) takes another approach to obtaining the electronic structure of atoms and molecules. The idea behind it is that E can be calculated directly from the electron density, ρ. This is a significantly different stance to HF theory that derives E from Ψ. Thus DFT offers an immediate advantage over HF-based methods: ρ is an experimentally observable quantity, Ψ is not.

The basis of DFT relies on the theorem derived by Hohenberg & Kohn (1964).[26] They proved that each electronic ground-state corresponds to one electron density distribution ρ(r) and that from it one can calculate, in principle, the corresponding ground-state wavefunction and consequently the ground-state properties (*e.g.* energy). A further advantage is that the electron density is a function of only three (spatial) variables per electron, rather than the four (three spatial plus one spin) required to represent the many-electron wavefunction. Thus DFT calculations are well known to be appreciably more efficient than wavefunction-based methods.

In practice, solving the Schrödinger equation under the DFT formalism requires finding a solution to the Kohn-Sham equations (1965),[27] which are similar to the standard one-electron HF equations. However, DFT estimates both the electron correlation and exchange energies, but can do so over a local range only. So-called non-local effects, which are manifest in *e.g.* dispersive (van der Waal) interactions or when a bond is stretched to breaking point are not included, and this is perhaps the biggest criticism that can be levied at the technique.

DFT has one further serious limitation. The functional to translate ρ to E is not known exactly. Thus once again a series of approximations are adopted, but unlike wavefunction-based methods the functional cannot be systematically improved until convergence in molecular properties is met. Instead there exists a collection of available functionals based on different types of approximations. These

functionals are generally chosen by reputation for reliable results obtained for the types of systems of interest.

2.3.2.1. Basic DFT functionals

The simplest functional is the local density approximation (LDA), which assumes that ρ is a slowly varying function and so can be divided into a grid where each block is substituted by a constant. Thus, it provides good results for systems where the electron density is relatively constant, such as solid-state metals.

Improvements to this simple approximation resulted in the generalised gradient approximation (GGA). As the name suggests, there is inclusion of the gradient of the density at each block. A variety of gradient corrected functional forms have been developed for use with molecular systems, where the electron density is a rapidly changing property. The most widely used functionals are PBE of Perdew, Burke, and Ernzerhof,[28, 29] PW91 of Perdew and Wang,[30, 31] and BLYP, composed of the Becke exchange functional (B)[32] and the correlation functional of Lee, Yang and Parr (LYP).[33, 34]

2.3.2.2. Hybrid functionals

As discussed previously, HF theory calculates the exchange energy exactly whereas in DFT it is approximate. In order to capitalise on this, hybrid functionals have been developed which incorporate a linear combination of (exact) HF exchange with some other combination of exchange and correlation from LDA and GGA functionals. The relative proportions of the three components are determined by an empirical fit against a training set of molecules, giving rise to *e.g.* the widely applied B3LYP functional, which is composed of Becke's three parameter exchange functional (B3)[35] and the LYP correlation functional.[33, 34]

2.3.3. Basis sets

In the previous sections the approximations required to the Hamiltonian so that an approximation to the true solution to the Schrödinger equation can be obtained were discussed. It is now time to proceed in a similar fashion with respect

to the wavefunction, $\psi_i(r)$, which is represented by a collection of basis functions [also known as atomic orbitals (AO) – $\phi_\alpha(r)$] termed basis set. In a practical manner these are known mathematical functions that combine linearly to describe the electron distribution (and hence the electron density and molecular orbitals). For this reason this approach is designated the linear combination of atomic orbitals – LCAO approach (see Equation 2.8). It should be noted, however, that this represents another approximation because it is impossible to use an infinite number of basis functions and the series will therefore be truncated at some level. Nevertheless according to the variational principle the more functions used the better the basis set is.

$$\psi_i(r) = \sum_\alpha c_{i\alpha}\,\phi_\alpha(r) \qquad \text{Equation 2.8}$$

Where $c_{i\alpha}$ represents the set of weighting coefficients applied to each basis function. These coefficients are optimised until the ground-state wavefunction is obtained (that is, the lowest eigenvalue is obtained when the wavefunction is acted upon by the Hamiltonian operator).

2.3.3.1. Localised basis sets

Localised basis sets are those where the basis functions are centered on atomic nuclei, and are mainly represented by Slater-type orbitals (STOs)[36] or Gaussian-type orbitals (GTOs).[37, 38]

STOs use functions that are based on the atomic 1*s* orbital of a hydrogen atom, thus providing an accurate description of the electron density with distance from the nucleus. However, they do not lend themselves well to calculations of multiple integrals. It is therefore common to substitute the use of STOs for GTOs, as these are much more amenable of being computed. GTOs have some deficiencies, however, in describing the correct form of the electron density, as close to the nucleus they have no cusp and they also decay too rapidly at long ranges. These issues can be overcome by combining a number of GTOs, the overall effect of which is to create a new function which is a good-enough approximation of the atomic wavefunction (see Figure 2.11).

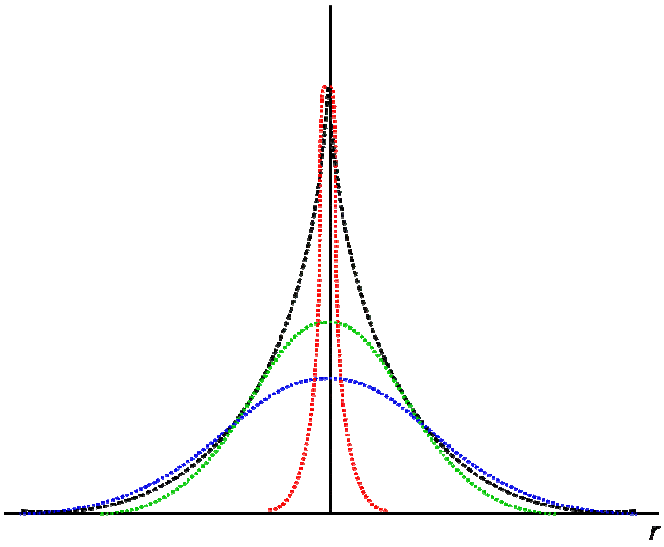

Figure 2.11. One-dimensional illustration of the summation of three GTOs (red, green and blue doted lines) approximating a Hydrogen 1s wavefunction (black dashed line).[39]

In the description of basis sets so far, all electrons have been treated in the same way. As a way to reduce computational effort it could be argued that only the valence electrons are chemically relevant, as the core electron will remain unchanged throughout the whole simulation. To this end split-valence basis sets were developed, which allow the core and valence shells to be represented by different numbers of basis functions (*i.e.* different accuracy). Examples of these types of basis sets are those proposed by Pople and co-workers, such as 3-21G, which represents a basis set that uses three blocks of Gaussian functions. In this example, the first block is comprised of 3 GTOs to describe the core orbitals and the additional two blocks use 2 and a further 1 GTOs for the valence orbitals.

The electron cloud about an atom in a molecule is usually perturbed in comparison with the isolated atom. As it has been previously stated, basis sets are composed of atomic orbitals so, in order to correct for this polarisation functions are generally introduced (indicated by asterisks, *e.g.* 6-31G*). The polarisation functions allow the orbitals to have a higher angular quantum number (l) than required to describe the electronic ground-state, *e.g.* *p*-type functions for an *s*-block element. Furthermore, diffuse functions (indicated by a '+') can also be included in order to

model atomic orbitals which have electron density further away from the nucleus in molecular orbitals, such as anions or excited state species.

Localised basis sets are generally known as being used for calculations of isolated molecules (in the gas phase) but with the addition of translational symmetry they can also be employed in solid state calculations.

2.3.3.2. Delocalised basis sets

An alternative approach to mimic the molecular electronic configuration is to consider the electrons as nearly free particles instead of being confined to the region of space around the atomic nucleus. In such a case the behaviour of the electrons can be considered sinusoidal and the wavefunction can be remodelled as a linear combination of plane waves, in an analogous manner to the GTO description given above (Equation 2.9).

$$\psi_i(r) = \sum_k c_{ik} \exp(ik.r) \qquad \text{Equation 2.9}$$

Where k is the wavevector of the electrons, expressed as the reciprocal of the de Broglie's wavelength, and c_{ik} are the basis set weighting coefficients that are manipulated during the calculation until the electronic ground state is reached.

The plane-wave method has proven to be very successful for the modelling of condensed phase matter. The main reasons for this are that: (i) they are simple and fast to compute, (ii) they can be made as accurate as necessary in a continuous way by simply adding more plane-waves and (iii) they are periodic. However in order to describe the electronic density correctly a very large number of plane-waves is necessary, especially because of the fact that the core electrons of the individual atoms are rapidly oscillating around the nucleus. A simplification similar to that employed in Gaussian split-valence basis sets, has therefore been developed for plane-wave basis sets.[40] In this approach the core electrons, which are less involved in the physical properties of molecules, are replaced with a smooth effective potential (called a pseudopotential) that allows the valence region to be unchanged (see Figure 2.12). As a consequence the number of plane-waves required to represent the

wavefunction is significantly reduced with no appreciable loss in computational accuracy.[41]

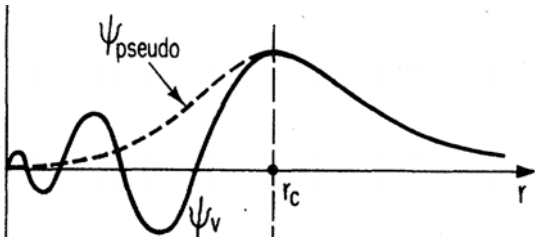

Figure 2.12. Schematic illustration of the pseudopotential concept. The solid line shows the all-electron wavefunction, ψ_v, while the dashed line shows the corresponding pseudo-wavefunction, ψ_{pseudo}. All quantities are shown as a function of the distance from the atomic nucleus, r. The cutoff radius, r_c, marks the point beyond which the all-electron and pseudo quantities become identical.[42]

2.3.4. Geometry optimisation

Up to this point the different parts required to determine the total energy of a structure (Ψ and H) have been discussed. This section will now consider how these are combined in order to lead to an optimised structure.

Firstly, knowing the wavefunction and the Hamiltonian of a system should "only" give us the total energy of such system (see Equation 2.4). Nevertheless, the energy is intimately related to the structure, and for that reason most physical properties of a given system can be derived from it.[42] The arrangement of atoms with the lowest energy [*i.e.* the potential energy surface (PES) minimum at 0 K] corresponds to a stable state, as forces must be applied in order to provoke change (see Figure 2.13).

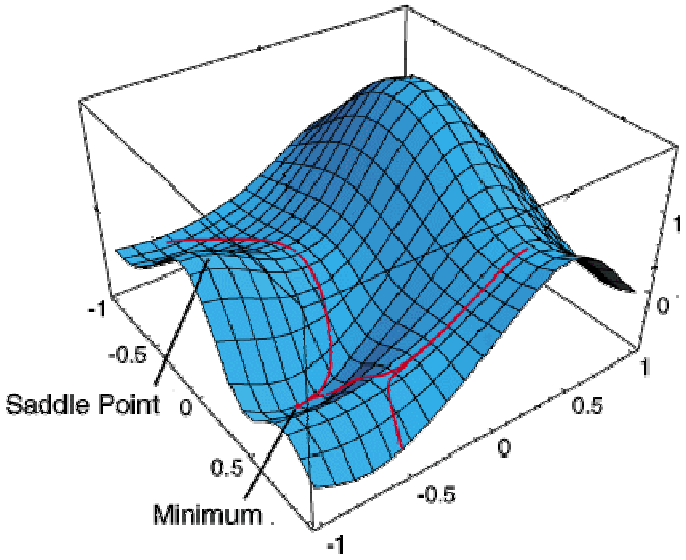

Figure 2.13. Schematic of a three-dimensional potential energy surface (PES).[43]

When performing geometry optimisations the fact that the forces are related to the structure of systems is taken as an advantage, in the sense that the atomic positions are optimised with respect to the forces (first derivatives of the energy with respect to the internal parameters) until they approach zero, at which point the optimised structure (a minimum) is reached. This is generally assisted by the use of estimates of the curvatures (second derivatives) of the PES, which are iteratively improved.

In practical terms it all comes together whereby starting from an input structure (trial or from experiment), the Born-Oppenheimer approximation is imposed and the ground state wavefunction is computed along with the forces and the estimates of the force constants. The atoms are then allowed to move (*i.e.* Born-Oppenheimer approximation is "lifted") according to Newton's law of motion which yields a structure that replaces the starting model. This process is then repeated in an iterative fashion until convergence with respect to forces and atomic displacements is obtained.

2.3.5. *Ab initio* molecular dynamics

Molecular dynamics (MD) simulations follow on from the optimised geometries, whereby these structures are allowed a certain amount of freedom to explore the PES. This is done by giving the system a certain amount of energy (which is closely related to the simulation temperature) that allows the atomic positions to evolve in time, according to Newton's law of motion. In effect, instead of driving the forces to zero, here the "natural" behaviour of the system is observed. Two methods that are widely used in the minimisation process of the electrons are the Born-Oppenheimer and the Car-Parrinello approaches. The main difference between these methods resides on the fact that in the first instance the electronic and nuclear coordinates are decoupled while in the latter case they are performed simultaneously. As a consequence of coupling the optimisation of electrons and nuclei a smaller time step has to be used in the calculations, so that the highest frequency (which in this case is electronic) can be sampled properly. Nevertheless Car-Parrinello MD remain much quicker which is the reason it is widely used even thought some instability and small errors may occur.[44-46]

2.4. Combining experiment and theory

During the work described in this thesis, several diffraction experiments have been performed in which, by necessity, the quality of data has been poor or data have been incomplete. This causes problems such as obtaining the accurate positions of hydrogen atoms. In order to help with this, computational modelling through the use of quantum mechanical calculations has also been performed. Furthermore the manipulation of matter in a virtual manner also offered the benefit of understanding essential components of the molecular systems in a way that would be inaccessible by experimental methods, such as shifting atoms along a particular reaction coordinate to obtain potential energy surfaces or swapping atoms of a structure to mimic other structures. For these reasons the synergetic combination of both experimental and theoretical methods has been used in this thesis, the results of which will be presented in the following four chapters.

2.5. Bibliography

[1] J. M. Hollas, *Modern Spectroscopy*, 3rd ed., John Wiley & Sons, New York, **1996**.

[2] C. Giacovazzo, H. L. Monaco, G. Artioli, D. Viterbo, G. Ferraris, G. Gilli, G. Zanotti, M. Catti, *Fundamentals of Crystallography*, 2nd ed., Oxford University Press, New York, **2002**.

[3] J. P. Glusker, M. Lewis, M. Rossi, *Crystal Structure Analysis for Chemists and Biologists*, Verlag Chemie, **1994**.

[4] W. Massa, *Crystal Structure Determination*, Springer-Verlag, Berlin, **2000**.

[5] F. Jensen, *Introduction to Computational Chemistry*, Wiley & Sons, Chichester, **1999**.

[6] A. R. Leach, *Molecular Modelling: Principles and applications*, 2nd ed., Prentice Hall, Essex, **2001**.

[7] http://nasaexplores.nasa.gov/show_912_student_st.php?id=030106134335.

[8] J. P. Glusker, K. N. Trueblood, *Crystal Structure Analysis: A Primer*, Oxford University Press, **1985**.

[9] http://xray0.princeton.edu/~phil/Facility/Guides/XrayDataCollection.html, (Ed.: P. Jeffrey).

[10] W. Friedrich, P. Knipping, M. Laue, *Sitzb. kais. Akad. Wiss.* **1912**, 303.

[11] W. L. Bragg, *Proc. Cam. Phil. Soc.* **1913**, *17*, 43.

[12] A. L. Patterson, *Phys. Rev.* **1934**, *46*, 372.

[13] A. L. Patterson, *Z. Kristallogr. Kristallgeom. Kristallphys. Kristallchem.* **1935**, *90*, 517.

[14] D. Harker, J. S. Kasper, *J. Chem. Phys.* **1947**, *15*, 882.

[15] F. P. A. Fabbiani, C. R. Pulham, *Chem. Soc. Rev.* **2006**, *35*, 932.

[16] L. Merrill, W. A. Bassett, *Rev. Sci. Instrum.* **1974**, *45*, 290.

[17] R. A. Forman, G. J. Piermarini, J. D. Barnett, S. Block, *Science* **1972**, *176*, 284.

[18] G. J. Piermarini, S. Block, J. D. Barnett, R. A. Forman, *J. Appl. Phys.* **1975**, *46*, 2774.

[19] http://www.crystal.vt.edu/crystal/dac.html.

[20] http://ph.ed.ac.uk/~dra.

[21] E. Schrödinger, *Ann. Physik* **1926**, *79*, 489.

[22] G. Wedler, *Manual de Química Física*, Fundação Calouste Gulbenkian, Lisbon, **2001**.

[23] Wavefunction and energy are deemed eigenfunction and eigenvectors, where eigen can be translated from german to mean proper, own, characteristic or peculiar.

[24] P. A. M. Dirac, *Proc. R. Soc. London, Ser. A* **1929**, *123*, 714.

[25] M. Born, R. Oppenheimer, *Ann. Physik* **1927**, *84*, 457.

[26] P. Hohenberg, W. Kohn, *Phys. Rev. B* **1964**, *136*, 864.

[27] W. Kohn, L. J. Sham, *Phys. Rev. A* **1965**, *140*, 1133.

[28] J. P. Perdew, K. Burke, M. Ernzerhof, *Phys. Rev. Lett.* **1996**, *77*, 3865.

[29] J. P. Perdew, K. Burke, M. Ernzerhof, *Phys. Rev. Lett.* **1997**, *78*, 1396.

[30] J. P. Perdew, in *Electronic Structure of Solids '91* (Eds.: P. Ziesche, H. Eschrig), Akademie Verlag, Berlin, **1991**, p. 11.

[31] J. P. Perdew, J. A. Chevary, S. H. Vosko, K. A. Jackson, D. J. Singh, C. Fiolhais, *Phys. Rev. B* **1992**, *46*, 6671.

[32] A. D. Becke, *Phys. Rev. A* **1988**, *38*, 3098.

[33] C. Lee, W. Yang, R. G. Parr, *Phys. Rev. B* **1988**, *37*, 785.

[34] B. Miehlich, A. Savin, H. Stoll, H. Preuss, *Chem. Phys. Lett.* **1989**, *157*, 200.

[35] A. D. Becke, *J. Chem. Phys.* **1993**, *98*, 5648.

[36] J. C. Slater, *Phys. Rev.* **1930**, *36*, 57.

[37] A. de Moivre, *Biometrika* **1733**, *59*, 677.

[38] A. de Moivre, *The Doctrine of Chances: a Method of Calculating the Probability of Events in Play*, 2nd ed., Woodfall, London, **1738**.

[39] P. D. McCaffrey, *PhD Thesis* **2007**, *The University of Edinburgh*.

[40] J. C. Phillips, *Phys. Rev.* **1958**, *112*, 685.

[41] M. L. Cohen, V. Heine, in *Solid State Physics, Vol. 24*, Academic Press, New York, **1970**, p. 37.

[42] M. C. Payne, M. P. Teter, D. C. Allan, T. A. Arias, J. D. Joannopoulos, *Rev. Mod. Phys.* **1992**, *64*, 1045.

[43] http://www.chem.wayne.edu/~hbs/chm6440/PES.html.

[44] R. Car, M. Parrinello, *Phys. Rev. Lett.* **1985**, *55*, 2471.

[45] D. K. Remler, P. A. Madden, *Mol. Phys.* **1990**, *70*, 921.

[46] G. Pastore, E. Smargiassi, F. Buda, *Phys. Rev.* **1991**, *44*, 6334.

CHAPTER 3

Structural studies of the 1:1 adduct formed between squaric acid and 4,4'-bipyridine

3.1. Introduction

Proton migration and proton transfer phenomena are found in many chemical and biological processes and are therefore worthy of exploration by both experimental and theoretical methods.[1-3] In the case of organic molecular crystals, with which this work is concerned, the impetus of external stimuli such as temperature or pressure are generally required.[4-13] The system that forms the focus of this chapter is the adduct formed between squaric acid (SQ) and 4,4'-bipyridine (BIPY) as shown in Figure 3.1, hereafter denoted SQBP. This was selected for study on account of a previous report which suggested temperature-induced proton transfer.[9]

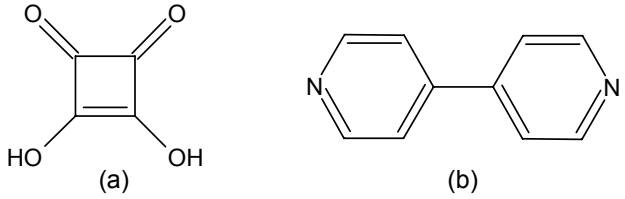

Figure 3.1. a) Squaric acid, b) 4,4'-Bipyridine.

Squaric acid is a diprotic acid (pK_{a1} = 1.2–1.7, pK_{a2} = 3.2–3.5),[14, 15] that can crystallise as (i) the neutral squaric acid molecule (SQH_2),[16, 17] (ii) the hydrogen squarate anion (SQH^-, *e.g.* in the 1:1 adduct of SQBP – see section 3.2)[9, 18-20] or (iii) as the squarate di-anion (SQ^{2-}, *e.g.* in the 3:2 adduct of SQBP – see section 3.2).[20-22] Both anions and the neutral molecule can participate in hydrogen bonding. Squaric acid and its anions are almost perfectly flat molecules on account of π-conjugation of the C=C and C=O bonds. Resonance is known to stabilise the mono-anion, and to a greater extent the di-anion, when compared to pure squaric acid (see Figure 3.2).[23, 24]

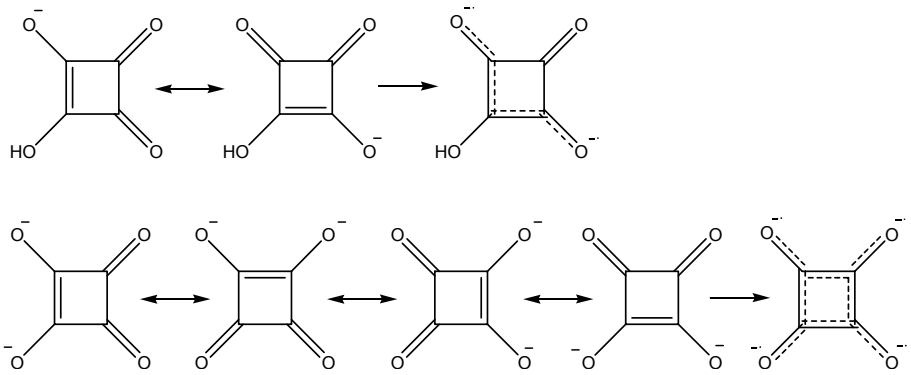

Figure 3.2. Scheme showing the possibilities of delocalisation for the mono-anion and the di-anion.[24]

4,4'-Bipyridine is a rather rigid, weak, bidentate base (pK_{a1} = 2.7–2.9 for $BIPYH^+$ and pK_{a2} = 4.8–4.9 for $BIPYH_2^{2+}$).[25, 26] Both nitrogen atoms can act as hydrogen bond acceptors and there are some instances in which C–H···O interactions can be formed.[27] Another factor that makes this ligand an important moiety in supramolecular chemistry and crystal engineering is the possibility of π-π stacking. The stacking of aromatic rings can occur in three different ways: (i) perfectly aligned, face-to-face or 'sandwich'; (ii) offset, slipped or parallel displaced; or (iii) T-shaped or point-to-face (see Figure 3.3).[28]

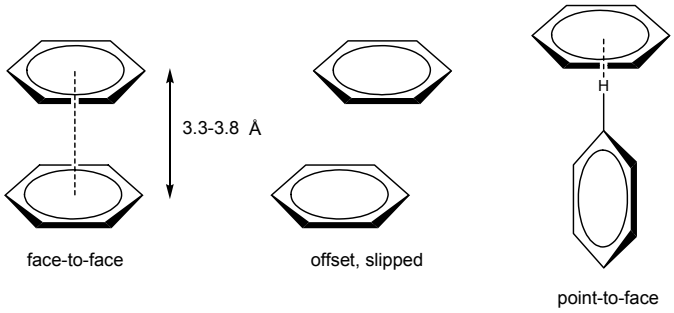

Figure 3.3. Schematic of the possible modes of ring stacking for benzene.[28]

The π-π interactions, although poorly directional and energetically weaker than hydrogen bonds (calculated energies of *ca.* 7.5 kJ mol^{-1} for the face-to-face and 11 kJ mol^{-1} for the slipped and T-shaped conformations in the case of benzene dimers), can appreciably stabilise crystal packing arrangements.[28-30]

3.2. Previous work

Reetz *et al.*[9] showed that dissolution of a 1:1 mixture of 4,4'-bipyridine and squaric acid in hot water produced a pale, yellow-brown precipitate (see Figure 3.4). On recrystallisation at ambient temperature the bulk of the material was obtained as pale, ochre, rectangular crystals which displayed a λ_{max} = 390 nm. Single crystal X-ray diffraction studies showed this to be a 1:1 adduct that crystallised in the monoclinic crystal system (see Table 3.1) The authors denoted this as form I. Reetz *et al.* also identified another form that crystallised as slightly darker crystals and for which λ_{max} = 460 nm. Single crystal X-ray diffraction studies showed this to be a triclinic polymorph (hereafter labelled form III).

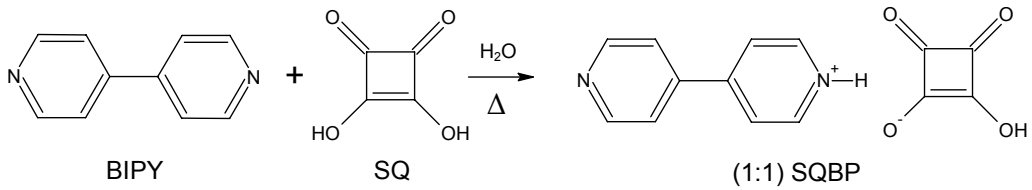

Figure 3.4. Formation of the 1:1 adduct.

Table 3.1. Crystal details for SQBP forms I and III as determined by Reetz *et al*.[9]

	Form I		Form III
Chemical formula	$C_{14}H_{10}N_2O_4$		$C_{14}H_{10}N_2O_4$
M_r (g mol^{-1})	270.24		270.24
Crystal system, space group	monoclinic, $P2_1/n$		triclinic, $P1$
Temperature (K)	183	293	173
a	3.758(1)	3.800(1)	9.619(1)
b	11.196(1)	11.208(1)	10.679(2)
c (Å)	27.351(2)	27.447(2)	12.726(4)
α	90	90	70.17(3)
β	92.95(1)	92.22(1)	85.83(2)
γ (°)	90	90	70.08(1)
V (Å^3)	1149.26(68)	1168.10(56)	1154.78(1391)
Z	4	4	4
ρ_{calc} (g cm^{-3})	1.562	1.537	1.55

The results of differential scanning calorimetry (DSC) showed that form I undergoes a thermally reversible transition to a new red form (designated form II) on heating to 453 K. An energy uptake of 5.4 kJ mol^{-1} was observed for this transformation. On cooling to below 423 K, the colour of the crystal changed back to yellow, but only 4.2 kJ mol^{-1} were released. Subsequent heating and cooling gave the red form at 446 K and the yellow form below 423 K, accompanied by an uptake and release of 4.2 kJ mol^{-1}. Further heating and cooling had no effect on the transition temperature or the magnitude of the energy changes. On the basis of this evidence the authors suggested that the yellow form produced on cooling below 423 K was a fourth polymorph.

Partial deuteration of the adduct was achieved by utilizing squaric acid-d_2 in the preparation. On heating to 453 K, no colour change was observed and this led the authors to suggest that the temperature-induced colour change obtained from heating form I was due to proton transfer.

The authors also reported preliminary results of the response of the adduct to pressure, whereby a hydrostatic pressure of 11 kbar was applied to a sample for 60 seconds. After decompression, X-ray powder diffraction and UV-visible data were collected and appeared similar to those obtained at high temperature. On this basis the authors suggested that the temperature-induced phase transition could also be induced *via* pressure.[9]

In a later study by MacLean *et al.*,[20] a SQBP adduct with a different composition was obtained in the form of very thin orange plates from crystallisation of stoichiometric quantities of squaric acid and 4,4'-bipyridine in methanol. This phase was identified by single crystal X-ray diffraction as the 3:2 adduct of SQBP (see Figure 3.5). This phase contained doubly protonated bipyridine molecules and both SQH^- and SQ^{2-} anions. The SQH^- anions aggregate to form dimers, whilst the SQ^{2-} anions connect to the bipyridine ions ($BIPYH_2^{2+}$) through two independent N–H···O bonds of length *ca.* 2.6 Å.

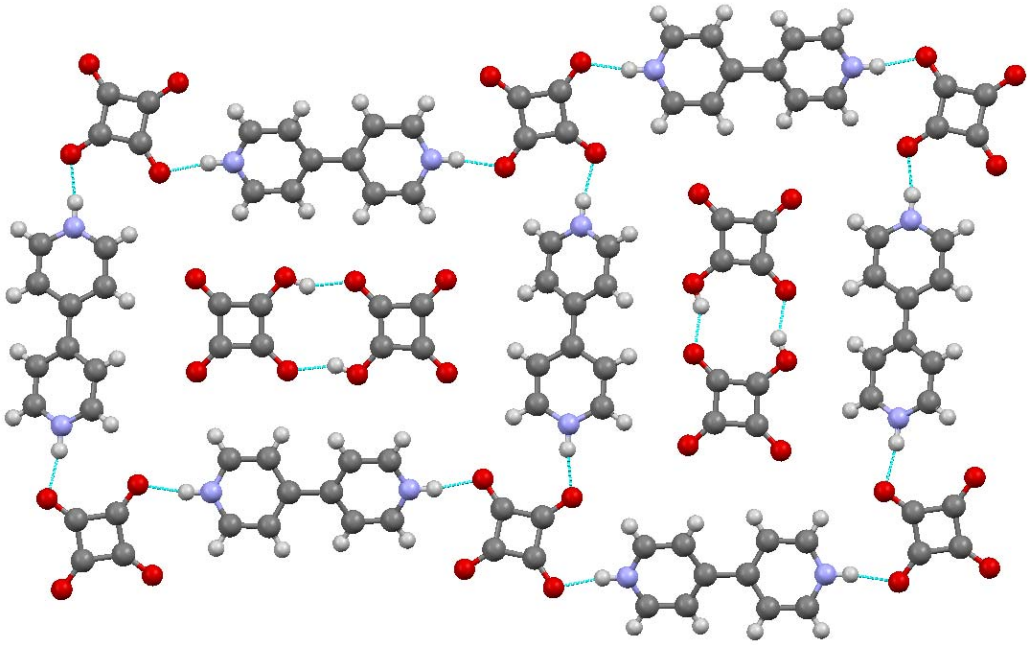

Figure 3.5. View of the (103) planes of the 3:2 SQBP adduct.[20]

These previous studies have therefore described some interesting systems that may undergo temperature-induced proton transfer resulting in colour changes. For the 1:1 adduct, form I is known to comprise monoprotonated SQ and BIPY molecules, but the structure of the high-temperature (red) form II is unknown.

The objectives of this project were therefore to:

- determine the crystal structure of the high-temperature form II in order to identify the extent of protonation of the BIPY molecules;

- identify and characterise the form obtained by cooling form II below 423 K;
- to use complementary computational techniques to (i) identify the extent of protonation of BIPY molecules in form II, (ii) assess the energetics of any proton transfer process, and (iii) to identify the cause of the colour change between forms I and II.
- determine whether the form produced at high pressure is in fact the same as that produced at high temperature.

3.3. Experimental section

3.3.1. Materials

Squaric acid (SQ) and bipyridine (BIPY) were obtained from Sigma-Aldrich and used as received. Crystals of the 1:1 adduct of SQBP were grown by combining equimolar quantities of both precursors [0.44 g (3.97 mmol) of SQ with 0.62 g (3.86 mmol) of BIPY] in approximately 500 cm^3 of hot water. Repeated recrystallisation of SQH_2 from deuterium oxide (D_2O) gave deuterated squaric acid ($SQ\text{-}d_2$). Deuterated BIPY ($BIPY\text{-}d_8$) was obtained by substitution of the H-atoms under solvothermal synthesis conditions previously reported by Browne *et al*.[31] Crystallisation of the perdeuterated adduct ($SQBP\text{-}d_{10}$) was prepared by combining equimolar quantities of $SQ\text{-}d_2$ and $BIPY\text{-}d_8$ [0.23 g (1.98 mmol) and 0.32 g (1.95 mmol)] in approximately 100 cm^3 of D_2O. In every case crystals suitable for X-ray analysis were obtained by slow cooling of a bath from 343 K to room temperature over a period of 12 hours.

3.3.2. Differential scanning calorimetry

Differential scanning calorimetry (DSC) traces in the temperature range of 200 to 500 K were collected on a Pyris 1 differential scanning calorimeter equipped with *Pyris Thermal Analysis System 3.81*.[32] Short isothermal steps were imposed at the beginning of each heating and cooling cycle so that equilibration could be

achieved. Accurately weighed samples (mass ~ 2 mg) were loaded into aluminium pans which were then hermetically sealed. Heating and cooling scan rates of 100 K min^{-1}, typical of HyperDSC, were used. Helium gas was constantly flushed through the system during all experiments to disperse the heat and to purge any volatile products that may react with the platinum resistance wires. Nitrogen gas was used to maintain dry conditions within the furnace.

3.3.3. Variable temperature visible and IR spectroscopies

The infrared and visible spectra of the crystals were recorded with a Bruker Equinox-55 spectrometer linked to a Hyperion microscope attachment.[33] Temperatures were controlled using a LINKAM LTS350 temperature stage – fitted with potassium bromide windows and purged with nitrogen gas – connected to a LNP94 cooling stage and controlled by a CI94 interface. The detectors used for the visible and IR regions of the electromagnetic spectrum were a silicon diode and mercury cadmium telluride (MCT), respectively. Data were collected over the spectral ranges of 25000–8500 cm^{-1} (at a resolution of 8 cm^{-1}) and 6000–600 cm^{-1} (at a resolution of 2 cm^{-1}) within the temperature range 298–488 K. Corrections for background absorption were achieved by automatic subtraction of the spectrum of the empty temperature stage from the sample spectra.

3.3.4. Variable temperature diffraction studies

3.3.4.1. Single-crystal X-ray diffraction

Diffraction data were collected using a Bruker-SMART Apex CCD diffractometer equipped with an Oxford Cryosystems low temperature device at temperatures of 180, 298 and 453 K, using Mo-Kα radiation (λ = 0.71073 Å). Data integration and reduction was performed using *SAINT* (Bruker Nonius).[34] An absorption correction was applied using the multiscan procedure program *SADABS*.[35] Structures were solved by direct methods using the *SIR92*[36] package, and refined using full-matrix least squares against $|F|^2$ using *CRYSTALS*.[37] The non-hydrogen atoms were refined with anisotropic thermal parameters. Hydrogen atoms associated with C–H bonds were placed in geometrically calculated positions

and allowed to regularise with respect to Fourier difference peaks. Hydrogen atoms associated with N–H and O–H bonds were placed, in the case of form I at low temperature (LT), through the use of Fourier difference maps with a subsequent riding model being applied. At high temperature (HT) location of these hydrogen atoms was not possible.

3.3.4.2. Powder neutron diffraction

Variable temperature diffraction data for SQBP-d_{10} were initially collected on the time-of-flight high-resolution powder diffractometer (HRPD)[38] at the ISIS pulsed neutron source. The sample was placed in a 5 mm diameter cylindrical can and was heated using a vanadium element furnace. Data were recorded over a time-of-flight range between 30 and 130 ms. Diffraction data were recorded at 292 K for a period of approximately 15 hours. In the region between 473 and 483 K, data were recorded at 5 K intervals for *ca.* 10 minutes in order to investigate the point at which the phase transition was complete; the remainder of the time available for this experiment, *ca.* 10 hours, was used to collect data at 488 K.

Data from gently ground crystals of the hydrogenous sample (SQBP ≈ 0.75 g) were also collected on the D20 high-flux instrument at the Institut Laue-Langevin (λ = 1.4965 Å) over the temperature range 120–473 K.[39] The diffractometer operated in high-resolution mode.[40] No attempt was made to optimise the data collection method in terms of wavelength or sample mounting. The patterns were corrected for attenuation due to the strong incoherent scattering from hydrogen and the moderately strong preferred orientation along the *b*- axis (010). This was done following the protocol given in the International Tables C section 6.3.3 for a cylindrical can with μR = 0.90,[41] and calculated assuming a 100 % packing efficiency (generally 50–80 % depending on the powder grain size and habit) as a safety factor for the correction.[42] Data reduction was achieved using the standard data reduction protocols for the D20 instrument in *LAMP*.[43] Full-profile Rietveld[44] refinements of the resulting patterns were performed by Bill Marshall and Kevin Knight using *PC-GSAS*[45] as implemented in the *EXPGUI*[46] package. The starting models used for both LT and HT structures were those obtained by X-ray diffraction

techniques. Geometrical restraints and thermal parameter constraints based on the X-ray structure were used in order to enhance the observable data to parameters ratio. Background parameters (shifted Chebyschev with 8 and 12 terms for forms I and II, respectively) and scale factor were also refined. The figures of merit obtained were $R(F^2)$ = 0.1060 and χ^2 = 207.2 for the LT collection and $R(F^2)$ = 0.2713 and χ^2 = 72.80 for the HT collection.[42]

3.3.4.3. Powder X-ray diffraction

Temperature-controlled experiments were performed on the high-resolution powder X-ray diffractometer of beamline ID31 at the ESRF, Grenoble[47, 48] with a wavelength of 0.801003(3) Å.[49] Sufficient quantities (~ 4 mg) of SQBP form I crystals were lightly ground and introduced into thin-walled borosilicate glass capillaries (1.5 mm diameter). The capillaries were mounted on the axis of the diffractometer and rapidly rotated during measurements in order to improve randomisation of the orientations of the individual crystallites. The capillary was heated (293–493 K) by means of an Oxford Cryosystems Cryostream device mounted parallel to the capillary. Lattice parameters were obtained from Pawley[50] refinements, performed by Norman Shankland and Kenneth Shankland, in the 2θ range 2–40° using the programs *TOPAS* and *DASH*.[51, 52]

3.3.5. Computational modelling

3.3.5.1. Geometry optimisation

Equilibrium structures for SQBP forms I and II were obtained using the *CPMD*[53] simulation package.[54] Initial geometries, unit cells and space group symmetry constraints were taken from the X-ray experiments, with the hydrogen atoms placed manually on the BIPY molecule in the case of the high temperature form. Electronic exchange and correlation were modeled using the gradient-corrected functional of Perdew, Burke and Ernzerhof (PBE).[55, 56] Core electrons were treated using a set of Vanderbilt ultra-soft pseudopotentials, while valence electrons were represented by a plane-wave basis set truncated at an extended energy cutoff of 30 Ry. It should be noted that as the *a*- axis of the form I structure is considerably

shorter than the other two axes, this simulation was performed on a 3×1×1 supercell in order to create a simulation model of more cubic dimensions. The electronic band structures were then sampled at the Γ- point only.

3.3.5.2. Potential energy surfaces

A series of single-point energy calculations were undertaken where proton positions were shifted in set increments along the N···O hydrogen bonds.[54] Two sets of calculations were performed. The first were on the form I structure (*i.e.* $SQH^-.BIPYH^+$) where a proton was pulled from the SQ molecules to the BIPY molecules, thereby approximating the form I to form II transition. The second set of calculations were on the form II structure (*i.e.* $SQ^{2-}.BIPYH_2^{2+}$) where a proton from the BIPY molecules was stepped back across to the SQ molecules, approximating the potential energy scans (PES) for the reverse reaction.

3.3.5.3. Molecular dynamics

Molecular dynamics (MD) simulations, within the NVT ensemble, were carried out at 180 K for form I and 350 K for form II with a time step of 3.0 a.u., coupled to Nosé-Hoover thermostat[57, 58] chains for each vibrational degree of freedom at a characteristic frequency of 3000 cm^{-1}.[54] An electronic mass parameter of 400 a.u. was employed.

3.3.5.4. Properties

Localised basis set calculations on the form I and form II forms were performed by Derek Middlemiss using the *CRYSTAL06*[59] code. The crystalline orbitals were expanded in terms of bases of localised Gaussian-type functions, of varying extents. The B3LYP[60-62] hybrid functional was selected on the basis that previous studies have shown that it yields widths of band gaps in good agreement with experimental data in a wide variety of compounds.[63, 64] The methods used, however, are known to provide a poor representation of weak intermolecular interactions. Thus forcing the adoption of a strategy where the atomic positions were optimised within the fixed volume and lattice vectors of the experimental unit cells.

The optimisations employed a total energy convergence tolerance of 10^{-7} a.u., and were pursued until RMS gradients and displacements fell below 3×10^{-4} and 1.2×10^{-3} a.u., with tolerances for the maximum component and maximum absolute value of 1.5 times the RMS setting. Results relating to the convergence in total energies with respect to the basis set size and the density of Monkhorst-Pack sampling[65] of reciprocal space are presented in Table 3.6. It is evident that the relative stabilities of the two forms change markedly with progress from the smaller 6–31G*[66-68] to the larger 6–311G**[69, 70] basis sets, due no doubt to the introduction of polarisation functions at H sites in the latter. Issues of the tractability and numerical stability of the self-consistent process render the use of larger sets impractical. It should also be noted that the 4×4×4 Monkhorst-Pack mesh provides excellent convergence. The latter basis set and mesh are adopted in all subsequent calculations. The details of the electronic structure and charge distributions are obtained within the optimised structures of both forms from atom-projected densities-of-states plots and Mulliken analyses respectively.

Finally, some components of the work benefit from a comparison with isolated molecule calculations. These were performed by Derek Middlemiss using the *Gaussian03* suite of programs,[71] adopting the same B3LYP Hamiltonian as the periodic simulations,[60-62] but employing larger 6–311++G**[69, 70] basis so as to provide the diffuse functions necessary for the proper representation of the anionic states of the SQ molecule.[72] It should be noted that this extensive basis is not required in the solid state calculations due to the presence of functions at neighbouring sites which may enter into the expansion of extended electronic states. Harmonic vibrational analyses were performed subsequent to the optimisations.

3.3.6. Variable pressure diffraction studies

3.3.6.1. Single-crystal X-ray diffraction

Diffraction data were collected on Station 9.8 at the STFC Daresbury Laboratory, with a Bruker APEX 2 CCD diffractometer at 293 K using synchrotron radiation (λ = 0.6711 Å). The experiments focused on direct compression (0 to

32 kbar) of a single crystal of form I under hydrostatic conditions. For this purpose a Merrill-Bassett diamond-anvil cell (DAC)[73] equipped with 800 μm culet diamonds and tungsten gasket with a 300 μm hole. A single crystal of SQBP form I was loaded with a small piece of ruby and 4:1 methanol-ethanol, acting as the pressure calibrant and pressure-transmitting medium, respectively.

3.3.6.2. Powder X-ray diffraction

Variable pressure X-ray powder diffraction experiments were performed at the STFC Daresbury Laboratory on Station 9.5HPT using apparatus described by Lennie *et al*.[74] Crystals of form I SQBP were gently ground and loaded, along with 4:1 methanol-ethanol (pressure-transmitting medium), at 293 K into a DAC[73] equipped with 800 μm culet diamonds and a tungsten gasket. The pressure within the gasket hole (300 μm) was determined by measuring the fluorescence from a small piece of ruby on excitation with a 532 nm, 10 mW diode laser.[75]

3.3.6.3. Powder neutron diffraction

High-pressure time-of-flight powder neutron diffraction data were collected for SQBP-d_{10} using the PEARL-HiPr instrument located at the ISIS Neuron Facility at the Rutherford Appleton Laboratory.[76, 77] This experiment used a type V3b Paris-Edinburgh cell[78, 79] equipped with standard WC/Ni-binder toroidal anvils and TiZr capsule gaskets (55 mm^3 initial volume).[80] The refined diffraction patterns were obtained after focussing the individual detector element spectra to a common time-of-flight scale, normalisation of the summed data with respect to the incident beam monitor and the scattering from vanadium sample and correction for the wavelength and scattering-angle dependence of the neutron attenuation by the anvil (WC) and gasket (TiZr) materials.[81] Full-profile Rietveld refinements of the resulting patterns were attempted using *PC-GSAS*[45] as implemented in the *EXPGUI*[46] package.[42] The perdeuterated adduct was gently ground and loaded into a standard capsule gasket along with a ~ 1 mm diameter lead pellet, the latter being present to act as a pressure calibrant.[82-85] Once loaded into the Paris-Edinburgh press, the sample was sealed within the capsule using an initial applied load of

7 tonnes. The applied load and, hence, the sample pressure, was then varied and monitored by means of a computer-controlled hydraulic oil pressure system connected to the *in situ* hydraulic ram of the press. In the time available for this experiment, data were collected at 11 pressure points (including two decompression shots) at cell loads between 0 kbar and 31 kbar, with data collection times ranging between 30 minutes and 6 hours.[86]

3.4. Variable temperature studies - results and discussion

3.4.1. General characterisation

Using the procedure described by Reetz *et al*., yellow, plate-like crystals of SQBP were obtained at room temperature.[9] Single crystal X-ray diffraction confirmed that these were the monoclinic form I. On heating to *ca*. 453 K the crystals turned red with no apparent disintegration. This red form was presumed to be form II (see Figure 3.6).

Figure 3.6. Optical image of a single-crystal of form I (yellow) and the result of increasing the temperature to give form II (red).

The change of colour from yellow to red is associated with a shift in the absorption of light to longer wavelengths. This was quantified using solid-state VT-visible spectroscopy (see Figure 3.7). At ambient temperatures, an absorption band centred at 450 nm was observed for form I. This is somewhat different from the position of 390 nm reported by Reetz *et al*. This may reflect the fact that the lower limit of data collection in the present study was 400 nm and so a band centred at 390 nm might not be detected.

At 488 K a new absorption band centred at 540 nm appeared and is consistent with the observed colour change. The apparent higher temperature of the transition reflects the poor thermal contact of the crystal on the heating stage. In order to protect the KBr window from possible attack at these elevated temperatures, the crystal was mounted on a glass cover-slip and this would have restricted heat flow between the hot stage and the crystal.

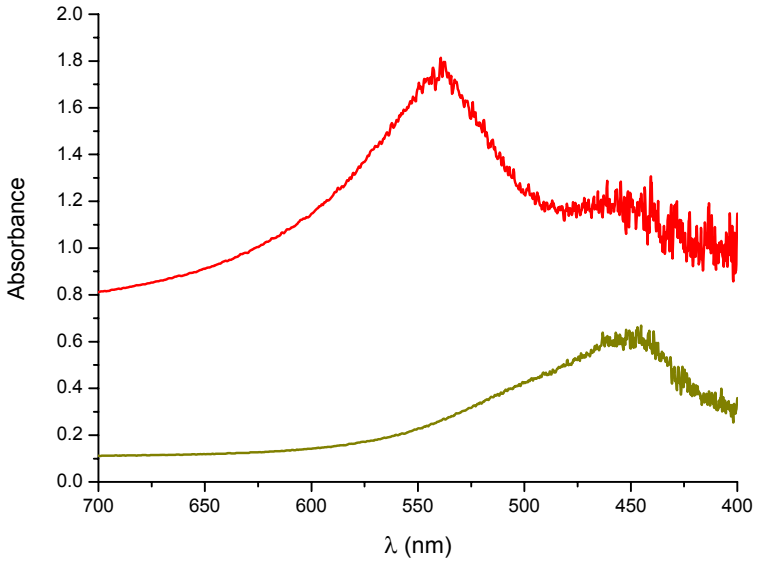

Figure 3.7. Visible spectra of a single crystal of SQBP as a function of temperature. The dark yellow line represents form I at 298 K and the red line represents form II at 488 K.

VT-infrared spectra were also collected on a crystal in order to characterise the phase transition. Direct comparison of both LT and HT spectra was only possible in the region 2000–4000 cm^{-1} on account of the strong absorption of the form II crystal in the region below 2000 cm^{-1} combined with the increased scattering from the sample, presumably as a consequence of decreased crystal quality (see Figure 3.8). A difference between the two spectra was observed, with the appearance of a new band at 3050 cm^{-1} in form II. This region of the spectrum corresponds to aromatic C–H stretching modes and hydrogen-bonded N–H modes. Hence the

appearance of this band at high temperature suggests either changes in the aromatic ring of the BIPY molecule or changes associated with transfer of a proton towards a nitrogen atom of a BIPY molecule.

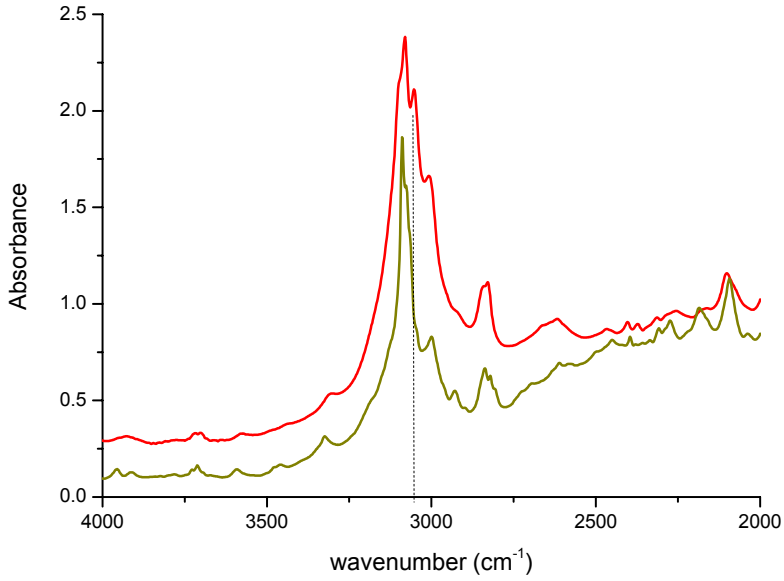

Figure 3.8. IR of a single crystal of SQBP as a function of temperature. The dark yellow line represents form I at 298 K and the red line represents form II at 488 K. The dashed black line is an aid to visualisation of the new band.

The results obtained in the DSC experiments (see Figure 3.9) agree with those previously reported.[9] When starting from a fresh sample of form I a phase transition to form II occurred at 453 K with an endothermic event of *ca.* 5.5 kJ mol^{-1}. Upon cooling the reverse transition occurred at 426 K with the release of ~ 3.5 kJ mol^{-1}. Subsequent cycling of the temperature led to transitions at 446 K (with an endotherm of 4.5 kJ mol^{-1}) and 426 K (with an exotherm of 2.5 kJ mol^{-1}) for the heating and cooling stages, respectively. In subsequent heating cycles the phase transition was observed at 447 K with an endotherm of 4.4 kJ mol^{-1}. Crystals recovered at the end of the experiment appeared shattered and of slightly darker colour. It should be noted that, for the first cycle of heating, multiple peaks were

observed. This may be due to poor initial surface contact between the individual crystals and the heater. This effect appeared reduced for subsequent heating cycles, presumably as a consequence of physical movement of the crystals during the phase transition and hence improved thermal contact.

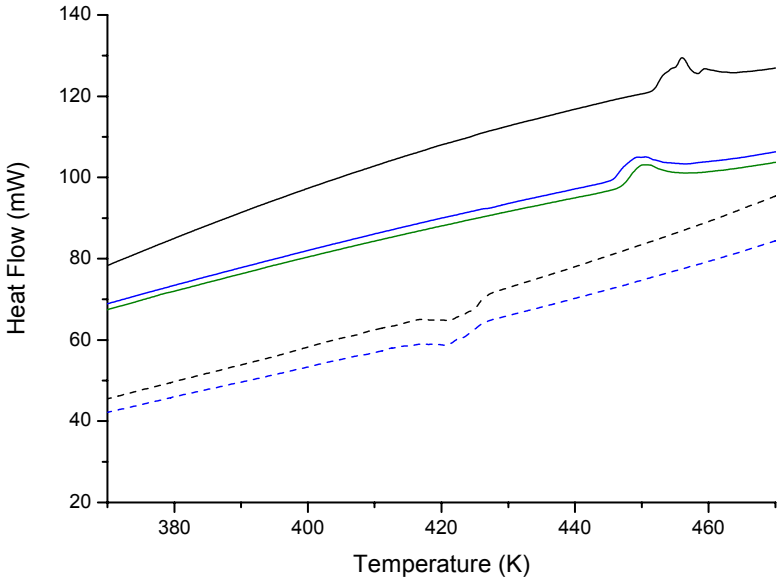

Figure 3.9. DSC traces for (1:1) SQBP at heating and cooling rates of 100 K min^{-1}. The solid lines represent the heating processes while the cooling stages are dashed. Black represents the initial cycle, followed by blue (second cycle) and green (partial third cycle).

These results are consistent with two possible hypotheses. The first is that heating form I to above 453 K causes the formation of form II, which on cooling to 426 K transforms to a new form IV. On heating form IV above 447 K, it transforms back to form II. This is the hypothesis presented by Reetz,[9] and the authors supported it by reference to the powder X-ray diffraction pattern and UV-visible spectrum of the post-heated material recovered to ambient temperature. The diffraction pattern and absorption coefficients of the UV-visible spectrum were apparently different from those obtained for form I. The second hypothesis is that on cooling form II below 426 K, only a proportion of it transforms back to form I

i.e. the transition is not fully reversible owing to kinetic factors. Subsequent re-heating of this mixed phase would therefore result in a lower transition temperature with a smaller endotherm. Both of these hypotheses are explored in greater detail in section 3.4.4.

3.4.2. Single-crystal X-ray diffraction studies

SQBP crystallises in space group $P2_1/n$ with one SQH^- anion and one $BIPYH^+$ cation in general positions of the asymmetric unit cell (see Figure 3.10). This leads to a unit cell comprising four molecules of each of the components. The chains of alternating BIPY and SQ molecules deviate from a perfectly linear plane by 6–10°.

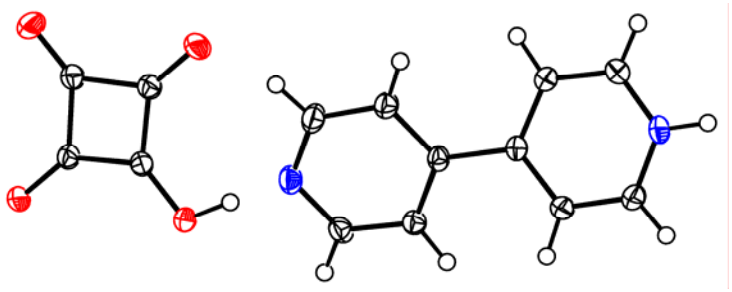

Figure 3.10. The asymmetric unit of SQBP form I at 183 K. Displacement ellipsoids are drawn at the 50 % probability level.

Squaric acid and bipyridine molecules (with a torsion angle between the heterocyclic rings of approximately 24.3°) are connected primarily through strong N–H···O (2.60 Å) and O–H···N (2.61 Å) hydrogen bonds that form $C_2^2(14)$ chains parallel to the (103) planes, but also through auxiliary close CH···O contacts (2.35 and 2.40 Å).[87] These chains are interconnected by several close contacts between CH···O atoms (ranging from 2.46 to 2.66 Å; the sum of the van der Waals radii for O and H is 2.72 Å) (see Figure 3.11). These close contacts are not coplanar with the chains and enable the rings to stack in a slipped conformation with an interlayer distance of around 3.3 Å [see Figures 3.12 (a)]. Furthermore, the neighbouring stacks are offset thereby stabilising the crystal structure [see Figures 3.12 (b)].

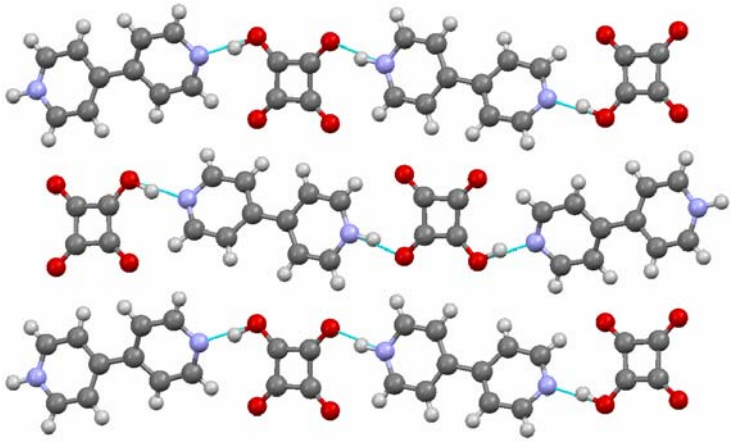

Figure 3.11. The crystal structure of SQBP form I viewed along the *a*- axis.

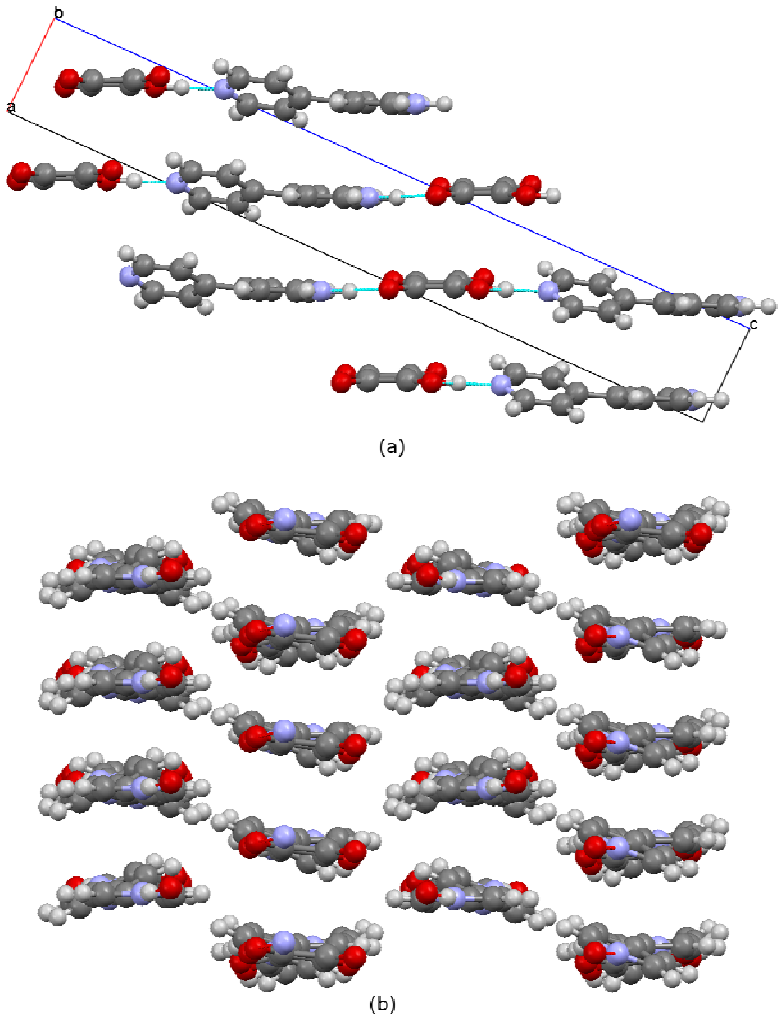

Figure 3.12. Form I SQBP (180 K) view: (a) of the *ac* plane; and (b) along the (103) planes.

In situ heating of a crystal of form I to 453 K on the diffractometer resulted in a single-crystal to single-crystal phase transition to form II. The fact that the crystal remained intact is indicative that the crystal structures of both forms have many similarities. The lattice parameters of the two forms are related, such that the *a*- axis triples and the *c*- axis is reduced to a third (see Table 3.2).

Table 3.2. Crystal details for SQBP forms I and II.

	Form I		**Form II**
Chemical formula	$C_{14}H_{10}N_2O_4$		$C_{14}H_{10}N_2O_4$
M_r (g mol^{-1})	270.24		270.24
Crystal system, space group	monoclinic, $P2_1/n$		monoclinic, $C2/c$
Temperature (K)	180	298	453
a	3.7551(5)	3.7975(1)	12.359(8)
b	11.2066(13)	11.1996(3)	11.287(7)
c (Å)	27.322(3)	27.4424(7)	9.061(6)
β (°)	92.947(7)	92.236(2)	109.139(10)
V (Å^3)	1148.2(2)	1166.25(5)	1194.1(13)
Z	4	4	4
ρ_{calc} (g cm^{-3})	1.563	1.539	1.492
Radiation type	Mo *K*α	Mo *K*α	Mo *K*α
Crystal form, colour	Plate, yellow	Plate, yellow	Plate, red
Crystal size (mm)	0.10 x 0.35 x 0.45	0.10 x 0.35 x 0.45	0.11 x 0.22 x 0.43

Form II adopts the monoclinic crystal system with space group *C*2/*c*. The asymmetric unit of form II contains half a molecule of SQ and BIPY (with a torsion angle between the pyridine rings of 0°) that lie on a 2-fold axis and an inversion centre (see Figure 3.13). It should be noted that because of the high temperature at which the data were collected H atom placement on the BIPY was restricted to geometrically sensible positions.

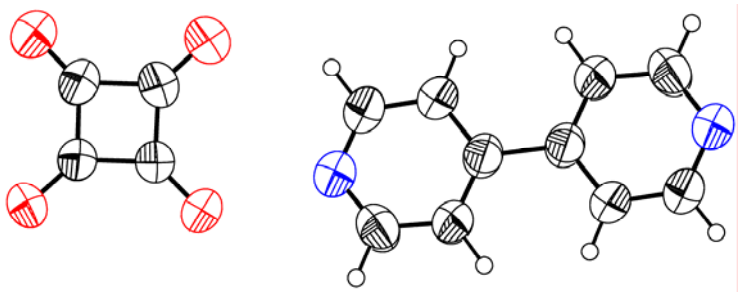

Figure 3.13. Extended asymmetric unit of SQBP form II at 453 K with only the geometrically placed hydrogen atoms shown. Displacement ellipsoids are drawn at the 50 % probability level.

The unit cell comprises four molecules of BIPY and four molecules of SQ, as with form I, but the relative orientations of the alternating molecules are now essentially flat throughout (3.1°). The pattern of hydrogen bonding is maintained, with N···O distances of 2.55 Å. The $C_2^2(14)$ chains are retained and now lie on the (30-2) planes. The auxiliary close CH···O contacts (2.36 Å) are also present. The stacks of chains remain slipped and connected through several close contacts between CH···O atoms (2.46 and 2.54 Å; the sum of the van der Waals radii of O and H is 2.72 Å). As before, π-π stacking is offset, but because of the higher thermal motion this led to a slightly increased intermolecular distance of 3.6 Å. Furthermore, the molecules appear to slip (*ca.* 13°) during the phase transition (see Figure 3.14). The arrangement of the molecules and consequent stability of the lattice will be discussed further in section 3.4.6.

Selected parameters for both forms of SQBP are shown in Table 3.3, following the numbering scheme for the SQ molecule presented in Figure 3.15.

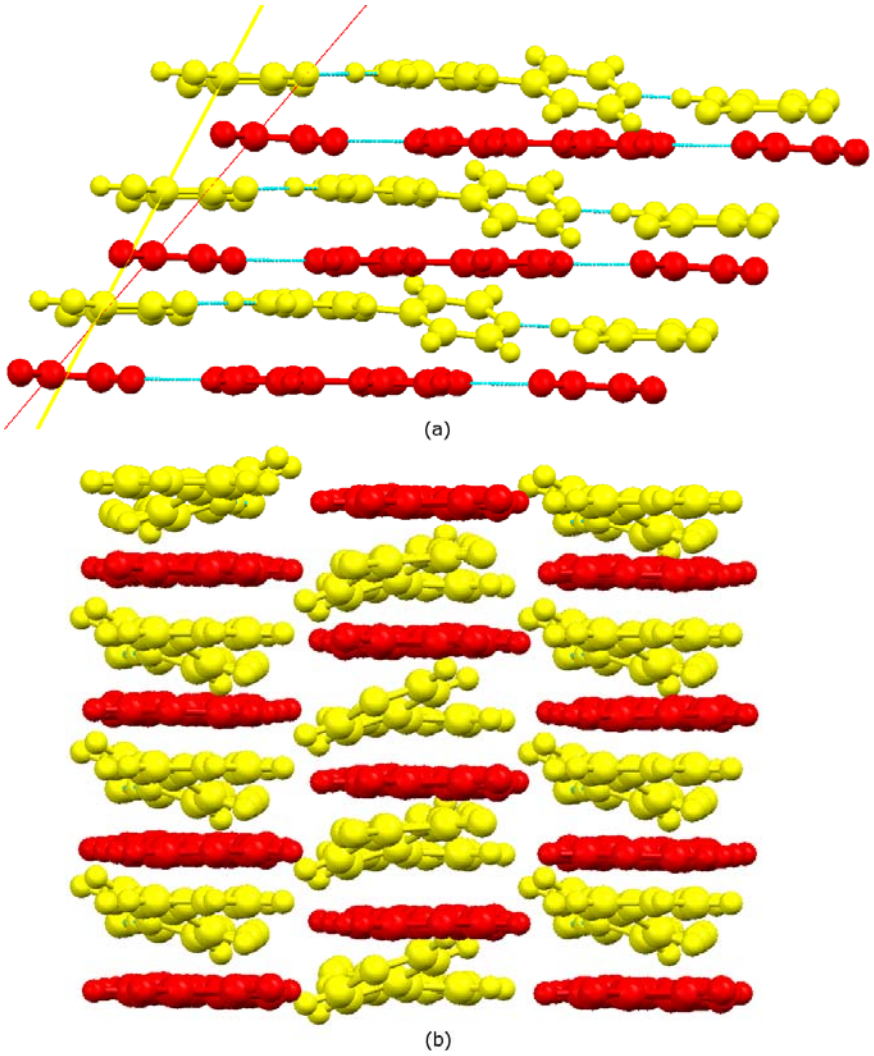

Figure 3.14. Comparison of form I (yellow) and form II (red) SQBP (a) viewed along the b axis and (b) viewed along the (103) and (302) planes, respectively. The calculation of the slipping angle was based on the yellow and red planes.

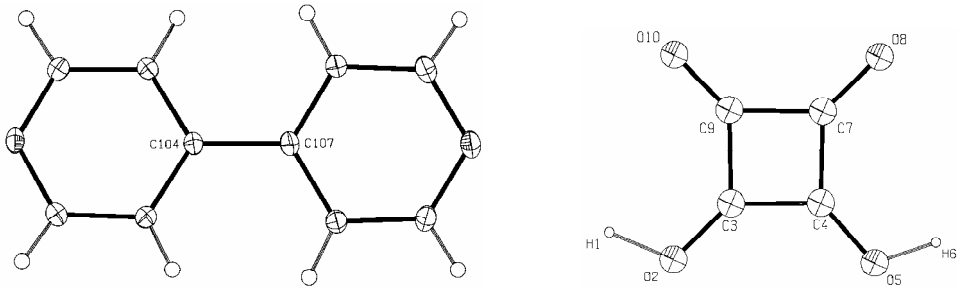

Figure 3.15. The numbering scheme used in Table 3.3 and for the CSD[88] search for the SQ and BIPY molecules (see Tables 3.4 and 3.5, respectively). Note H_1 has been arbitrarily assigned as the more labile hydrogen atom.

Table 3.3. Comparison of selected parameters from experimental and computed structures for forms I and II of SQBP (distances in Å, angles in degrees).

Geometry	Form I (LT)				Form II (HT)		
	X-ray (180 K)	X-ray (298 K)	Neutron (120 K)	Calculated	X-ray (453 K)	Neutron (473 K)[a]	Calculated
SQ							
C_3=C_4	1.419(2)	1.417(2)	1.477(19)	1.441	1.436(4)	1.447(5)	1.463
C_4–C_7 / C_3–C_9	1.452(2) / 1.490(2)	1.444(2)	1.510(21) / 1.483(21)	1.463 / 1.497	1.446(5)	1.497(3)	1.493
C_7–C_9	1.504(2)	1.502(2)	1.474(23)	1.507	1.465(5)	1.468(5)	1.506
O_2–C_3 / C_4–O_5	1.265(2) / 1.311(2)	1.262(2) / 1.309(2)	1.234(23) / 1.242(22)	1.270 / 1.309	1.267(4)	1.256(21)	1.256
C_7=O_8 / C_9=O_{10}	1.228(2) / 1.221(2)	1.225(2) / 1.218(2)	1.254(25) / 1.236(25)	1.245 / 1.238	1.225(4)	1.247(21)	1.236
O_5–H_6	0.928(9)	0.887 (1)	1.007(32)	1.105	—	—	—
BIPY							
C···N	1.343(4) / 1.338(6) [b]		1.319(20) / 1.323(21) [b]	1.350(2) / 1.347(3) [b, f]	1.311(5)	1.341(16)	1.356(4)[f]
N–H_1 / N–H_6	0.938(1) / —	0.910(1)	1.049(22) / —	1.096 / —	—	1.071(15)	1.065
C_{104}–C_{107} [c]	1.483(2)	1.486(2)	1.541(19)	1.479	1.526(4)	1.566(8)	1.446
τ BIPY [d]	24.3(2)	24.2(2)	24.3(17)	24.0	0.0(5)	0.0	0.0
r Interlayer [e]	3.31(2)	3.36(2)	3. 34(2)	3.43	3.63(4)	3.50(2)	3.57
H-bonding							
N···O_2 / N···O_5	2.597(2) / 2.611(2)	2.605(2) / 2.628(2)	2.568(20) / 2.645(21)	2.553 / 2.613	2.554(3)	2.567(14)	2.620
∠ C_3–O_2–N / C_4–O_5–N	118.22(7) / 114.79(7)	118.34(9) / 114.83(9)	113.88(121) / 122.04(118)	115.48 / 117.46(1)	117.84(2)	117.21(69)	115.62

a – Neutron diffraction structure refined using geometrical restraints and thermal parameter constraints derived from the X-ray structure; b – Note that in the case of form I ($SQH^-.BIPYH^+$) the first value refers to C–NH bonds and the second to C–N bonds (*i.e.* with no H atom connected to the nitrogen); c – Distance between the individual pyridine rings; d – Calculated based on the angle formed between the planes of the individual pyridine rings; e – Measured between the planes formed by the adduct molecules that lie parallel to each other (see Figure 3.14); f – Averaged value of those existing in the calculated structure.

Owing to the high temperature at which the data for form II were collected, it was not possible to locate the position of the hydrogen atoms linking the nitrogen and oxygen atoms. A search of the Cambridge Structural Database (CSD)[88] was conducted in order to discover whether an analysis of heavy atom positions could give clues to the positions of the hydrogen atoms. The search located 16 organic crystal structures that contain the structural moiety SQH_2, 36 containing SQH^-, and 26 containing SQ^{2-}. The results clearly show that the SQ molecule becomes more delocalised with increasing negative charge (see Table 3.4). Thus in SQ^{2-} the C=O and C=C bonds become more like C···O and C···C, respectively. This indicated that form I had structural features typical of SQH^- and form II seemed to be closer to SQ^{2-} (see Tables 3.3 and 3.4). For form I the C–C bond lengths are 1.42, 1.45, 1.49 and 1.50 Å, and the C–O bond lengths are 1.22, 1.23, 1.27 and 1.31 Å. For form II the symmetrically inequivalent C–C bond lengths are 1.44, 1.45, and 1.47 Å, and the C–O bond lengths are 1.23 and 1.27 Å.

Table 3.4. Average bond lengths (Å) for squaric acid, hydrogen squarate, and squarate di-anion obtained from the CSD.[88]

Distances	SQH_2	SQH^-	SQ^{2-}
C_3=C_4	1.412(18)	1.429(18)	1.463(11)
C_4–C_7 / C_3–C_9	1.459(14) / 1.457(13)	1.431(15) / 1.492(29)	1.460(13) / 1.459(10)
C_7–C_9	1.494(9)	1.487(16)	1.461(10)
O_2–C_3 / C_4–O_5	1.282(24) / 1.288(11)	1.248(14) / 1.306(10)	1.252(9) / 1.254(12)
C_7=O_8 / C_9=O_{10}	1.244(41) / 1.229(7)	1.246(17) / 1.225(10)	1.255(9) / 1.254(12)

Selected parameters associated with the BIPY molecule were also extracted from the CSD; namely the C–N and N–H bonds, and the C–C bond between the pyridine rings (see Table 3.5.), for both co-planar (0 ± 8°) and twisted (23 ± 8°) conformations. The search located 60 organic crystal structures that contain the neutral BIPY structural moiety in the twisted conformation and 76 structures in the co-planar conformation. The $BIPYH^+$ group appeared in 13 structures in the twisted conformation, and in 10 structures in the co-planar conformation. The $BIPYH_2^{2+}$ group appeared in 16 structures in the twisted conformation and in 21 structures in the co-planar conformation. The distributions of the parameters appear to be identical

within the error limits quoted. This is not surprising given the low energy barrier required to convert between the two conformations (less than 10 kJ mol^{-1}).[89]

Table 3.5. Average bond lengths (Å) of BIPY, $BIPYH^+$, and $BIPYH_2^{2+}$ forms as obtained from the CSD[88].

Distances		BIPY	$BIPYH^+$	$BIPYH_2^{2+}$
C–N [a]	Twisted	1.333(28)	1.334(8) / 1.335(10)	1.338(22)
	Co-planar	1.328(12)	1.335(6) / 1.339(6)	1.329(9)
C_{104}–C_{107}	Twisted	1.485(21)	1.485(12)	1.494(22)
	Co-planar	1.485(28)	1.498(14)	1.488(6)

a – Note that in the case of $BIPYH^+$ the first value refers to C–NH bonds and the second to C–N bonds (*i.e.* with no H atom connected to the nitrogen).

3.4.3. Powder neutron diffraction studies

X-ray measurements allowed the heavy atom positions to be located. Location of the H-atoms was very desirable in order to understand fully the origins of the observed phase transition. A critical aspect of this work therefore relied upon the successful collection and interpretation of neutron diffraction data. Ideally, one would have used single-crystal neutron diffraction in order to obtain structural information for form II. However, such studies require relatively large single crystals and despite numerous attempts, it became clear that SQBP intrinsically grows as long, but very thin plates that were not suitable for single crystal neutron diffraction. Instead, it was decided to use powder neutron diffraction.

Initial studies focussed on fully deuterated SQBP (SQBP-d_{10}) using the High Resolution Powder Diffractometer (HRPD) at the Rutherford Appleton Laboratory. For most powder neutron diffraction studies it is essential to use samples that contain small quantities of hydrogen. This is because hydrogen scatters very strongly and incoherently, thereby giving rise to large backgrounds that can overwhelm the Bragg scattering from the sample. After loading a sample of SQBP-d_{10} into a standard vanadium can, a data-set was collected over a period of 18 hours at 292 K. This confirmed the presence of form I. The sample temperature was then progressively raised until 488 K, the diffraction pattern changed significantly and could be successfully indexed as form II. This in itself was an important result because it

demonstrated that the phase transition occurred in the fully deuterated compound, even though Reetz *et al.* had noted that the phase transition did not occur in the partially deuterated compound. After data collection for 12 hours at this elevated temperature, it became apparent that new Bragg peaks attributable to neither form I nor form II had appeared and that these persisted on cooling the sample back to ambient temperature. This strongly suggested decomposition of the sample at such high temperatures, perhaps exacerbated by contact with the vanadium can. For this reason it was not possible to extract structural information from the experiment. It was therefore clear that a powder diffraction experiment on form II would require rapid data collection. For this reason, an experiment was attempted on D20 at the ILL.[39] The very high flux allowed data collection within 20 and 60 minutes for forms I and II, respectively. Furthermore the very high flux allowed the use of a non-deuterated sample.

Since the amount of data obtainable from a powder diffraction study is considerably lower than that from a single crystal study, it was necessary to apply geometrical restraints (bond lengths, angles and planarity) and thermal parameter constraints in order to obtain chemically plausible structures. These restraints were taken from the X-ray data, where at HT the eluding hydrogen atoms were placed on the BIPY molecule. For completeness, Rietveld analyses of both forms are reported (see Figures 3.16 and 3.17). The results confirmed experimentally for the first time that the form II structure is best described as hydrogen-bonded $BIPYH_2^{2+}$ and SQ^{2-} ions.

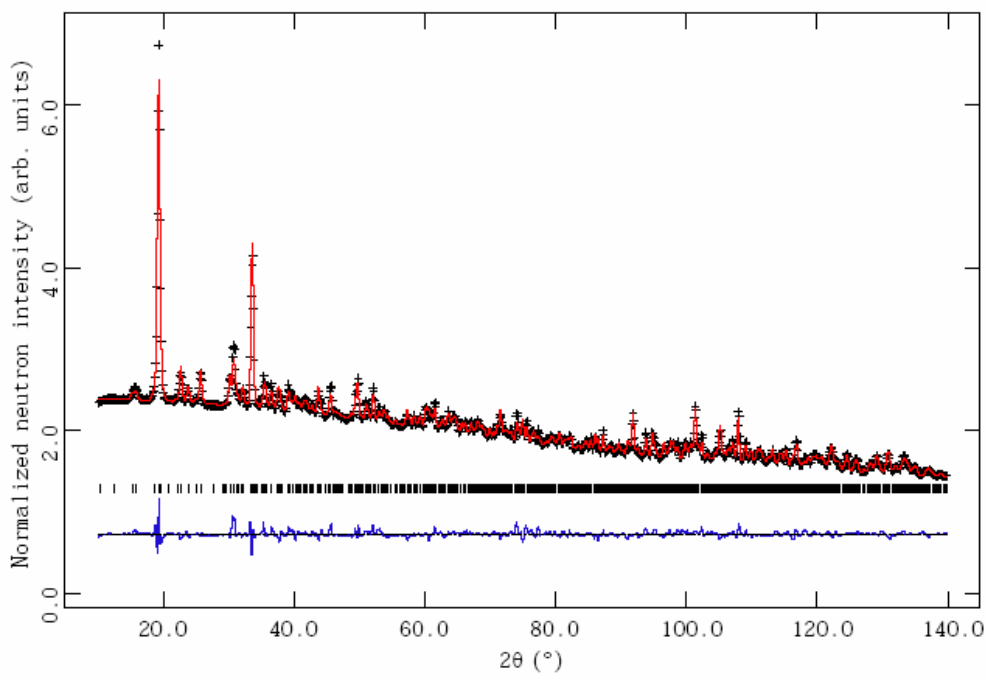

Figure 3.16. Rietveld refinement of the neutron diffraction pattern of form I SQBP at 120 K.[42] The crosses denote the observed data; the solid line is the profile calculated using the 180 K single-crystal X-ray structure of form I as the starting model with coordinates refined under geometrical restraints. The blue line below the pattern shows the difference between the measured and the calculated patterns. The ticks indicate the positions of the Bragg peaks.

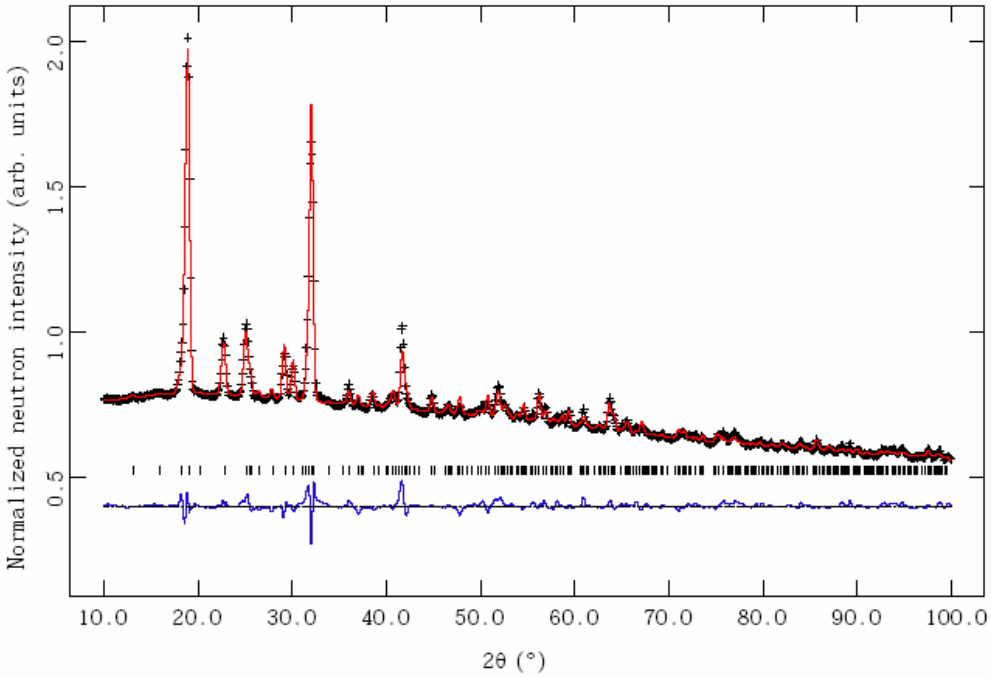

Figure 3.17. Rietveld refinement of the neutron diffraction pattern of form II SQBP at 473 K.[42] The crosses denote the observed data; the solid line is the profile calculated using the 453 K single-crystal X-ray structure of form II as the starting model with coordinates refined under geometrical restraints. The blue line below the pattern shows the difference between the measured and the calculated patterns. The ticks indicate the positions of the Bragg peaks.

3.4.4. Powder X-ray diffraction studies

In order to study the reversibility of the phase transition, powder X-ray studies were performed as a function of temperature. These were carried out using the high-resolution powder-diffraction beamline (ID31) at the European Synchrotron Radiation Facility (ESRF).[49] The diffraction pattern collected at 293 K (see Figure 3.18), could be indexed to form I. Pawley refinement gave a good fit to the data, with the refined lattice parameters being presented in Table 3.6. This demonstrated that the single crystal measurement was representative of the bulk polycrystalline material. However, it should be noted that three weak reflections in the powder pattern (at $2\theta = 6.84$, 8.54 and 8.91°) were not accounted for in the Pawley refinement demonstrating that the sample contained tiny amounts of unidentified impurity.

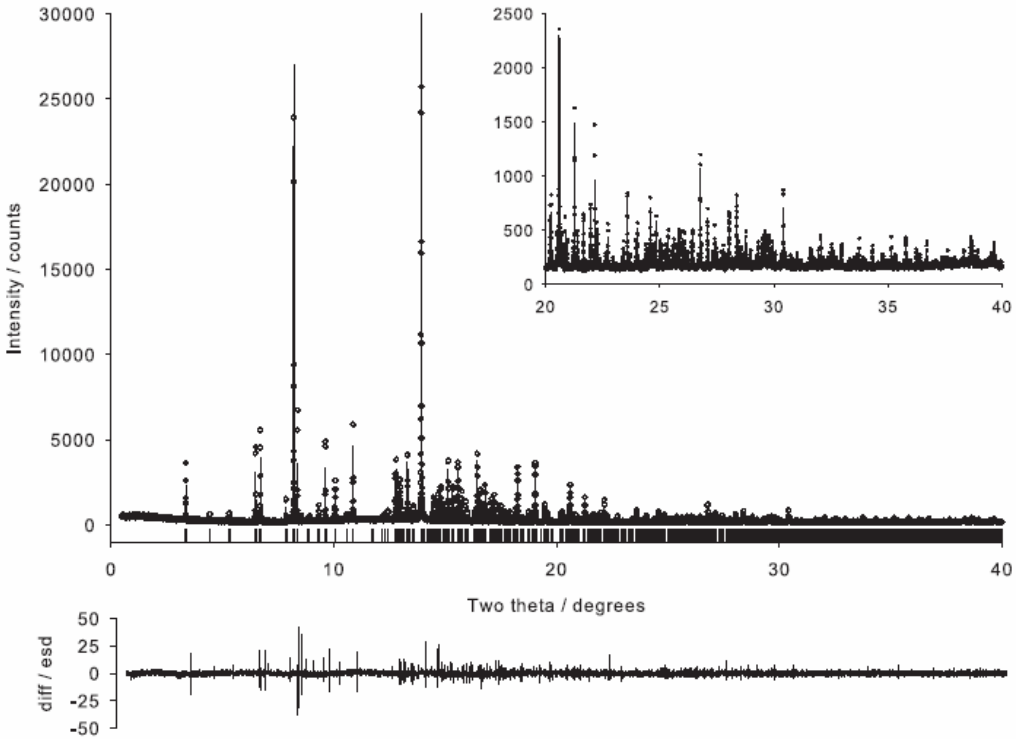

Figure 3.18. Pawley refinement of the synchrotron radiation diffraction pattern of form I SQBP at 293 K.[90, 91] The circles denote the observed data; the line is the calculated profile. The line below the pattern shows the difference between the measured and the calculated patterns, expressed as difference divided by the ESD. The ticks indicate the positions of the Bragg peaks.

A powder pattern was collected at 493 K (see Figure 3.19) and a very satisfactory fit to the data was obtained using the lattice parameters and space group of form II, derived from the single-crystal X-ray study, as a starting point (see Table 3.6). Very small amounts of another component were observed, but its identity is unknown and the very few number of observable peaks thwarted any attempt to index this component.

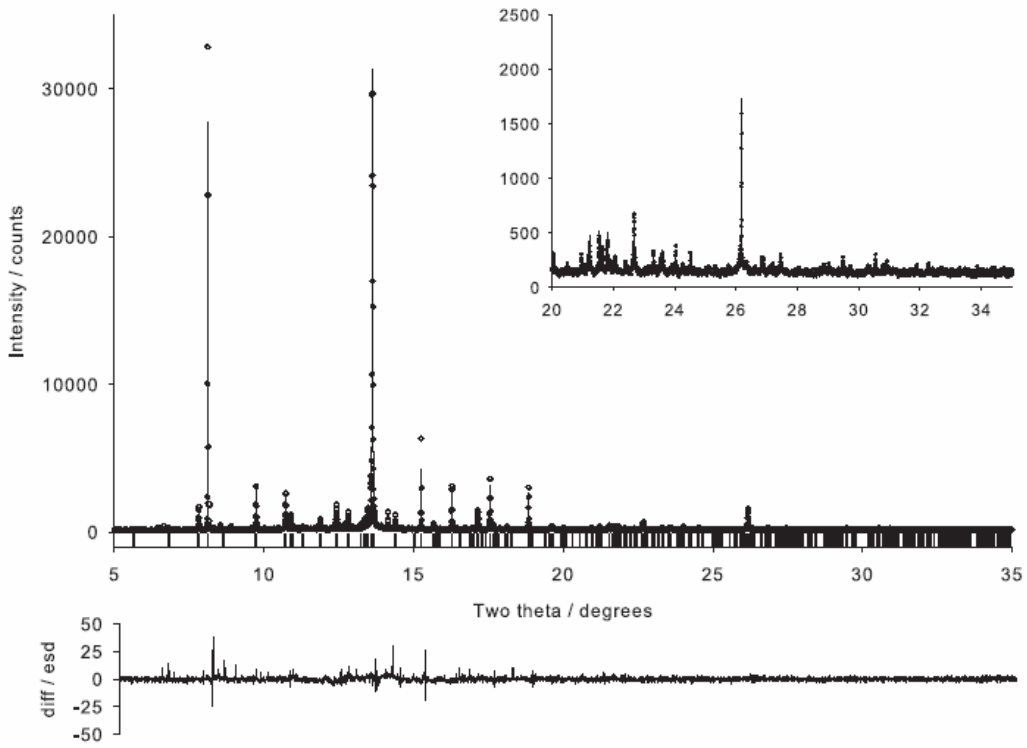

Figure 3.19. Pawley refinement of the synchrotron radiation diffraction pattern of form II SQBP at 493 K.[90, 91] The circles denote the observed data; the line is the calculated profile. The line below the pattern shows the difference between the measured and the calculated patterns, expressed as difference divided by the ESD. The ticks indicate the positions of the Bragg peaks.

The sample was subsequently cooled over a period of *ca.* 10 hours where five data-sets were collected (420, 370, 320, 270 and 220 K). The diffraction pattern collected at 420 K (see Figure 3.20) could be satisfactorily fitted to a mixture of forms I and II with the refined lattice parameters presented in Table 3.6. This confirmed that form II was reverting to form I, not a new form IV as postulated by Reetz *et al*.

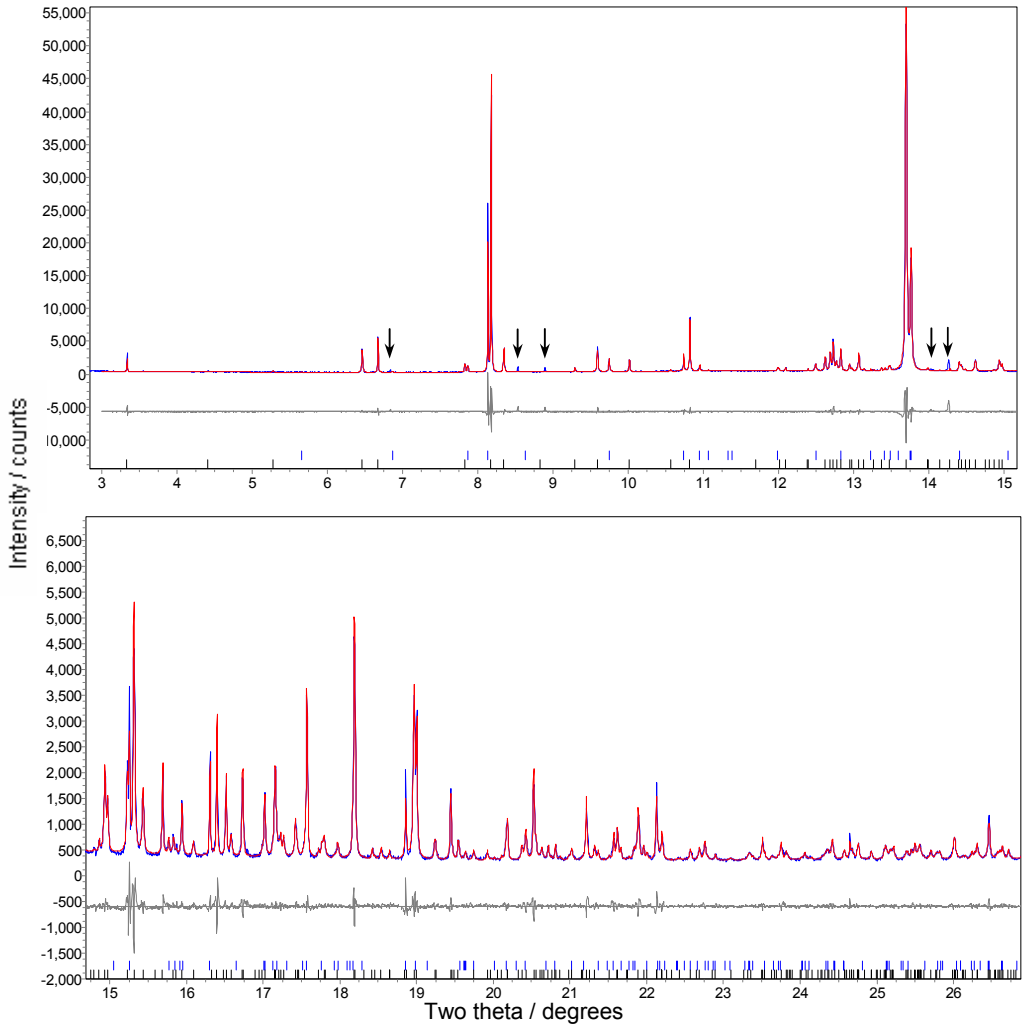

Figure 3.20. Two-phase Pawley refinement of the synchrotron radiation diffraction pattern of SQBP at 420 K.[90, 91] The blue line denotes the observed data; the red line is the calculated profile. The grey line below the pattern shows the difference between the measured and the calculated patterns, expressed as difference divided by the ESD. The black and blue ticks indicate the positions of the Bragg peaks of form I and form II respectively. Note that the impurity peaks are identified by arrows.

The diffraction patterns obtained during the remaining data-collections of the cooling process gave good fits, consistent with the predominance of a single phase, namely form I (see Table 3.6). This indicates that there is a kinetic barrier to overcome along the transition between form II and I on cooling, after which the transition is fully reversible.

Table 3.6. Unit cell parameters of SQBP determined from variable temperature powder diffraction experiments. Note that the volume expansion of form I is essentially linear, with $r^2 = 0.9991$.

T / K	Lattice parameters				Volume / Å^3	R_{wp}^{Pawley}	χ^2
	a / Å	*b* / Å	*c* / Å	β / °			
270	3.7900(1)	11.2073(1)	27.4336(1)	92.386(1)	1164.25(3)	18.36	5.52
293	3.7997(1)	11.2098(1)	27.4523(1)	92.223(1)	1168.42(3)	10.43	4.33
320	3.8097(1)	11.2133(1)	27.4704(1)	92.080(1)	1172.74(3)	17.85	5.13
370	3.8325(1)	11.2236(1)	27.5108(1)	91.749(1)	1182.82(3)	17.70	6.81
420	3.8539(1)	11.2347(1)	27.5398(2)	91.479(1)	1192.00(3)	8.19	7.66
	12.3463(3)	11.2960(1)	9.0503(1)	108.919(1)	1194.00(3)		
493	12.4624(3)	11.3141(1)	9.0940(1)	109.459(1)	1209.02(3)	13.84	4.67

3.4.5. Computational modelling – structure

3.4.5.1. Geometry optimisation

The results obtained by PW-DFT calculations for the geometry optimisation of certain structure parameters of both forms of SQBP can be found in Table 3.3, together with the experimental data for direct comparison. Based on the parameters found in Table 3.3 the simulations were generally in very good agreement with the X-ray data, having maximum deviations of 4.0 and 5.2 %, and averages of 1.1 and 2.3 % for form I and form II, respectively. The agreement with the neutron data was also good, with average deviations of 2.7 and 2.1 %, with maximums of 9.7 and 6.8 % for forms I and II, respectively.

The form II structure optimisation was run in parallel to the neutron experiments and was therefore initiated from the X-ray diffraction heavy atom coordinate set with doubly protonated BIPY molecules. This revealed that this structure was indeed a stable point on the potential energy surface. Form II was calculated to be slightly lower in energy than form I, but the overall difference was very small (6.2 kJ mol^{-1} at 0 K *cf.* 1.5 and 3.8 kJ mol^{-1} from k_BT at 180 and 453 K, respectively) and lay well within the range expected for polymorphs of molecular compounds.[92]

3.4.5.2. Potential energy surfaces

Positioning of the H-atoms, in particular the acidic ones, is central to the present study. In order to investigate whether or not the geometry optimisations had their positions biased by the starting model, PES scans were performed.[54] This was achieved by performing a series of single-point energy calculations where the H-atoms were systematically shifted along the short strong hydrogen bond between the nitrogen and oxygen atoms, thus mimicking the form I to form II transition (dark yellow line in Figure 3.21) and the reverse reaction (red line in Figure 3.21).

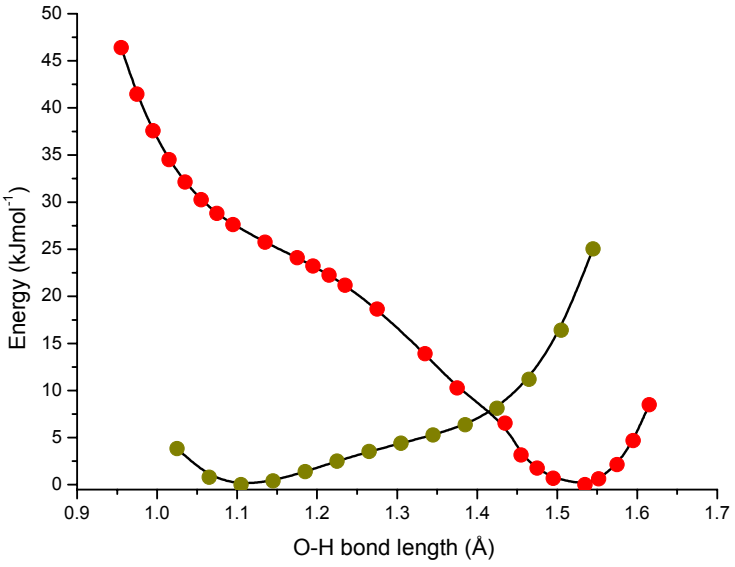

Figure 3.21. Graph of the PES calculated for the acidic H-atom position of both forms I (dark yellow) and II (red).

The PES scans reveal many important properties of the H-bond linkages. First, the minimum energy geometries are clearly observed (yielding O–H distances around 1.1 and 1.5 Å, with the latter corresponding to an N–H bond length of 1.07 Å). For each form only one stable minimum exists, although a shoulder on each surface corresponding to the proton-transferred form is visible. The energy well for

the form I structure is shallower than that of form II, where the H-atoms appear to require less than 10 kJ mol^{-1} for the protons to adopt a conformation similar to that of form II. For form II the barrier to revert to a form I-like structure is much higher (around 30 kJ mol^{-1}). This is indicative that the H-atoms in form I are more labile than in form II, which in turn could be seen to account for the observation from the DSC and powder diffraction reversibility studies that the reversible reaction appeared to be controlled by kinetic factors.

3.4.5.3. Molecular dynamics

In order to go beyond the PES and explore the free-energy surface molecular dynamics simulations for both forms were performed.[54] These demonstrated that the equilibrium structures were not perturbed when energy (*i.e.* temperature) was given to the system, thereby confirming the stability of the proposed HT structure. Furthermore, the time-averaged model for form II obtained from the MD (which was run in the absence of symmetry constraints, *i.e.* space group *P*1) was concurrent with the *C*2/*c* space group setting obtained from the X-ray diffraction experiments.

To further probe the suggestion raised by the PES scans that the H-atoms in form I were more labile than form II, the time-averaged O–H and N–H bond lengths were extracted from the MD simulations. After discarding the first 0.15 ps to allow for system equilibration, the O–H trajectories from the form I model and the N–H from form II were averaged in accordance with the blocking method.[93] This corrected the standard deviations obtained for correlation within the data set. The final uncertainties quoted are the errors obtained in the standard deviations (that is the standard deviation divided by the square-root of the number of data points). After this process, the time-averaged O–H distance from form I equated to 1.270(30) Å, compared to 1.113(2) Å for the N–H distance from form II. The elongated value and significant uncertainty in the former indicated that the free-energy surface also supports a more labile H-atom in the form I structure.

3.4.6. Computational modelling – properties

3.4.6.1. Relative energies

The relative energies of forms I and II ($SQH^-.BIPYH^+$ and $SQ^{2-}.BIPYH_2^{2+}$, respectively) obtained from the solid state optimisations are presented in Table 3.7.[72] Like the PW-DFT calculations (section 3.4.5), the high temperature form is favoured, but the energy difference is again quite small.

Table 3.7. The internal energy difference, ΔE^{per} [E(form II)–E(form I)] (kJ mol^{-1}) separating the optimised lattices of SQBP as a function of basis set size and Monkhorst-Pack mesh density. Also presented are similar values obtained from isolated molecule calculations, both with-, $\Delta E^{iso,ZPE}$, and without-, ΔE^{iso}, the vibrational zero point correction.[72]

Basis set	MP Mesh	ΔE^{per}	ΔE^{iso}	$\Delta E^{iso,ZPE}$
6–31G*	4×4×4	-2.21	—	—
6–311G**	4×4×4	-4.46	—	—
6–311G**	6×6×6	-4.42	—	—
6–311++G*	—	—	+1093.95	+1098.49

The isolated molecule calculations offered useful insights, revealing in particular that the reaction in which the remaining proton transfers from the SQH^- anion to the $BIPYH^+$ cation was very strongly disfavoured. The fact that this process occurs at all within the solid state is a direct consequence of the increase in electrostatic stabilisation arising from the change in the charge states of the molecular ions and their arrangement inside the lattice. A semi-quantitative treatment of these interactions can be obtained from the application of a model for a one-dimensional chain of ions of alternating sign.[72] The energy per pair is given by $E = \frac{-2\ln(2)q^2}{4\pi\varepsilon_0 R}$, where the factor $2\ln(2)$ is the Madelung constant for a 1D chain, q is the magnitude of the charges borne by the ions, ε_0 is the vacuum permittivity and R is the separation of the ions. Figure 3.22 shows the energy difference obtained between the two charged states of the chains, $\Delta E = E(q_2)–E(q_1)$ for the 'ideal' case

($q_1 = \pm 1e$, $q_2 = \pm 2e$), as well as with the effective Mulliken charges of the molecules shown in Table 3.8 ($q_1 = \pm 0.715e$, $q_2 = \pm 1.297e$). It should be noted however, that the latter values must be regarded as establishing only relative variations, since absolute values have little formal meaning and are strongly dependent on which basis set is used.[94]

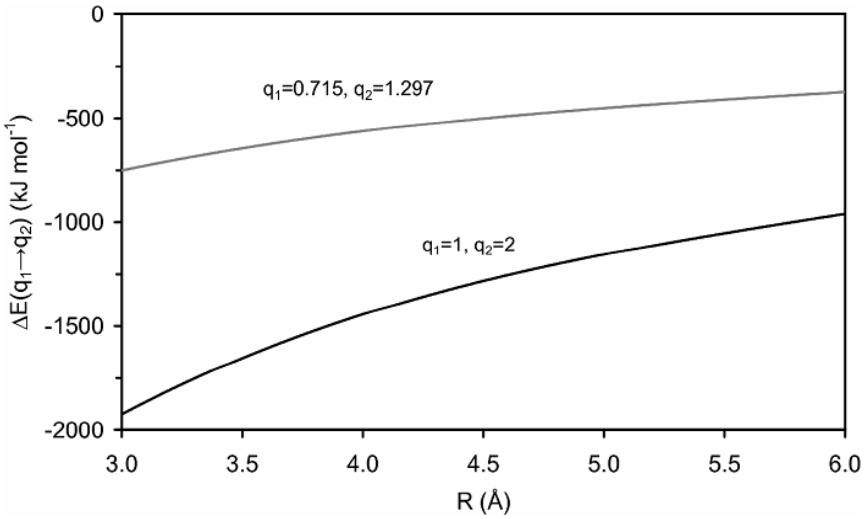

Figure 3.22. The difference in electrostatic energies per ion pair, ΔE (kJ mol^{-1}), between one-dimensional ionic chains with alternating charges of $\pm q_1$ and $\pm q_2$ as a function of ionic separation, R(Å).[72]

The electrostatic stabilisation produced by use of the ideal charges more than offsets the large energy difference obtained from the isolated molecule calculation for separations of less than approximately 5.5 Å. However, the stabilisations produced by substitution of the calculated charges are much smaller, and do not suffice to stabilise the proton transfer state in the isolated molecules at any reasonable separation. This is likely due to an underestimate of the effective charges within the Mulliken analyses, in which the net charge transfer between molecules in forms I and II amounts to only 0.582*e*.

Table 3.8. The effective Mulliken charges, q (*e*), borne by BIPY and SQ molecules, the energies of the lower and upper edges (eV) and assignments of the topmost valence and lowest conduction bands, and the corresponding T_1, T_2 and T_3 absorption wavelengths (as defined in Figure 3.25) and band widths (T_1–T_3) (nm) in forms I and II of the SQBP crystal.[72]

Form	q(BIPY)	q(SQ)	Band	E_{lower}	E_{upper}	Assignment	T_1	T_2	T_3	Width
LT	+0.715	-0.715	Valence	-5.589	-5.381	SQ C + O	427	403	382	47
			Conduction	-2.477	-2.344	BIPY C + N				
HT	+1.297	-1.297	Valence	-5.050	-4.880	SQ C + O	621	566	520	101
			Conduction	-2.884	-2.666	BIPY C + N				

A more accurate treatment of the electrostatic interactions can be obtained by performing an Ewald sum over the Mulliken charges of individual atoms, yielding an energy difference between the two forms of 414.92 kJ mol^{-1}, which is within the range of stabilisations produced by the 1D chain model using the same charges and presumably represents an underestimate for essentially the same reasons. The charges obtained from the application of a basis-independent method, such as a topological analysis, or a calculation of the dynamical charge tensors, would be expected to offer useful comparisons.[72] Nevertheless, the current results indicate that the small energy difference obtained between the polymorphic forms in the solid state arises from the counterbalancing of two much larger contributions, and establish the magnitudes of the interactions involved. Finally, it should be noted that the addition of the vibrational zero point energies to the internal energies of the isolated molecules, destabilises the HT structure by 4.53 kJ mol^{-1} relative to form I. While this value has been obtained within a strictly harmonic analysis, and does not include the red-shifts of the donor-proton stretching modes in the hydrogen bonds of the solids, it does support the suggestion that the relative free energies of the two forms may vary substantially from their internal energies. Furthermore, it is conceivable that the inclusion of vibrational contributions may invert the order of stability of the forms, so that form I is, as expected, more stable than form II. The conclusion is that future theoretical studies of both the current system, and polymorphic molecular crystals in general should include an explicit treatment of the thermodynamics obtained from the direct integration of the phonon dispersion relations across the Brillouin zone.

3.4.6.2. Electronic structure and absorption spectra

The atom-projected densities-of-states plots for forms I and II are presented in Figures 3.23 and 3.24 respectively. Examination clearly shows that both structures are wide gap charge-transfer insulators, in which the fundamental excitation of the solid corresponds to the transfer of an electron from the SQ(C+O) π-states to the BIPY(C+N) π^*-states.[72]

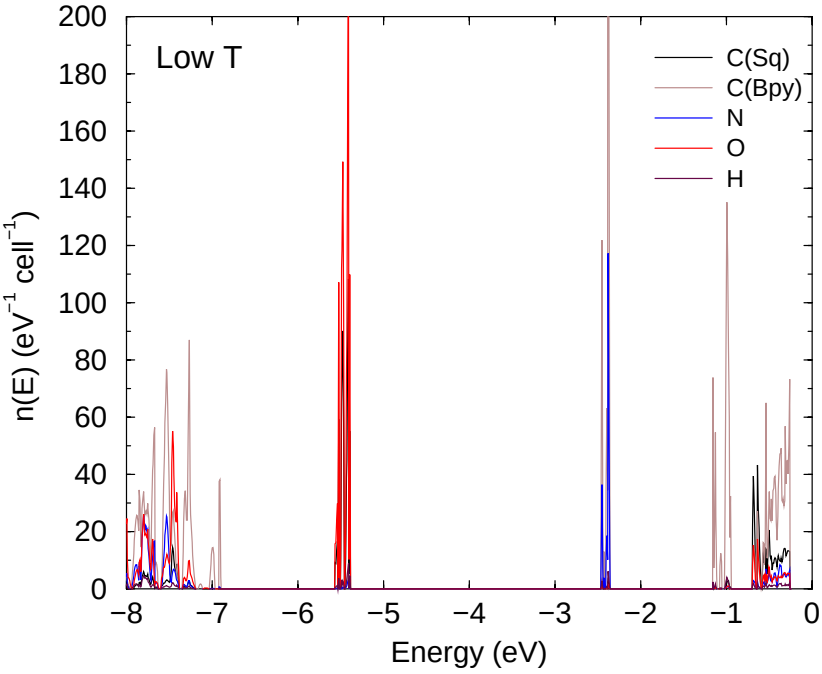

Figure 3.23. The atom projected densities-of-states plot for form I. The valence band edge lies at -5.38 eV.[72]

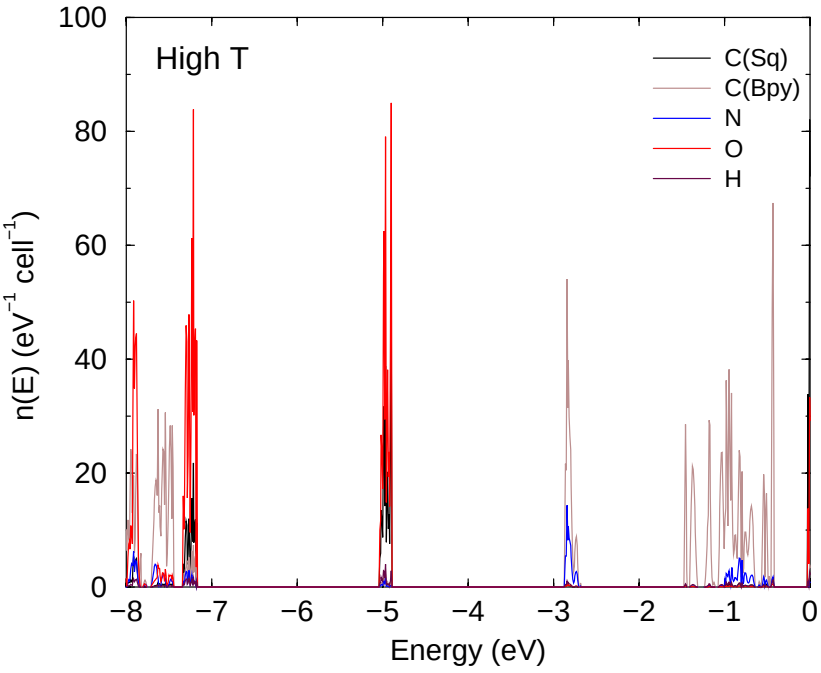

Figure 3.24. The atom projected densities-of-states plot for form II. The valence band edge lies at -4.88 eV.[72]

Adopting the simple triangular model of the topmost valence and lowermost conduction bands depicted in Figure 3.25 allowed to make some comparisons with the experimental optical absorption spectra shown in Figure 3.7. Viewed purely in terms of the joint densities-of-states, and omitting any consideration of the matrix elements of the transitions, it can be seen that the T_2 transition is likely to occur with greater weight than the T_1 and T_3 excitations.[72] Equating the T_2 transition with the peak optical absorption yields theoretical values of 403 and 566 nm in forms I and II respectively, in reasonable agreement with experimental values of 450 and 540 nm. Moreover, the trends in the theoretical absorption band widths, derived as T_1–T_3 would also appear to be in agreement with the experimental observations (full width at half maximum of around 50 and 70 nm for forms I and II).

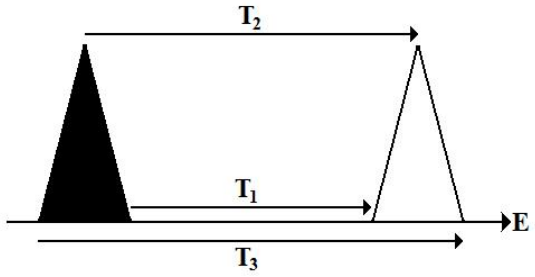

Figure 3.25. The triangular model for the uppermost valence- and lowermost conduction band densities-of-states, with the limiting, T1 and T3, and strong, T2, transitions indicated.[72]

The increase in the band width in form II would seem to be almost entirely due to the corresponding increase in the BIPY-derived conduction band width. This suggests that this in turn arises from the fact that the BIPY molecules are planar in this structure, leading to an enhanced overlap of the π^* states resident on both rings. Finally, there remains the question of why the temperature-induced proton transfer leads to a change of colour in this material. It is clear from a comparison of Figure 3.23 and 3.24 that this is due to the increase- and decrease- respectively in the energies of the uppermost valence- and lowermost conduction bands in form II. Two opposing interactions underlie these shifts: first, there is the Madelung potential

derived from the extended environment, the change in which with progress from form I to form II would be expected to stabilise the SQ-derived valence band and destabilise the BIPY-derived conduction band. Secondly, there is the intramolecular potential, the change in which would be expected to yield opposite shifts to those just discussed. Thus, the change in the position of the bands observed in our calculations would suggest that the intramolecular interactions dominate over the Madelung contributions.

3.5. Variable pressure studies – results and discussion

Initial studies were performed on single-crystals at Station 9.8 at the STFC Daresbury Laboratory. After loading a crystal of form I in a diamond-anvil cell the pressure was raised in steps. It was found that in the range 0–14 kbar SQBP form I did not undergo any transition. Instead the lattice parameters decreased (see Table 3.9), such that at 14 kbar the volume of the unit cell reduced by approximately 12 % compared with that at ambient pressure. As pressure was increased above 14 kbar a striking colour change, similar to that seen in the VT studies, was observed (see Figure 3.26). The transition was, however, destructive as fracturing of the crystal was clearly visible. This caused the appearance of multiple domains in the diffraction patterns, and it proved impossible to index the reflections. Nevertheless, on the basis of the colour change and the results obtained from the variable temperature studies proton transfer should also be induced by pressure.

Table 3.9. Unit cell parameters of SQBP determined from single-crystal X-ray diffraction experiments with increasing pressure.

Pressure / kbar	Lattice parameters				Volume / Å^3
	a / Å	*b* / Å	*c* / Å	β / °	
0	3.810(5)	11.27(2)	27.89(2)	92.12(3)	1197(7)
3	3.812(3)	11.26(1)	27.50(20)	92.29(2)	1182(2)
14	3.592(6)	10.99(5)	26.80(50)	91.90(30)	1058(5)

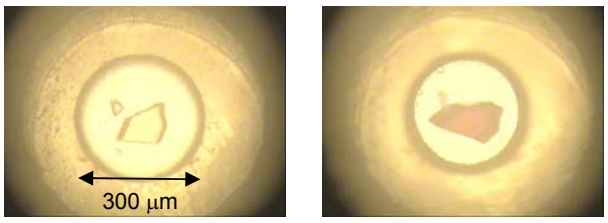

(a) (b)

Figure 3.26. Optical image of a single crystal of form I SQBP inside a DAC with 4:1 methanol-ethanol and a ruby chip at: (a) ambient pressure; (b) over 14 kbar.

In an effort to overcome the deterioration in crystal quality, high-pressure powder diffraction methods were selected to study this system. These experiments took place using both X-ray (Station 9.5 HPT at the STFC Daresbury Laboratory) and neutron (PEARL beamline at ISIS) sources. Both studies of the pressure-driven phase change gave similar results, but the discussion will be limited to the neutron diffraction studies as they are of higher quality. In the range 0–14 kbar, the *a*-, *b*- and *c*- axes decreased by 4.9, 1.6 and 2.0 %, respectively while the β angle increased by 3.9 % (see Figure 3.27 and Table 3.10). This resulted in an 8.8 % decrease in volume over this pressure range. The higher compressibility along the *a*- axis can be understood by reference to the crystal structure. Compression of the structure causes reduction in the distance between layers of molecules and this has a significant component along the *a*- axis (see Figure 3.12).

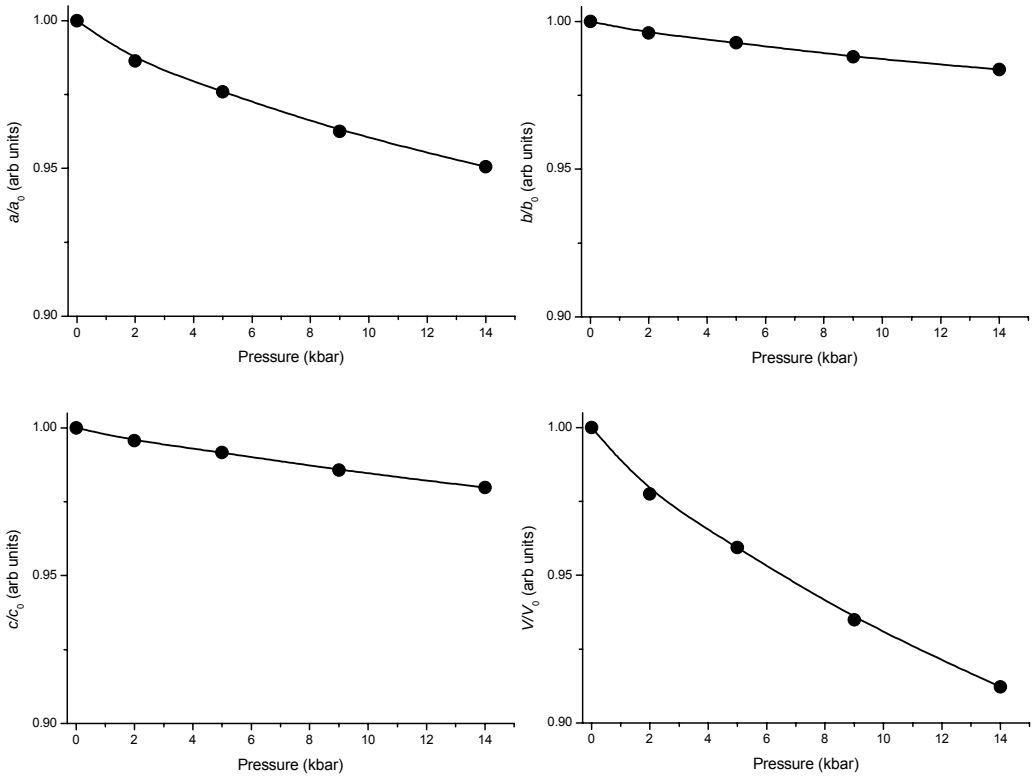

Figure 3.27. Variation of unit-cell parameters determined from powder diffraction experiments as a function of pressure.

Table 3.10. Unit cell parameters of SQBP determined from powder neutron diffraction experiments with increasing pressure.

Pressure / kbar	Lattice parameters				Volume / Å^3
	a **/ Å**	***b*** **/ Å**	***c*** **/ Å**	**β / °**	
0	3.7920(6)	11.1687(29)	27.5522(58)	92.083(17)	1166.12(32)
2	3.7401(6)	11.1252(28)	27.4317(68)	92.939(19)	1139.91(34)
5	3.7007(5)	11.0873(24)	27.3214(53)	93.650(16)	1118.74(26)
9	3.6500(6)	11.0343(25)	27.1596(55)	94.697(17)	1090.17(26)
14	3.6043(4)	10.9864(16)	26.9971(37)	95.712(11)	1063.73(17)

The pattern obtained at 18 kbar showed the appearance of new peaks indicative of a phase transition (see circled area and the high intensity peak around 3.25 Å in Figure 3.28). This phase was also present at 23 kbar, but at 26 kbar the pattern changed again to give what appeared to be another phase. This persisted up to 31 kbar, which was the limit of the study. On decompression, the new phase remained down to 14 kbar and form I appeared again after full recovery to ambient conditions.

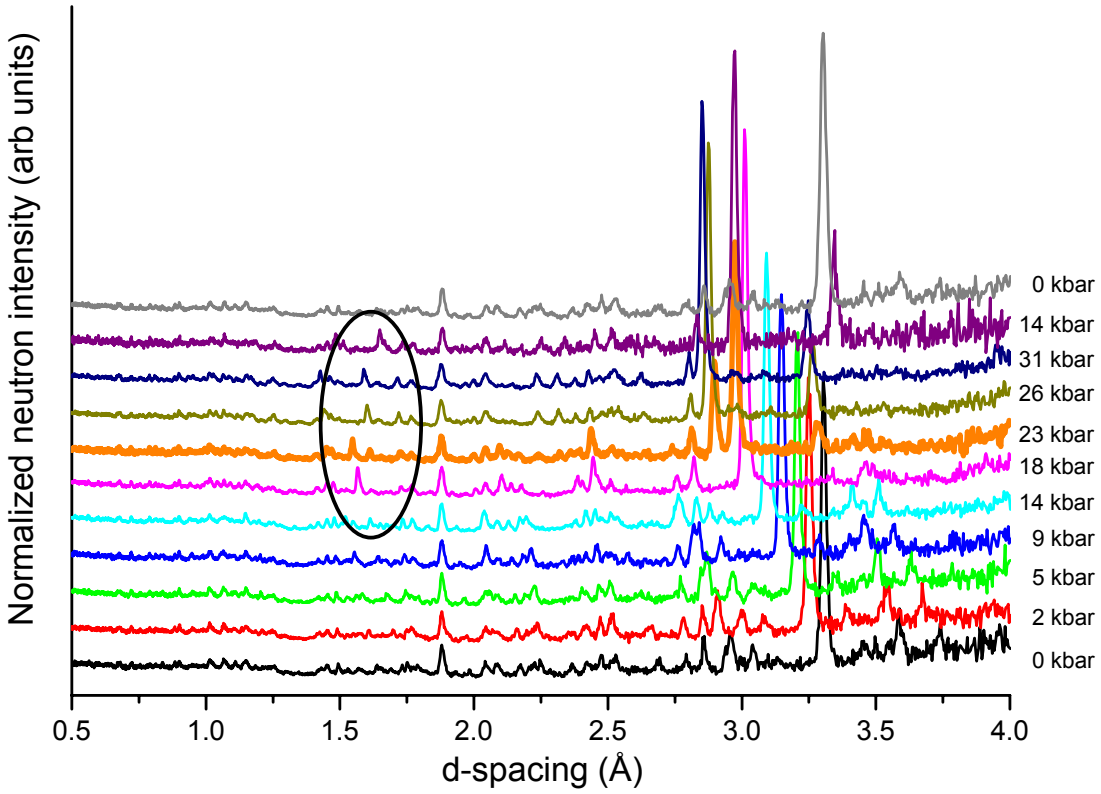

Figure 3.28. Variable pressure compression study and recovery of SQBP-d_{10}. The thicker orange line represents the mixed form.

A direct comparison of the diffraction patterns obtained at ambient pressure together with high-pressure patterns is displayed in Figure 3.29. Comparison suggests that neither of the high-pressure phases correspond to form II, thereby casting doubt on Reetz's[9] suggestion that high-temperature and high-pressure forms are the same. Nevertheless, it is very likely that all of the forms are related and may show structural similarities.

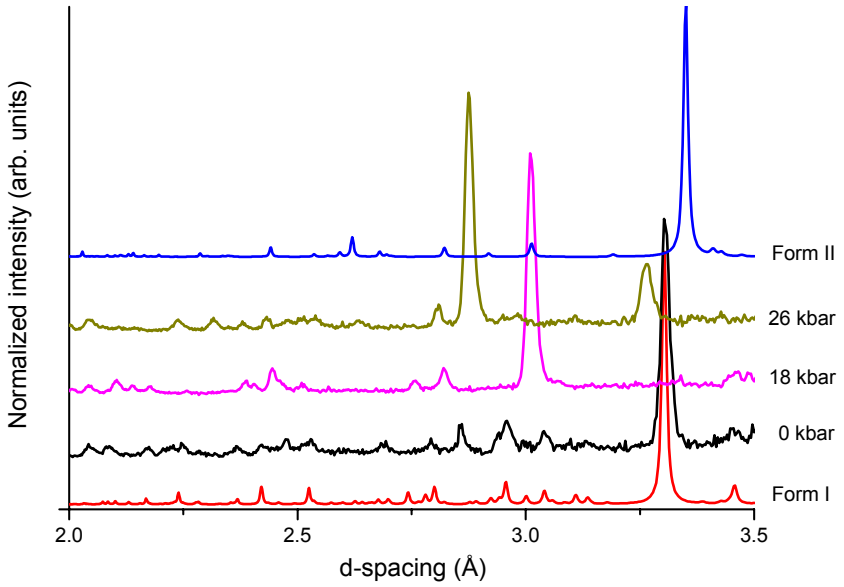

Figure 3.29. Comparison of the VT and VP powder patterns. It should be noted that because the Form I (298 K) and II (453 K) patterns were calculated based on X-ray scattering factors the intensities are not comparable with from those obtained from neutron. However, the peak positions are equivalent as they are dependent solely on unit-cell dimensions. Note also that the neutron diffraction patterns also contain peaks due to the pressure calibrant Pb.

All attempts to index the powder patterns for the two HP forms (above 14 kbar) have proven to be unsuccessful. This is not surprising given the size of the unit cell, moderately low symmetry and limited *d*-spacing range. Nevertheless, as stated previously, there is the suggestion that proton transfer might occur on the basis of the colour change. It is therefore clear that the study of the SQBP system is incomplete and further work will be required before a full understanding of the behaviour of this pressure-induced proton transfer system is obtained.

3.6. Conclusions

In situ heating of the SQBP form I to 453 K afforded the heavy atom structure of the high-temperature form II. The single-crystal to single-crystal phase transition occurred due to the fact that the structures of both forms have numerous similarities. Location of the H-atoms along the N···O short H-bond was identified by the use of very high flux powder neutron diffraction. These were determined to be on the BIPY molecules, thereby confirming that proton transfer occurred during the transition.

The reversibility study performed with powder X-ray diffraction demonstrated that on cooling form II below 423 K a mixture of both forms I and II was initially obtained. However, after allowing the sample to equilibrate, it was found that the transition was fully reversible, suggesting that a kinetic barrier had to be overcome, which remains consistent with the DSC study of the transformation.

The *ab initio* calculations were in agreement with the experimental results. The structure of form II was calculated to exhibit an arrangement of molecules that stabilises the electrostatic interactions of the charged states of the molecular ions (SQ^{2-} and $BIPYH_2^{2+}$) consequent of the proton transfer event. Visible absorption spectra were calculated and revealed good agreement with those determined experimentally. The colour change is suggested to be a consequence of the destabilisation of the SQ molecules (leading to the higher energy of the valence bands) and a stabilisation of the BIPY molecules (leading to the lower energy of the conduction bands).

High-pressure experiments showed that a colour change from yellow to red also occurred on increasing the pressure applied to a single crystal. This was associated with a transition which destroyed the single crystal. Powder neutron diffraction experiments indicated that the sample underwent two phase transitions at 18 kbar and at 26 kbar, but reverted back to form I on decompression to ambient conditions (*i.e.* the transitions are completely reversible). The patterns obtained for these two high-pressure forms were clearly different from those of forms I and II, but

could not be indexed. Based on the colour change and the results obtained from the variable temperature studies proton transfer is likely to occur.

In conclusion the current chapter has explored the behaviour of the titled adduct under a range of conditions using experimental and computational methods. The studies proved to be challenging and the level of complexity of this system is close to the limits of experimental and computational methodologies.

3.7. Bibliography

[1] T. Steiner, *Angew. Chem. Int. Ed.* **2002**, *41*, 48.

[2] G. Zundel, *Adv. Chem. Phys.* **2000**, *111*, 1.

[3] N. S. Golubev, G. S. Denisov, V. A. Gindin, S. S. Ligay, H.-H. Limbach, S. N. Smirnov, *J. Mol. Struct.* **1994**, *322*, 83.

[4] J. A. Cowan, J. A. K. Howard, G. J. McIntyre, S. M.-F. Lo, I. D. Williams, *Acta Cryst. B* **2003**, *59*, 794.

[5] J. A. Cowan, J. A. K. Howard, G. J. McIntyre, S. M.-F. Lo, I. D. Williams, *Acta Cryst. B* **2005**, *61*, 724.

[6] F. Fontaine-Vive, M. R. Johnson, G. J. Kearley, J. A. K. Howard, S. F. Parker, *J. Am. Chem. Soc.* **2006**, *128*, 2963.

[7] C. A. Morrison, M. M. Siddick, P. J. Camp, C. C. Wilson, *J. Am. Chem. Soc.* **2005**, *127*, 4042.

[8] B. H. Peng, G. F. Liu, L. Liu, D. Z. Jia, *Tetrahedron* **2005**, *61*, 5926.

[9] M. T. Reetz, S. Hoger, K. Harms, *Angew. Chem. Int. Ed. Engl.* **1994**, *33*, 181.

[10] T. Steiner, I. Majerz, C. C. Wilson, *Angew. Chem. Int. Ed.* **2001**, *40*, 2651.

[11] C. C. Wilson, *Acta Cryst. B* **2001**, *57*, 435.

[12] C. C. Wilson, C. A. Morrison, *Chem. Phys. Lett.* **2002**, *362*, 85.

[13] C. C. Wilson, K. Shankland, N. Shankland, *Z. Kristallogr.* **2001**, *216*, 303.

[14] D. T. Ireland, H. F. Walton, *J. Phys. Chem.* **1967**, *71*, 751.

[15] D. J. MacDonald, *J. Org. Chem.* **1968**, *33*, 4559.

[16] D. Semmingsen, *Acta. Chem. Scand.* **1973**, *27*, 3961.

[17] D. Semmingsen, F. J. Hollander, T. F. Koezle, *J. Chem. Phys.* **1977**, *66*, 4405.

[18] T. Kolev, Z. Glavcheva, R. Petrova, O. Angelova, *Acta Cryst. C* **2000**, *C56*, 110.

[19] R. J. Bull, M. F. C. Ladd, D. C. Povey, R. Shirley, *Cryst. Struct. Commun.* **1973**, *2*, 625.

[20] E. J. MacLean, P. S. Wheatley, G. Ferguson, C. Glidewell, *Acta Cryst. C* **1999**, *55*, 1892.

[21] I. L. Karle, D. Ranganathan, V. Haridas, *J. Am. Chem. Soc.* **1996**, *118*, 7128.

[22] S. L. Georgopoulos, R. Diniz, B. L. Rodrigues, M. I. Yoshida, L. F. C. De Oliveira, *J. Mol. Struct.* **2005**, *753*, 147.

[23] V. Bertolasi, P. Gilli, V. Ferretti, G. Gilli, *Acta Cryst. B* **2001**, *57*, 591.

[24] G. Gilli, V. Bertolasi, P. Gilli, V. Ferretti, *Acta Cryst. B* **2001**, *57*, 859.

[25] A. Albert, R. Goldacre, J. Phillips, *J. Chem. Soc.* **1948**, 2240.

[26] L. A. Ashton, J. I. Bullock, P. W. G. Simpson, *J. Chem. Soc., Faraday Trans.* **1982**, *78*, 1961.

[27] J. A. Cowan, J. A. K. Howard, M. A. Leech, *Acta Cryst. C* **2001**, *57*, 302.

[28] H. W. Roesky, M. Andruh, *Coord. Chem. Rev.* **2003**, *236*, 91.

[29] F. H. Herbstein, *Perspectives in Structural Chemistry, Vol. IV*, John Wiley & Sons, Inc., **1971**.

[30] C. D. Sherrill, M. O. Sinnokrot, *J. Phys. Chem. A* **2004**, *108*, 10200.

[31] W. R. Browne, C. M. O'Connor, J. S. Killeen, A. L. Guckian, M. Burke, P. James, M. Burke, J. G. Vos, *Inorg. Chem.* **2002**, *41*, 4245.

[32] PerkinElmer Life and Analytical Sciences, Shelton, Connecticut, USA.

[33] C. Spanswick, School of Chemistry and EaSTCHEM Research School, The University of Edinburgh, UK, Personal communication, **2005**.

[34] SAINT Area-Detector Software Package v7.01A, Bruker - AXS, Madison, Wisconsin, USA, **2003**.

[35] G. M. Sheldrick, SADABS v2.04, University of Gottigen, Germany, **2001**.

[36] A. Altomare, G. Cascarano, C. Giacovazzo, A. Guagliardi, *J. Appl. Cryst.* **1993**, *26*, 343.

[37] D. J. Watkin, C. K. Prout, J. R. Carruthers, P. W. Betteridge, R. I. Cooper, CRYSTALS v12 ed., Chemical Crystallography Laboratory, Oxford, UK, **2003**.

[38] R. M. Ibberson, W. I. F. David, K. S. Knight, *Report RAL-92-031. Ruttherford Appleton Laboratory, Chilton, Didcot, Oxfordshire, UK* **1992**.

[39] C. C. Wilson, Department of Chemistry and WestCHEM Research School, University of Glasgow, UK, Personal communication, **2007**.

[40] T. C. Hansen, P. F. Henry, H. E. Fischer, J. Torregrossa, P. Convert, *Meas. Sci. Technol.* **2008**, *19*, 034001.

[41] E. N. Maslen, in *International Tables for Crystallography, Vol. 6*, **2006**, pp. 600.

[42] W. G. Marshall, K. S. Knight, ISIS Neutron Facility, Rutherford Appleton Laboratory, UK, Personal communication, **2007**.

[43] D. Richard, M. Ferrand, G. J. Kearley, LAMP - Large Array Manipulation Program, ILL.

[44] H. M. Rietveld, *Acta Cryst.* **1967**, *22*, 151.

[45] A. C. Larson, R. B. Von Dreele, *GSAS, Report LAUR86-748, Los Alamos National Laboratory, New Mexico, USA* **2004**.

[46] B. H. Toby, *J. Appl. Cryst.* **2001**, *34*, 210.

[47] A. N. Fitch, *Mater. Sci. Forum* **1996**, *228-231*, 219.

[48] A. N. Fitch, *J. Res. Natl. Inst. Stand. Technol.* **2004**, *109*, 133.

[49] C. R. Pulham, School of Chemistry and EaSTCHEM Research School, The University of Edinburgh, UK, Personal communication, **2006**.

[50] G. S. Pawley, *J. Appl. Cryst.* **1981**, *14*, 357.

[51] A. A. Coelho, Bruker AXS, Karlsruhe, Germany, **2003**.

[52] W. I. F. David, K. Shankland, J. van de Streek, E. Pidcock, W. D. S. Motherwell, J. C. Cole, *J. Appl. Cryst.* **2006**, *39*, 910.

[53] *CPMD version 3.11.1*, *Copyright IBM Corp. 1990-2006, Copyright MPI für estkörperforschung Stuttgart 1997-2001*.

[54] C. A. Morrison, School of Chemistry and EaSTCHEM Research School, The University of Edinburgh, UK, Personal communication, **2007**.

[55] J. P. Perdew, K. Burke, M. Ernzerhof, *Phys. Rev. Lett.* **1997**, *78*, 1396.

[56] J. P. Perdew, K. Burke, M. Ernzerhof, *Phys. Rev. Lett.* **1996**, *77*, 3865.

[57] S. Nose, *J. Chem. Phys.* **1984**, *81*, 511.

[58] W. G. Hoover, *Phys. Rev. A* **1985**, *31*, 1695.

[59] R. Dovesi, V. R. Saunders, C. Roetti, R. Orlando, C. M. Zicovich-Wilson, F. Pascale, B. Civalleri, K. Doll, N. M. Harrison, I. J. Bush, P. D'Arco, M. Llunell, CRYSTAL06, University of Torino, Torino, **2006**.

[60] A. D. Becke, *J. Chem. Phys.* **1993**, *98*, 5648.

[61] C. Lee, W. Yang, R. G. Parr, *Phys. Rev. B* **1988**, *37*, 785.

[62] B. Miehlich, A. Savin, H. Stoll, H. Preuss, *Chem. Phys. Lett.* **1989**, *157*, 200.

[63] J. Muscat, A. Wander, N. M. Harrison, *Chem. Phys. Lett.* **2001**, *342*, 397.

[64] W. F. Perger, *Chem. Phys. Lett.* **2002**, *368*, 319.

[65] H. J. Monkhorst, J. D. Pack, *Phys. Rev. B* **1976**, *13*, 5188.

[66] M. S. Gordon, *Chem. Phys. Lett.* **1980**, *76*, 163.

[67] P. C. Hariharan, J. A. Pople, *Theor. Chim. Acta* **1973**, *28*, 213.

[68] W. J. Hehre, R. Ditchfield, J. A. Pople, *J. Chem. Phys.* **1972**, *56*, 2257.

[69] R. Krishnan, J. S. Binkley, R. Seeger, J. A. Pople, *J. Chem. Phys.* **1980**, *72*, 650.

[70] A. D. McLean, G. S. Chandler, *J. Chem. Phys.* **1980**, *72*, 5639.

[71] M. J. Frisch, G. W. Trucks, H. B. Schlegel, G. E. Scuseria, M. A. Robb, J. R. Cheeseman, J. A. Montgomery, T. V. Jr., K. N. Kudin, J. C. Burant, J. M. Millam, S. S. Iyengar, J. Tomasi, V. Barone, B. Mennucci, M. Cossi, G. Scalmani, N. Rega, G. A. Petersson, H. Nakatsuji, M. Hada, M. Ehara, K. Toyota, R. Fukuda, J. Hasegawa, M. Ishida, T. Nakajima, Y. Honda, O. Kitao, H. Nakai, M. Klene, X. Li, J. E. Knox, H. P. Hratchian, J. B. Cross, V. Bakken, C. Adamo, J. Jaramillo, R. Gomperts, R. E. Stratmann, O. Yazyev, A. J. Austin, R. Cammi, C. Pomelli, J. W. Ochterski, P. Y. Ayala, K. Morokuma, G. A. Voth, P. Salvador, J. J. Dannenberg, V. G. Zakrzewski, S. Dapprich, A. D. Daniels, M. C. Strain, O. Farkas, D. K. Malick, A. D. Rabuck, K. Raghavachari, J. B. Foresman, J. V. Ortiz, Q. Cui, A. G. Baboul, S. Clifford, J. Cioslowski, B. B. Stefanov, G. Liu, A. Liashenko, P. Piskorz, I.

Komaromi, R. L. Martin, D. J. Fox, T. Keith, M. A. Al-Laham, C. Y. Peng, A. Nanayakkara, M. Challacombe, P. M. W. Gill, B. Johnson, W. Chen, M. W. Wong, C. Gonzalez, J. A. Pople, Gaussian 03, Revision C.02 ed., Gaussian Inc, Wallingford, CT, **2004**.

[72] D. S. Middlemiss, Department of Chemistry and WestCHEM Research School, University of Glasgow, UK, Personal communication, **2007**.

[73] L. Merrill, W. A. Bassett, *Rev. Sci. Instrum.* **1974**, *45*, 290.

[74] A. R. Lennie, D. Laundy, M. A. Roberts, G. Bushnell-Wye, *J. Synchrotron Rad.* **2007**, *14*, 1.

[75] G. J. Piermarini, S. Block, J. D. Barnett, R. A. Forman, *J. Appl. Phys.* **1975**, *46*, 2774.

[76] PEARL*, Vol. ISIS 96- ISIS Facility Annual Report 1995-1996, RAL-TR-96-050*, Rutherford Appleton Laboratory, **1996**, pp. 61.

[77] PEARL*, Vol. ISIS 97- ISIS Facility Annual Report 1996-97, RAL-TR-97-050*, Rutherford Appleton Laboratory, **1997**, pp. 28.

[78] J. M. Besson, R. J. Nelmes, G. Hamel, J. S. Loveday, W. G., S. Hull, *Physica B* **1992**, *180*, 907.

[79] R. J. Nelmes, J. S. Loveday, R. M. Wilson, J. M. Besson, S. Klotz, G. Hamel, S. Hull, in *Proceedings of the Symposium on Time-of-Flight Diffraction at Pulsed Neutron Sources, Vol. 8* (Eds.: J. D. Jorgensen, A. J. Schultz), American Crystallographic Association, Buffalo, **1994**, p. 19.

[80] W. G. Marshall, D. J. Francis, *J. Appl. Cryst.* **2002**, *35*, 122.

[81] W. G. Marshall, Attenuation program for time-of-flight neutron powder-diffraction on PEARL with the Paris-Edinburgh cell, unpublished, **1996**.

[82] A. D. Fortes, *PhD Thesis* **2004**, *University of London*.

[83] A. Kuznetsov, V. Dmitriev, L. Dubrovinsky, V. Prakapenka, H. P. Weber, *Solid State Commun.* **2002**, *122*, 125.

[84] R. A. Miller, D. E. Schuele, *J. Phys. Chem. Solids* **1969**, *30*, 589.

[85] D. L. Waldorf, G. A. Alers, *J. Appl. Phys.* **1962**, *33*, 3266.

[86] It is typical in Paris–Edinburgh cells that initial pressure application and decompression results in non linear reversibility due to the friction of the piston in the cell.

[87] J. Bernstein, R. E. Davis, L. Shimoni, N.-L. Chang, *Angew. Chem. Int. Ed. Engl.* **1995**, *34*, 1555.

[88] F. H. Allen, W. D. S. Motherwell, *Acta Cryst. B* **2002**, *58*, 407.

[89] Obtained from Gaussian calculations performed for isolated molecules of the different BIPY moieties in the twisted and co-planar conformations at the 6‑31G*/B3LYP level.

[90] K. Shankland, ISIS Neutron Facility, Rutherford Appleton Laboratory, UK, Personal communication, **2008**.

[91] N. Shankland, Strathclyde Institute of Pharmacy and Biomedical Sciences, University of Strathclyde, UK, Personal communication, **2008**.

[92] J. A. Chisholm, S. Motherwell, P. R. Tulip, S. Parsons, S. J. Clark, *Cryst. Growth Des.* **2005**, *5*, 1437.

[93] H. Flyvbjerg, H. G. Petersen, *J. Chem. Phys.* **1989**, *91*, 461.

[94] K. B. Wiberg, P. R. Rablen, *J. Comput. Chem.* **1993**, *14*, 1504.

CHAPTER 4

Co-crystallisation studies involving squaric acid and 2,2'-dimethyl-4,4'-bipyridine

4.1. Introduction

The observation of temperature-induced proton transfer in the adduct formed between squaric acid and bipyridine (SQBP) prompted the design of a similar system in which proton transfer could take place, but at a lower temperature. The strategy involved selection of a substituted bipyridine that retained similar structural features but which possessed more basic character. For this reason, we selected dimethyl substituted bipyridine [2,2'-dimethyl-4,4'-bipyridine (dmBIPY), see Figure 4.1] with calculated pK_{as} of the conjugated acids of approximately 3.5 and 5.6.[1-3][4]

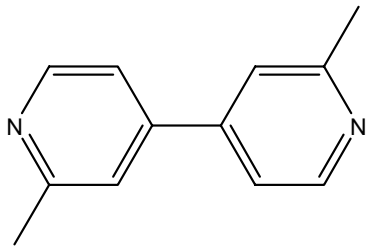

Figure 4.1. 2,2'-dimethyl-4,4'-bipyridine.

Co-crystallisation of this compound with squaric acid (SQ) did not follow the design quite as intended, but did however, yield two interesting hydrates that have the potential to exhibit proton migration or transfer.

There is precedent for hydrogen-bonded chains of water molecules in crystals to be associated with proton transfer.[5-12] In the most relevant example, clusters of four water molecules were crystallised with bis(squaryl)biphenyl, hereafter labelled BSQB.[10] In this system it was found that proton transfer occurred between molecules in one water cluster and then transmitted to the adjacent water clusters by means of a variation of charge distribution in the BSQB di-anion.[10]

In this chapter the structures of 2,2'-dimethyl-4,4'-dipyridine-squaric acid-water, in ratios 1:2:2 (denoted as co-crystal I) and 1:1:3 (denoted as co-crystal II) will be discussed.

4.2. Experimental section

4.2.1. Materials

Squaric acid (SQ) and 2,2'-dimethyl-4,4'-dipyridyl (dmBIPY) were obtained from Sigma-Aldrich and Fluorochem, respectively, and used without further purification. Equimolar quantities of both precursors [0.08 g (0.43 mmol) of dmBIPY with 0.05 g (0.44 mmol) of SQ] were mixed and dissolved in the minimum amount of water (~ 10 cm^3). The solution was then allowed to evaporate slowly over a period of three days to give red diamond-shaped blocks of co-crystal I ($2SQ.dmBIPY.2H_2O$) and red rod-like blocks of co-crystal II ($SQ.dmBIPY.3H_2O$).

4.2.2. Computational modelling

Relative proton affinities of dmBIPY with respect to BIPY were obtained using the *Gaussian98* suite of programs.[13] These were performed in the gas-phase with the orbitals expanded in terms of Gaussian-type functions of varying extents (see Table 4.1). The Hamiltonian employed was that of the B3LYP hybrid functional in order to incorporate some approximation of electronic correlation.[14, 15] It should be noted that diffuse functions were not necessary as the states of the molecules are cationic.

4.2.3. Single-crystal X-ray diffraction

Studies of co-crystal I were performed using a Bruker-Nonius Kappa CCD diffractometer, equipped with an Oxford Cryosystems low temperature device operating at 100 and 200 K, and a Bruker-Nonius APEX 2 CCD diffractometer at room temperature. The studies of co-crystal II were performed using a Bruker-Smart Apex CCD diffractometer equipped with an Oxford low temperature device at 110 K and a Bruker-Nonius Kappa CCD diffractometer at 300 K. All instruments applied a Mo-Kα radiation ($\lambda = 0.71073$Å) source. Data reduction was performed using *SAINT*.[16] An absorption correction was applied using the multiscan procedure program *SADABS*.[17] Structures were solved by direct methods using the *SIR92*[18] package, and refined using full-matrix least squares against $|F|^2$ using *CRYSTALS*.[19] The non-hydrogen atoms were refined with anisotropic thermal parameters. Hydrogen atom positions associated with C–H bonds of the dmBIPY molecules were placed in geometrically calculated positions and allowed to regularise with respect to Fourier difference peaks. The remaining H-atoms were located through the use of Fourier difference maps at 100 K with a subsequent riding model being applied.[20]

4.3. Results and discussion

4.3.1. Computational modelling

Equilibrium structures for the three possible protonation states of BIPY and dmBIPY were calculated for isolated molecules. Comparing the relative variation in Mulliken charges on the nitrogen atoms for both molecules allowed the relative shift in basicity to be assessed. It should be noted however, that the absolute values have little formal meaning and are strongly dependent on which basis set is used.[21] Furthermore, the energies of the individual compounds were also extracted from the calculations. While their direct comparison is not meaningful (as mass balance is not maintained) comparison of the relative stabilities of BIPY *vs.* dmBIPY for the different states of protonation does allow conclusions to be drawn. The results from the calculations are presented in Table 4.1, and indicate that dmBIPY has a higher

proton affinity than BIPY as the nitrogen atoms on dmBIPY carry a more negative charge. Moreover, the calculations also confirm that both protonated states of dmBIPY are more stable than those of BIPY. Thus the calculations support the rationale behind the choice of precursors.

It was also seen, from the calculations, that the variation in the electronic structure of the heterocycle (due to methyl substitution) had little effect on the torsion angle as the equilibrium structures of both BIPY and dmBIPY gave similar values (~ 36°). It should be noted that frequency calculations demonstrated that these were stable structures and that similar starting geometries were pursued in order to overcome the fact that the energy barrier of the ring rotation is low (see Chapter 3).

Table 4.1. The effective Mulliken charges, q (e), borne by the nitrogen atoms of BIPY and dmBIPY and the internal energy differences (kJ mol^{-1}) separating the different protonation levels of the BIPY versus dmBIPY molecules as a function of basis set size; $1^{st}\Delta E$ = [E(dmBIPYH$^+$) - E(dmBIPY)] - [E(BIPYH$^+$) - E(BIPY)], $2^{nd}\Delta E$ = [E(dmBIPYH$_2^{2+}$) - E(dmBIPYH$^+$)] - [E(BIPYH$_2^{2+}$) - E(BIPYH$^+$)], Total ΔE = [E(dmBIPYH$_2^{2+}$) - E(dmBIPY)] - [E(BIPYH$_2^{2+}$) - E(BIPY)].

	q(BIPY)	q(dmBIPY)	1^{st} ΔE	2^{nd} ΔE	Total ΔE
6–31G*	—	—	-22.06	-32.25	-54.31
6–311G**	-0.286	-0.317	-20.41	-31.26	-51.67

4.3.2. Single-crystal X-ray diffraction studies

SQ and dmBIPY crystallised under ambient conditions as both a co-crystal I (formed as diamond-like crystals) and as a co-crystal II (to give rod-like crystals) both of which are red (see Figure 4.2). The crystal structures of the hydrates will be the focus of the remainder of this section.

Figure 4.2. Optical image of a single crystal of co-crystal I (left) and co-crystal II (right) at room temperature.

4.3.2.1. Co-crystal I (2SQ.dmBIPY.2H_2O)

The asymmetric unit of co-crystal I comprises half a molecule of doubly protonated dmBIPY, one molecule of SQ (with two disordered protons) and one molecule of water (also with two disordered protons) in general positions (see Figure 4.3). The dmBIPY molecules lie on an inversion centre, as does the proton shared by two SQ molecules. The proton that is shared between two water molecules lies on a 2-fold axis. The unit cell (see Table 4.2) contains four molecules of dmBIPY (with a torsion angle between the heterocyclic rings of 0°) and eight molecules of SQ and water that lie on the (40-2) planes.

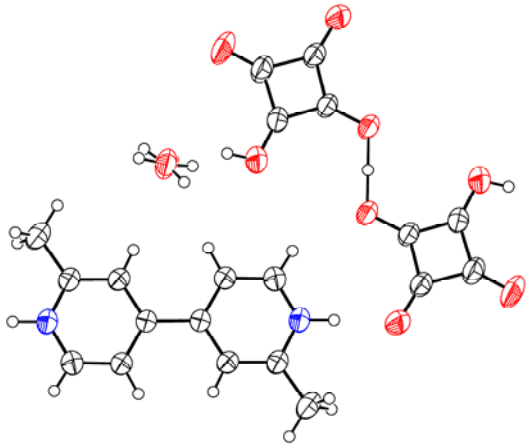

Figure 4.3. Extended asymmetric unit of co-crystal I at 295 K. Displacement ellipsoids are drawn at the 50% probability level.

Table 4.2. Crystal details for co-crystal I as a function of temperature.

	co-crystal I		
Chemical formula	$C_{20}H_{20}N_2O_{10}$		
M_r (g mol^{-1})	448.39		
Crystal system, space group	monoclinic, *C*2/*c*		
Temperature (K)	295	200	100
a	14.456(3)	13.256(3)	13.056(3)
b	12.681(3)	12.685(3)	12.664(3)
c (Å)	12.384(3)	12.437(3)	12.492(3)
β (°)	107.45(3)	107.35(3)	107.44(3)
V (Å^3)	2165.7(9)	1996.2(9)	1970.5(9)
Z	4	4	4
ρ_{calc} (g cm^{-3})	1.375	1.492	1.511
Radiation type	Mo *K*α	Mo *K*α	Mo *K*α
Crystal form, colour	Block, red		
Crystal size (mm)	0.15 x 0.23 x 0.38	0.10 x 0.16 x 0.40	0.10 x 0.16 x 0.40

The most interesting motif in the structure is the $D_3^3(16)$ finite chains formed by the short O–H···O hydrogen bond (2.49 Å) between SQ molecules and two symmetrically equivalent O–H···O hydrogen bonds (2.70 Å) between SQ and water molecules (see rectangle in Figure 4.4). These are interconnected through O–H···O bonds (2.59 and 2.70 Å) represented by a $R_4^4(14)$ ring (see circled motif in Figure 4.4)[22], which in turn are connected to dmBIPY molecules *via* two equivalent N–H···O hydrogen bonds (2.71 Å) (represented by a $D_2^2(11)$ finite chain, see ellipse in Figure 4.4). These layers are connected by the H-bond formed between the two water molecules that share a proton (2.78 Å), leading to an interlayer distance of *ca.* 3.4 Å (see Figure 4.5).

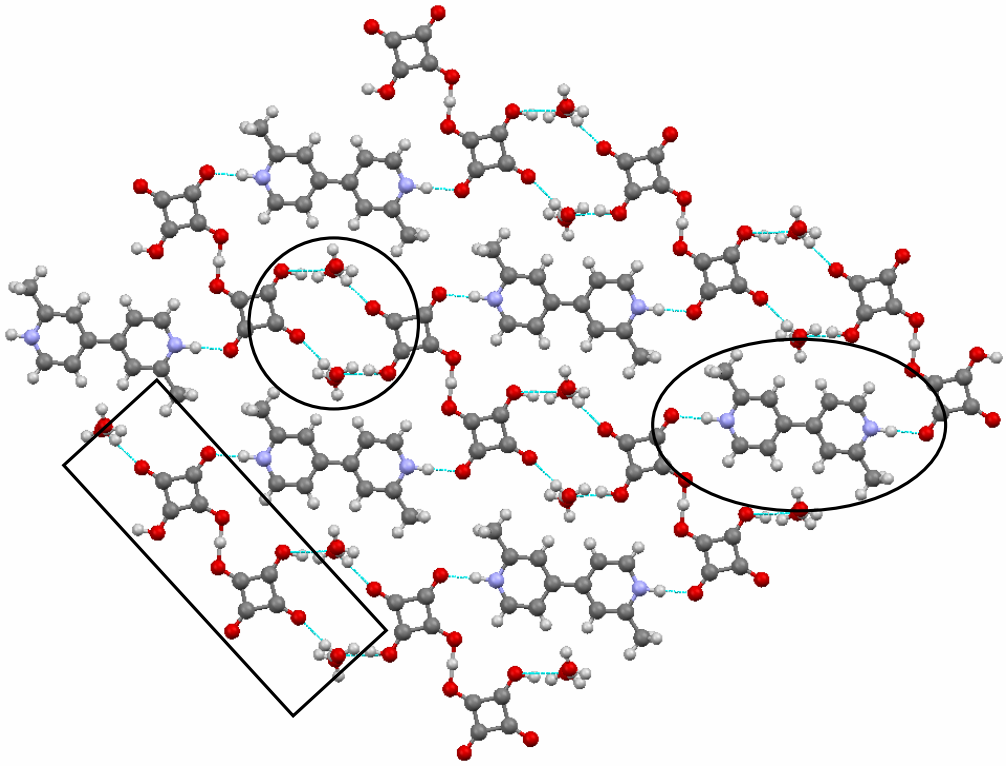

Figure 4.4. View of the (40-2) co-crystal I planes.

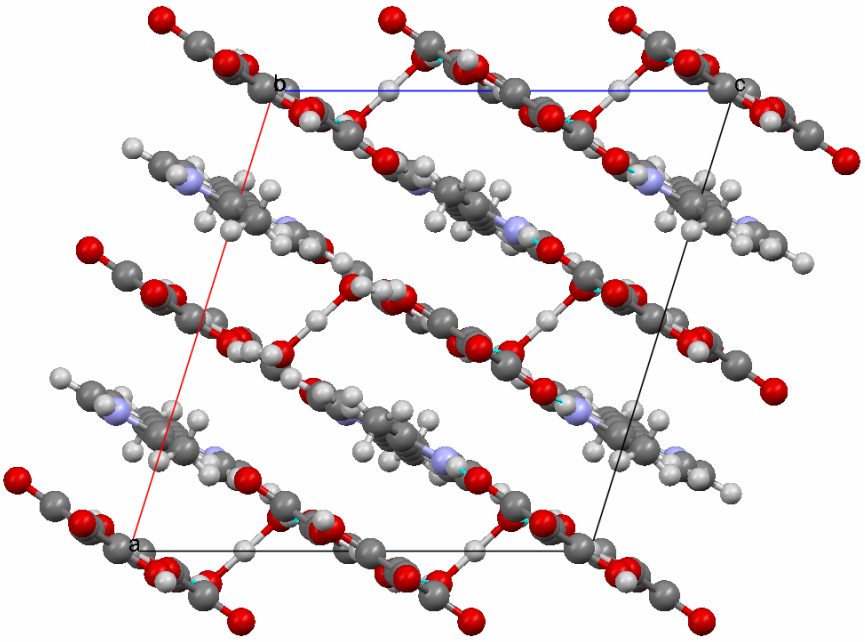

Figure 4.5. Co-crystal I view of the *ac* plane.

The arrangement of the molecules in this structure to form planar layers is very similar to that observed for the high temperature form of SQBP described in Chapter 3. Furthermore, co-crystal I is also red, this reinforces the idea that this is a consequence of the presence of doubly protonated bipyridine or dimethyl bipyridine molecules. In order to investigate whether or not proton transfer could also be observed in the solid state, single-crystal diffraction experiments were performed at lower temperatures of 200 and 100 K. Table 4.2 shows the variation in lattice parameters with temperature. The most striking variation is the very large decrease along the *a*- axis (reduced by 10 % from 295 K to 100 K). This causes a large decrease in unit-cell volume (9 %) between these temperatures. The main cause of this large decrease in the *a*- axis is the reduction in the O···O distance, associated with the interlayer separation, from 2.78 to 2.66 Å (see Table 4.3). This contact involves the disordered hydrogen atoms associated with two water molecules. Although at these lower temperatures the hydrogen atoms remain disordered, it appeared that as temperature was decreased the hydrogen bonding between the layers was strengthened.

Table 4.3. Selected intermolecular parameters (Å) of co-crystal I as a function of temperature.

Distances	295 K	200 K	100 K
$D_3^3(16)$			
O–H···O (SQ – SQ)	2.486(1)	2.475(1)	2.478(1)
O–H···O (SQ – H_2O)	2.702(2)	2.703(3)	2.702(3)
$R_4^4(14)$			
O–H···O	2.586(2) / 2.702(2)	2.594(3) / 2.703(3)	2.586(3) / 2.702(3)
$D_2^2(11)$			
N–H···O	2.706(2)	2.716(4)	2.712(3)
Interlayer			
O–H···O (H_2O – H_2O)	2.776(3)	2.656(4)	2.662(4)
***r* Interlayer**	3.44(3)	3.19(3)	3.16(3)

The parameters of the squaric acid molecules were followed and compared with those of SQBP (see Table 4.4). These show no appreciable change, indicating that the protons remain firmly attached to the dmBIPY molecules at all temperatures. It remains to be seen if data collection at still lower temperature would cause the protons to move, or whether this would cause the hydrogen atoms to become ordered.

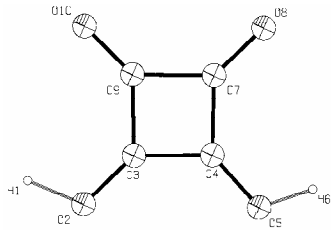

Figure 4.6. The numbering scheme used in Table 4.4 for the SQ molecules.

Table 4.4. Selected parameters (Å) from SQ molecules for both co-crystal I and SQBP (see Chapter 3).

Distances	co-crystal I			co-crystal II		SQBP Form I	SQBP Form II
	295 K	200 K	100 K	300 K	110 K	180 K	453 K
C_3=C_4	1.422(2)	1.421(4)	1.432(3)	1.455(7)	1.462(3)	1.419(2)	1.436(4)
C_4–C_7 / C_3–C_9	1.481(2) / 1.454(2)	1.473(5) / 1.449(4)	1.485(4) / 1.452(3)	1.451(6) / 1.464(7)	1.464(3) / 1.475(3)	1.452(2) / 1.490(2)	1.446(5)
C_7–C_9	1.498(2)	1.500(5)	1.503(4)	1.466(7)	1.482(3)	1.504(2)	1.465(5)
O_2–C_3 / C_4–O_5	1.285(2) / 1.283(2)	1.274(4) / 1.279(3)	1.270(3) / 1.276(3)	1.253(5) / 1.257(6)	1.257(2) / 1.254(3)	1.265(2) / 1.311(2)	1.267(4)
C_7=O_8 / C_9=O_{10}	1.218(2) / 1.254(2)	1.227(5) / 1.237(4)	1.224(3) / 1.242(3)	1.268(5) / 1.239(6)	1.256(2) / 1.237(3)	1.228(2) / 1.221(2)	1.225(4)

4.3.2.2. Co-crystal II (SQ.dmBIPY.3H_2O)

Co-crystal II crystallises with one molecule of doubly protonated dmBIPY, one molecule of deprotonated SQ and three water molecules in general positions of the asymmetric unit (space group $P2_1/n$) as seen in Figure 4.7. This leads to a unit cell (see Table 4.5) that comprises four molecules of SQ^{2-} and $dmBIPYH_2^{2+}$ (with a torsion angle between the heterocyclic rings of 24.2°), and twelve water molecules.

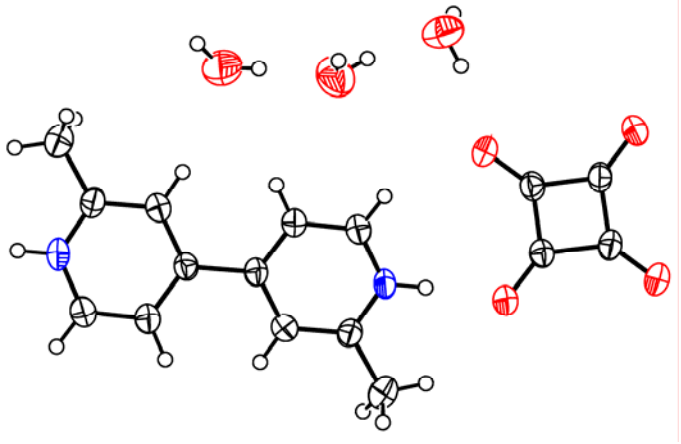

Figure 4.7. Asymmetric unit of co-crystal II at 300 K. Displacement ellipsoids are drawn at the 50% probability level.

Table 4.5. Crystal details for co-crystal II.

	Co-crystal II	
Chemical formula	$C_{16}H_{20}N_2O_7$	
M_r (g mol^{-1})	352.34	
Crystal system, space group	monoclinic, $P2_1/n$	
Temperature (K)	300	110
a *b* *c* (Å)	15.107(3) 6.7896(14) 16.679(3)	15.1101(4) 6.6834(2) 16.5867(4)
β (°)	101.63(3)	101.66(2)
V (Å^3)	1675.6(6)	1640.5(8)
Z	4	4
ρ_{calc} (g cm^{-3})	1.397	1.427
Radiation type	Mo *Kα*	Mo *Kα*
Crystal form, colour	Block, red	
Crystal size (mm)	0.13 x 0.14 x 0.43	0.13 x 0.14 x 0.43

SQ and dmBIPY are connected primarily through N–H···O hydrogen bonds (2.59 and 2.70 Å) that form $C_2^2(15)$ chains (see rectangle in Figure 4.8) that zig-zag along the (040) planes. These "stair-like" chains contain three hydrogen-bonded water molecules (with O–H···O distances of 2.69, 2.78, 2.81 and 2.84 Å), presumably to fill the voids in the structure that are a consequence of the bulky CH_3 groups, forming $C_4^4(12)$ chains (see ellipse in Figure 4.8). Furthermore, the water molecules assist in forming contacts (O–H···O of 2.92 Å) between the zig-zagging layers that are separated by *ca.* 3.39 Å (see Figure 4.9).

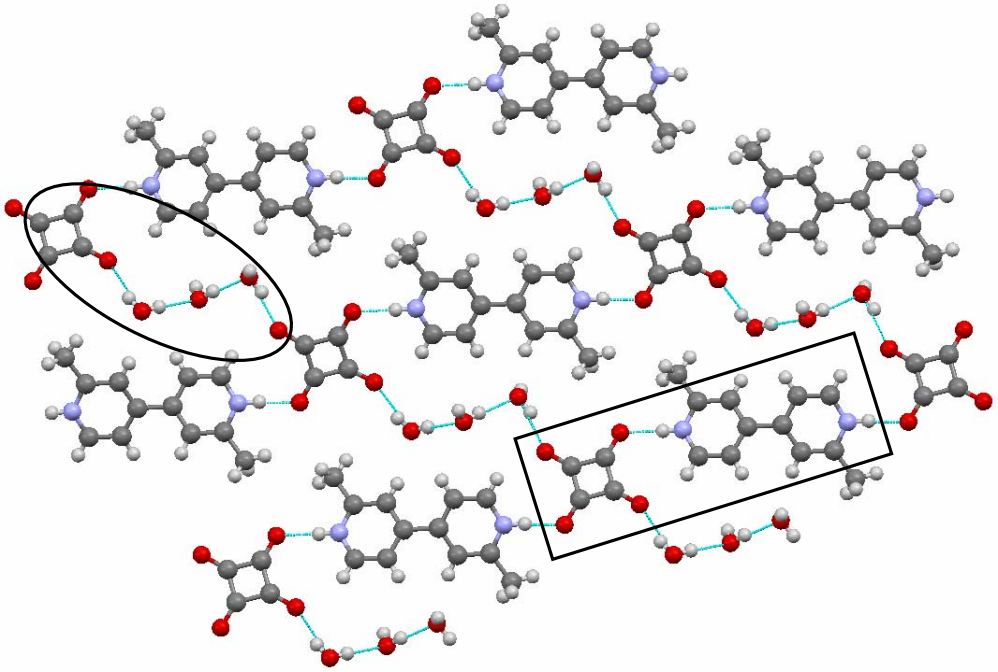

Figure 4.8. View of the (040) co-crystal II planes.

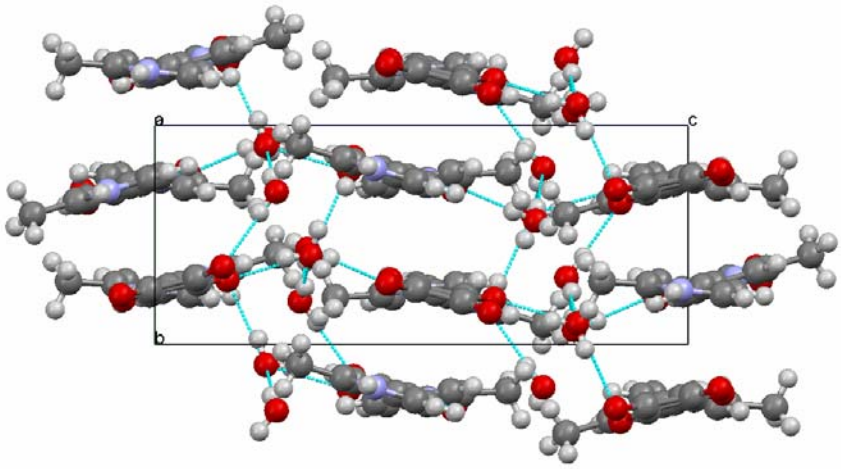

Figure 4.9. Co-crystal II view of the *bc* plane.

The colour of the crystals was red and this again supports the conclusion that this is controlled by the degree of protonation of the bipyridine or dimethyl bipyridine molecules. Single-crystal diffraction experiments were performed at a lower temperature and the geometries of the H-bonds were followed (see Table 4.6). One of the N–H···O bonds increased by 0.004 Å and the other decreased by 0.015 Å, thereby becoming slightly more symmetrical at 110 K (with an average of 2.64(6) Å *cf.* 2.6 Å in the case of SQBP). The maximum deviations were observed for the O–H···O bonds and interlayer distance, as with co-crystal I, but the decrease was smaller (1–2 %). The volume of the unit cell decreased by 2 %.

On the basis of the parameters of the squaric acid molecules (see Table 4.4) no evidence for proton migration or transfer was observed over this temperature range. This does not exclude, however, the possibility that at lower temperatures proton migration could occur.

Table 4.6. Selected parameters (Å) of co-crystal II as a function of temperature.

Distances	300 K	110 K
$C_2^2(15)$		
N–H···O	2.588(5) / 2.695 (5)	2.592(2) / 2.680(2)
$C_4^4(12)$		
O–H···O (H_2O – H_2O)	2.814(6) / 2.840(7)	2.794(3) / 2.832(3)
O–H···O (SQ – H_2O)	2.693(5) / 2.782(5)	2.686(2) / 2.780(2)
Interlayer		
O–H···O	2.916(6)	2.875(2)
***r* Interlayer**	3.39(2)	3.34(2)

4.4. Conclusions

It was found that, as expected, the methyl substitution encourages protonation of the heterocycle molecules. However, no indication of temperature-induced proton migration was observed. This may be because substitution of the BIPY with two methyl groups increases its basicity to too great an extent, *i.e.* the protons are too firmly attached to the nitrogen.

Both co-crystals that resulted from this study were red, but had different torsion angles between the heterocyclic rings. This is a further support for the conclusion that it is the doubly protonated BIPY or substituted BIPY that is responsible for the red colour of these systems.

Furthermore, it can be concluded that the methyl substitution appears to encourage formation of hydrates by incorporation of water molecules into the structure in order to fill the voids created by the bulky methyl groups.

4.5. Bibliography

[1] A. Albert, R. Goldacre, J. Phillips, *J. Chem. Soc.* **1948**, 2240.

[2] L. A. Ashton, J. I. Bullock, P. W. G. Simpson, *J. Chem. Soc., Faraday Trans.* **1982**, *78*, 1961.

[3] http://www.chemaxon.com/demosite/marvin/index.html, (Ed.: Chemaxon), **2007**.

[4] pKa values of the respective conjugate acids of BIPY and dmBIPY were calculated using the ChemAxon Marvin pKa calculator. The difference between these calculated values was then added to the experimental value that has been measured for BIPY. Thus obtaining an estimate of the pKa for the conjugate acids of dmBIPY.

[5] K. Edman, P. Nollert, A. Royant, H. Beirhali, E. Pebay-Peyroula, J. Hajdu, R. Neutze, E. M. Landau, *Nature* **1999**, *401*, 822.

[6] H. Luecke, B. Schobert, H.-T. Richter, J.-P. Cartailler, J. K. Lanyi, *Science* **1999**, *286*, 255.

[7] S. Yoshikawa, K. Shinzawa-Itoh, R. Nakashima, R. Yaono, E. Yamashita, N. Inoue, M. Yao, M. J. Fei, C. P. Libeu, T. Mizushima, H. Yamaguchi, T. Tomizaki, T. Tsukihara, *Science* **1998**, *280*, 1723.

[8] T. Tsukihara, H. Aoyama, E. Yamashita, T. Tomizaki, H. Yamaguchi, K. Shinzawa-Itoh, R. Nakashima, R. Yaono, S. Yoshikawa, *Science* **1996**, *272*, 1136.

[9] R. Henderson, J. M. Baldwin, T. A. Ceska, F. Zemlin, E. Beckmann, K. H. Downing, *J. Mol. Biol.* **1990**, *213*, 899.

[10] H. Terao, T. Sugawara, Y. Kita, N. Sato, E. Kaho, S. Takeda, *J. Am. Chem. Soc.* **2001**, *123*, 10468.

[11] L. E. Cheruzel, M. S. Pometun, M. R. Cecil, M. S. Mashuta, R. J. Wittebort, R. M. Buchanan, *Angew. Chem. Int. Ed.* **2003**, *42*, 5452.

[12] M. K. Kabir, H. Tobita, H. Matsuo, K. Nagayoshi, K. Yamada, K. Adachi, Y. Sugiyama, S. Kitagawa, S. Kawata, *Cryst. Growth Des.* **2003**, *3*, 791.

[13] M. J. Frisch, G. W. Trucks, H. B. Schlegel, G. E. Scuseria, M. A. Robb, J. R. Cheeseman, V. G. Zakrzewski, J. A. M. Jr., R. E. Stratmann, J. C. Burant, S. Dapprich, J. M. Millam, A. D. Daniels, K. N. Kudin, M. C. Strain, O. Farkas,

J. Tomasi, V. Barone, M. Cossi, R. Cammi, B. Mennucci, C. Pomelli, C. Adamo, S. Clifford, J. Ochterski, G. A. Petersson, P. Y. Ayala, Q. Cui, K. Morokuma, D. K. Malick, A. D. Rabuck, K. Raghavachari, J. B. Foresman, J. Cioslowski, J. V. Ortiz, A. G. Baboul, B. B. Stefanov, G. Liu, A. Liashenko, P. Piskorz, I. Komaromi, R. Gomperts, R. L. Martin, D. J. Fox, T. Keith, M. A. Al-Laham, C. Y. Peng, A. Nanayakkara, C. Gonzalez, M. Challacombe, P. M. W. Gill, B. Johnson, W. Chen, M. W. Wong, J. L. Andres, C. Gonzalez, M. Head-Gordon, E. S. Replogle, J. A. Pople, Gaussian 98, Revision A.7 ed., Gaussian Inc, Pittsburgh, PA, **1998**.

[14] A. D. Becke, *J. Chem. Phys.* **1993**, *98*, 5648.

[15] B. Miehlich, A. Savin, H. Stoll, H. Preuss, *Chem. Phys. Lett.* **1989**, *157*, 200.

[16] SAINT Area-Detector Software Package v7.01A, Bruker - AXS, Madison, Wisconsin, USA, **2003**.

[17] G. M. Sheldrick, SADABS v2.04, University of Gottigen, Germany, **2001**.

[18] A. Altomare, G. Cascarano, C. Giacovazzo, A. Guagliardi, *J. Appl. Cryst.* **1993**, *26*, 343.

[19] D. J. Watkin, C. K. Prout, J. R. Carruthers, P. W. Betteridge, R. I. Cooper, CRYSTALS v12 ed., Chemical Crystallography Laboratory, Oxford, UK, **2003**.

[20] I. D. H. Oswald, School of Chemistry and EaSTCHEM Research School, The University of Edinburgh, UK, Personal Communication, **2007**.

[21] K. B. Wiberg, P. R. Rablen, *J. Comput. Chem.* **1993**, *14*, 1504.

[22] It should be noted that both protons that possess half occupancy were considered as one.

CHAPTER 5

Structural studies of the 2:1 adduct formed between N,N-dimethylurea and phosphoric acid

5.1. Introduction

The adduct formed between urea and phosphoric acid (UPA) has been shown to exhibit migratory behaviour of the proton occupying the short, strong hydrogen bond (SSHB) formed between the precursors.[1] The proton position was found to change by as much as 0.1 Å from urea towards the centre of the hydrogen bond as the temperature was increased from 15 to 300 K.[1-4] In an effort to understand this phenomenon better, co-crystallisations of similar compounds were performed. Urea was replaced with a series of methyl-substituted urea (specifically methylurea, N,N-dimethylurea, N,N'-dimethylurea and tetramethylurea). From these co-crystallisations only crystals of the adduct formed between N,N-dimethylurea and phosphoric acid (dmUPA) were obtained. The crystal structure shared many structural features with the parent UPA, and crucially three different SSHBs were observed, making this new material a potential candidate for proton migration.

The structure of dmUPA was studied using variable temperature X-ray diffraction and computational methods, the results of which will be discussed in this chapter.

5.2. Experimental and computational methods

5.2.1. Materials

N,N-dimethylurea and phosphoric acid were obtained from Sigma-Aldrich and used without further purification. Crystals of the 2:1 adduct were grown by combining equimolar quantities of both precursors [0.43 g (4.88 mmol) of dimethylurea with 0.62 g (4.95 mmol) of phosphoric acid] in the minimum amount of hot water that allowed dissolution (~ 3 cm^3). The mixture was then allowed to evaporate slowly until crystal formation occurred after a period of 12 months. It should be noted that from the many crystallisation attempts of this adduct, crystals of ammonium dihydrogen phosphate (identified by single-crystal diffraction) were also obtained, presumably as a hydrolysis product from a competing reaction. Similar conditions were used for the attempted co-crystallisations of the other methyl-substituted ureas, but no solid products were obtained.

5.2.2. Single-crystal X-ray diffraction

Studies of the dmUPA adduct were performed using a Bruker-Smart Apex CCD diffractometer equipped with an Oxford low temperature device at 110, 200 and 300 K using a Mo-Kα radiation (λ = 0.71073Å) source. The data reduction was performed using *SAINT*.[5] An absorption correction was applied using the multiscan procedure program *SADABS*.[6] Structures were solved by direct methods using the *SIR92*[7] package, and refined using full-matrix least squares against $|F|^2$ using *CRYSTALS*.[8] The non-hydrogen atoms were refined with anisotropic thermal parameters. Hydrogen atom positions associated with C–H and N–H bonds of the dimethylurea molecules were placed in geometrically calculated positions and allowed to regularise with respect to Fourier difference peaks. The hydrogen atoms of the phosphoric acid molecules were located through the use of Fourier difference maps at 110 K with a subsequent riding model being applied. Furthermore these H positions were used in the refinement of the structures at subsequent temperatures.

5.2.3. Computational modelling

5.2.3.1. Proton affinities

Relative proton affinities of dmUPA with respect to UPA were obtained using the *Gaussian98* suite of programs.[9] These were performed in the gas-phase for isolated dimers of dmUPA and UPA at the 6–31G*/B3LYP level.[9-15]

5.2.3.2. Geometry optimisation

Equilibrium structures for dmUPA were obtained using the *CPMD* simulation package.[16] Initial geometries, unit cells and space group symmetry constraints were taken from the X-ray experiments. Electronic exchange and correlation were modeled using the gradient-corrected functional of Perdew, Burke and Ernzerhof (PBE).[17, 18] Core electrons were treated using a set of Vanderbilt ultra-soft pseudopotentials, while valence electrons were represented by a plane-wave basis set truncated at an extended energy cutoff of 30 Ry. Calculations were pursued on a 2x1x1 supercell, as the *a*- axis of the structure is shorter than the other two, in order to create a simulation model of more cubic dimensions. The electronic band structures were then sampled at the Γ- point only.

5.2.3.3. Molecular dynamics

Car-Parrinello molecular dynamics (MD) simulations (within the NVT ensemble), were performed at 50 and 300 K for the supercell approach. Both used a time step of 3.0 a.u. (1 a.u. = 0.0241888428 fs), coupled to Nosé-Hoover thermostat[19, 20] chains for each vibrational degree of freedom at a characteristic frequency of 3500 cm^{-1}.[21] An electronic mass parameter of 400 a.u. was employed. Trajectories were collected for *ca.* 1 ps.

5.2.3.4. Potential energy surfaces

A series of single-point energy calculations were undertaken where proton positions were shifted in set increments along the O···O bond vectors for the three different SSHBs found in the asymmetric unit of the crystal structure of dmUPA. The calculations were performed for both the crystal and gas phase structures. In the latter case the calculations were pursued by extracting a set of dimers from the

crystal lattice and subsequently optimising the atomic coordinates in a 12×12×12 Å supercell, thus decoupling the SSHBs of interest from the remaining interactions (including those between neighbouring simulation cells). The resulting potential energy surfaces (PESs) were then fitted to a sixth-order polynomial that subsequently formed the input for a one-dimensional Schrödinger equation solver that operated by application of a shooting algorithm incorporating fifth-order numerical integration.[22] This process determined the ground vibrational state and subsequent wavefunction for a proton, from which the quantum expectation value for the O–H bond was obtained. The bond distance was therefore corrected for the effects of zero-point energy, which would otherwise be absent from the simulated values. It has been shown that these corrected values are in much closer agreement with experimental parameters for hydrogen bonds.[22] In an effort to compare the effects of differences in electronic structure and crystal packing arrangements between UPA and dmUPA, two further PESs were calculated. These attempted to mimic the behaviour of the urea-phosphoric acid adduct in the packing arrangement of the dimethyl analogue and *vice versa*. This was achieved by simply replacing the CH_3 groups of dmUPA for H atoms in the first model, and replacing two adjacent H atoms of the base in UPA for CH_3 groups in the second, with distance parameters for the new bonds altered to suitable values (*i.e.* r N–CH_3 ~ 1.46 Å and r N–H ~ 1.02 Å).

5.3. Results and discussion

5.3.1. Proton affinities

Equilibrium structures for dmUPA and UPA dimers were calculated in the gas-phase. Comparing the relative variation in Mulliken charge on the nitrogen atoms for both bases (urea and dimethylurea) gave valuable insight into the relative shift in basicity. It should be noted that the absolute values have little formal meaning and are strongly dependent on which basis set is used.[23] The results from the calculations are presented in Figure 5.1 and in Table 5.1. These indicate that: the acid and the base interact more strongly in the case of dmUPA than in UPA; the C=O

bond length has increased (in dmUPA relative to UPA) and consequently becomes more involved in the hydrogen-bonding; and that the hydrogen atom along the O···O SSHB has moved closer to the dimethylurea molecule. Given that temperature-induced proton migration is observed for UPA in the solid state, this result strongly suggested that a similar migration should occur in dmUPA. Thus, the calculations support the rationale behind the choice of precursors, *i.e.* dimethylurea interacts more strongly with phosphoric acid than urea does.

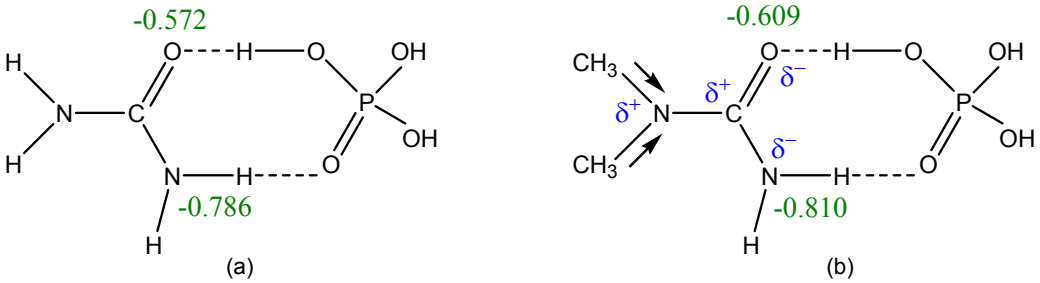

Figure 5.1. Diagram of the (a) UPA and (b) dmUPA dimers. The values in green denote the calculated Mulliken charges.

Table 5.1. Comparison of selected parameters from the dimer calculations (distances in Å).

	UPA	dmUPA
C=O	1.243	1.251
N–H	1.027	1.026
P=O	1.494	1.486
P–OH	1.572	1.585
O–H	1.016	1.021
O–H···O	2.611	2.591
N–H···O	2.865	2.865

5.3.2. X-ray structures

The crystal structure obtained for dmUPA is significantly different from that observed for UPA, in that the ratio of base to acid is now 2:1. The two symmetrically inequivalent dimethylurea molecules give rise to two SSHBs upon coordination to a central phosphoric acid molecule (see Figure 5.2). In order to distinguish them, these have been categorised with respect to the assisting H-bonds (N–H···O and N–H···OH) as $SSHB_1$ and $SSHB_2$, respectively. Applying the symmetry constraints

commensurate with the space group setting $P2_12_12_1$ created a unit cell comprising four molecules of phosphoric acid and eight molecules of dimethylurea (see Table 5.2).

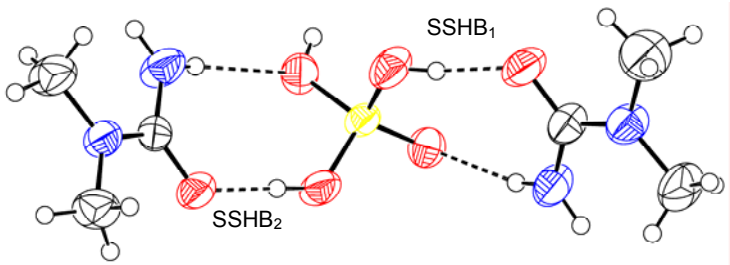

Figure 5.2. Asymmetric unit of dmUPA at 300 K. Displacement ellipsoids are drawn at the 50% probability level.

Table 5.2. Crystal details for dmUPA as a function of temperature.

	dmUPA		
Chemical formula	$C_6H_{19}N_4O_6P$		
M_r (g mol^{-1})	274.22		
Crystal system, space group	orthorhombic, $P2_12_12_1$		
Temperature (K)	300	200	110
a *b* *c* (Å)	6.3171(13) 11.305(2) 18.310(4)	6.2908(13) 11.037(2) 18.368(4)	6.2708(13) 10.867(2) 18.403 (4)
V (Å^3)	1307.7(5)	1275.3(4)	1254.1(4)
Z	4	4	4
ρ_{calc} (g cm^{-3})	1.393	1.428	1.452
Radiation type	Mo K α	Mo K α	Mo Kα
Crystal form, colour	Block, colourless		
Crystal size (mm)	0.11 x 0.14 x 0.37	0.24 x 0.28 x 0.53	0.24 x 0.28 x 0.53

The phosphoric acid and dimethylurea molecules are connected primarily through short O–H···O hydrogen bonds (2.42 Å for $SSHB_2$ and 2.45 Å for $SSHB_1$). Additional moderate N–H···OH and N–H···O hydrogen bonds (3.11 and 3.04 Å as shown in Table 5.3) give rise to two $R_2^2(8)$ rings (see Figure 5.2). The remaining hydrogen atom on the acid is involved in a short O–H···O hydrogen bond (2.52 Å) with another acid molecule (denoted PA–PA), forming $C_2^2(8)$ chains repeated along

the *a*- axis that are assisted by two further N–H···OH hydrogen bonds (2.96 and 3.04 Å) as shown in Figure 5.3. These chains are mapped through a 2_1 screw axis leading to a propeller-like structure (see Figure 5.4).

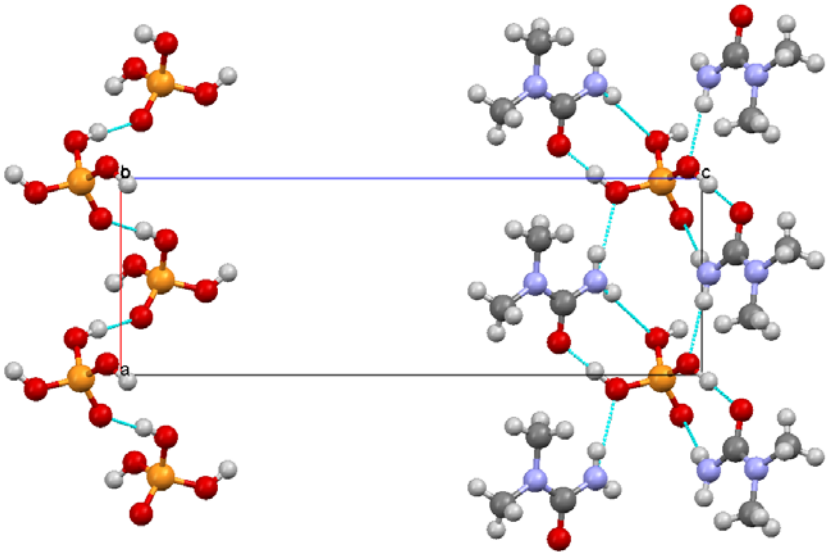

Figure 5.3. Chain of dmUPA molecules viewed along the *b*- axis. Note for purposes of clarity the dimethylurea molecules on the left are omitted and on the right only half of the propeller-like structure is presented.

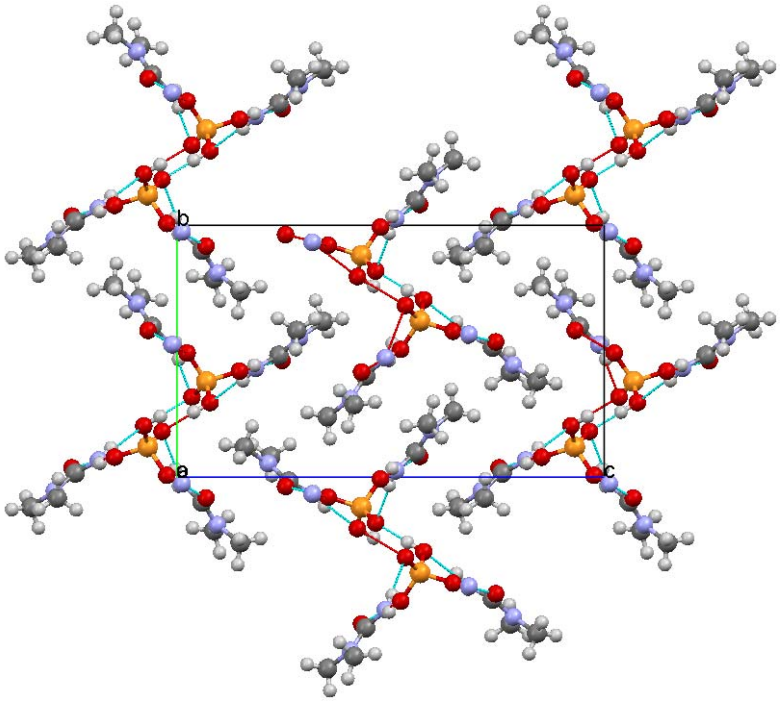

Figure 5.4. The crystal structure of dmUPA viewed along the *a*- axis.

In an attempt to gather evidence for proton migration in dmUPA, three variable temperature single-crystal X-ray diffraction experiments were performed. Over the temperature range studied (300–110 K), it was found that the volume decreased by *ca.* 4 %, with major contribution being along the *b*- axis (see Table 5.2). Inspection of Figure 5.4 shows that there are no significant interactions along this direction and so the contraction is presumably due to the hydrophobic areas where the methyl groups are bound solely by weak van der Waals forces.

Key structural parameters relating to the atoms prone to be affected by proton migration were also monitored and are presented in Table 5.3. Analysis of the X-ray structures revealed that at 300 K the protons appeared located on the phosphoric acid, which was in accordance with the study of UPA. The short O···O hydrogen bonds present in the structure did not change significantly with temperature, and so mirror the observations for UPA.[1-3] Bond lengths obtained for C=O and P–OH (involved in the PA–PA H-bonds) also did not change significantly. The P–OH bonds involved in $SSHB_1$ and $SSHB_2$ increased slightly as temperature was decreased. This was also observed in UPA.[4] The P=O bond length also increased with decreasing temperature, which did not happen in the case of UPA. However, this may be due to the fact that the N···O hydrogen bond decreased, and as a result the oxygen atoms of the acid become more involved in the hydrogen bonding. Furthermore, it was found that even at the lowest temperature (110 K), the protons were located on the phosphoric acid. This is in marked contrast with UPA, where the protons were located on the urea molecule at low temperatures. Clearly these minor structural changes show that proton migration does not occur in this system at least over this temperature range. A plausible explanation for this may be the fact that each phosphoric acid molecule interacts with two molecules of dimethylurea, which in effect weakens its acidity and inhibits proton migration. To explore this idea further, theoretical modelling was pursued and will be the focus of the remainder of this chapter.

Table 5.3. Comparison of selected parameters from experimental and computed structures of dmUPA as a function of temperature (distances in Å).

Geometry	dmUPA				UPA[24]
	X–ray (300 K) [b]	X–ray (200 K)	X–ray (110 K)	Calculated (0K)	neutron (150K)
Intermolecular					
$R_2^2(8)$					
O–H···O [a] (PA–dmU)	2.417(4) / 2.445(4)	2.419(2) / 2.445(2)	2.414(2) / 2.440(2)	2.399 / 2.435	2.411(2)
N–H···OH	3.114(5)	3.075(3)	3.051(2)	3.030	—
N–H···O	3.043(5)	3.002(3)	2.987(2)	2.945	2.946(2)
$C_2^2(8)$					
O–H···O (PA–PA)	2.521(4)	2.518(2)	2.514(2)	2.508	—
N–H···OH	2.958(4) / 3.021(4)	2.938(2) / 2.997(2)	2.920(2) / 2.976(2)	2.911 / 2.966	—
PA					
P=O	1.481(3)	1.493(2)	1.496(1)	1.522	1.509(2)
P–OH [a] (PA–dmU)	1.521(3) / 1.533(3)	1.525(2) / 1.545(2)	1.533(1) / 1.549(1)	1.554 / 1.577	1.511(2), 1.552(2), 1.568(2)
P–OH (PA–PA)	1.555(3)	1.560(2)	1.564(1)	1.591	
O–H [a] (PA dmU)	0.829(3) / 0.827(3)	0.834(2) / 0.841(2)	0.916(1) / 0.928(1)	1.198 / 1.117	0.991(4), 1.004(4), 1.253(4)
O–H (PA–PA)	0.825(3)	0.830(2)	0.871(1)	1.049	
dmU					
C=O [a]	1.266(5) / 1.254(5)	1.270(3) / 1.262(2)	1.273(2) / 1.265(2)	1.295 / 1.284	1.292(2)
C–NH$_2$ [a]	1.345(5) / 1.328(5)	1.345(3) / 1.341(3)	1.345(2) / 1.346(2)	1.347 / 1.353	1.324(2)
N–H [a]	0.858(3) / 0.858(3)	0.861(2) / 0.869(2)	0.857(1) / 0.862(1)	1.025(3) / 1.026(2)	1.005(4)
C–N(CH$_3$) [a]	1.324(5) / 1.332(5)	1.320(3) / 1.330(3)	1.331(2) / 1.339(3)	1.347 / 1.357	—
N–CH$_3$ [a]	1.457(5) / 1.450(6)	1.458(3) / 1.451(4)	1.460(2) / 1.454(2)	1.461(3) / 1.458(1)	—

a – The two values refer to $SSHB_2$ and $SSHB_1$, respectively (see Figure 5.2); b – Values for the intermolecular interactions at 300 K data set are presented in the text above but are repeated for completeness and ease of comparison.

5.3.3. Computational modelling

The results of the geometry optimisation were in good agreement with experiments, showing deviations of less than 2 % for the heavy atom parameters displayed in Table 5.3. There are bigger deviations in the parameters involving hydrogen atom positions (average of 18 %), but this is entirely expected due to the inherent differences of both methods in determining atomic locations (X-ray methods are based on electronic density while neutron diffraction methods and calculations are based on nuclear positioning). For this reason a comparison with parameters derived from neutron diffraction for UPA was performed, even though there are clear structural differences between these systems, and a much closer agreement was found (average deviation of 4 %).

The geometry optimisation calculations were followed by molecular dynamics simulations at 50 and 300 K, much in line with that done for UPA. As the *a*- axis of the unit cell is shorter than the other two, the calculations were performed on a 2x1x1 cell, thereby artificially augmenting the k-point sampling. The time-averaged structures obtained from the MD simulations (which were run in the absence of symmetry constraints, *i.e.* space group *P*1) were concurrent with the $P2_12_12_1$ space group setting obtained from the XRD experiments.[25]

Since proton migration is a subtle phenomenon, analysis of the SSHBs was performed individually for all hydrogen bonds present in the modelled cell (amounting to 24 bonds). After discarding the first 0.15 ps to allow for system equilibration, the O–H···O and respective O–H bond trajectories from the simulations at 50 and 300 K were averaged in accordance with the blocking method.[21, 26] This corrects the standard deviations obtained for correlation within the data set. The final uncertainties quoted are the errors obtained in the standard deviations (that is the standard deviation divided by the square-root of the number of data points). After this process it was found that the interactions between phosphoric acid molecules (PA–PA) did not involve a significant change in the O···O distance as was seen in the X-ray experiments. However, the proton positions along these SSHBs decreased by *ca.* 0.04 Å away from the centre of the bond, but always remained far from the centre. This small change in behaviour is probably symptomatic of an underlying anharmonic potential well, rather than a true migratory effect. As observed

experimentally, the O···O dmUPA H-bonds $SSHB_1$ remain longer than $SSHB_2$ regardless of temperature. There was a marginal decrease in the individual SSHBs with respect to temperature, but the effect was small, amounting to no more than 0.03 Å. Furthermore, no significant variation of the H-atom positions along the SSHBs was found, indicating that proton migration does not occur in this temperature range, as was seen from the experiments. The individual averages for the 24 hydrogen bonds were then averaged to yield one overall $SSHB_1$, $SSHB_2$ and PA–PA value, which are presented in Table 5.4.

Table 5.4. Comparison of the computed time-averaged SSHBs parameters (distances in Å) as obtained from the molecular dynamics simulations.

Bond type	MD (300K)		MD (50K)	
	r O···O	*r* (P)O–H	*r* O···O	*r* (P)O–H
$SSHB_1$	2.449(3)	1.164(6)	2.430(2)	1.156(2)
$SSHB_2$	2.444(4)	1.157(5)	2.414(1)	1.166(3)
PA–PA	2.497(5)	1.096(5)	2.501(2)	1.054(1)

To investigate further the possibility of proton migration, potential energy surfaces (PESs) were calculated. These were based on the equilibrium geometries, whereby the H atoms were shifted from the donor (phosphoric acid) to the acceptor in set increments. The calculations were performed for the three sets of independent SSHBs and were done both: (i) maintaining the crystal geometry and (ii) extracting a dimer and relaxing it to obtain the gas-phase optimised geometry (see Figure 5.5). The reason for calculating both the crystal- and the gas-phase surfaces was due to the fact that for UPA these vary dramatically: in the gas the minimum energy structure positioned the proton on the side of the acid and in the crystal it was shifted to the base. This highlights that the SSHB PES in UPA is very sensitive to the intermolecular interactions and is thought to lie at the heart of the reason why proton migration can occur in UPA.[27]

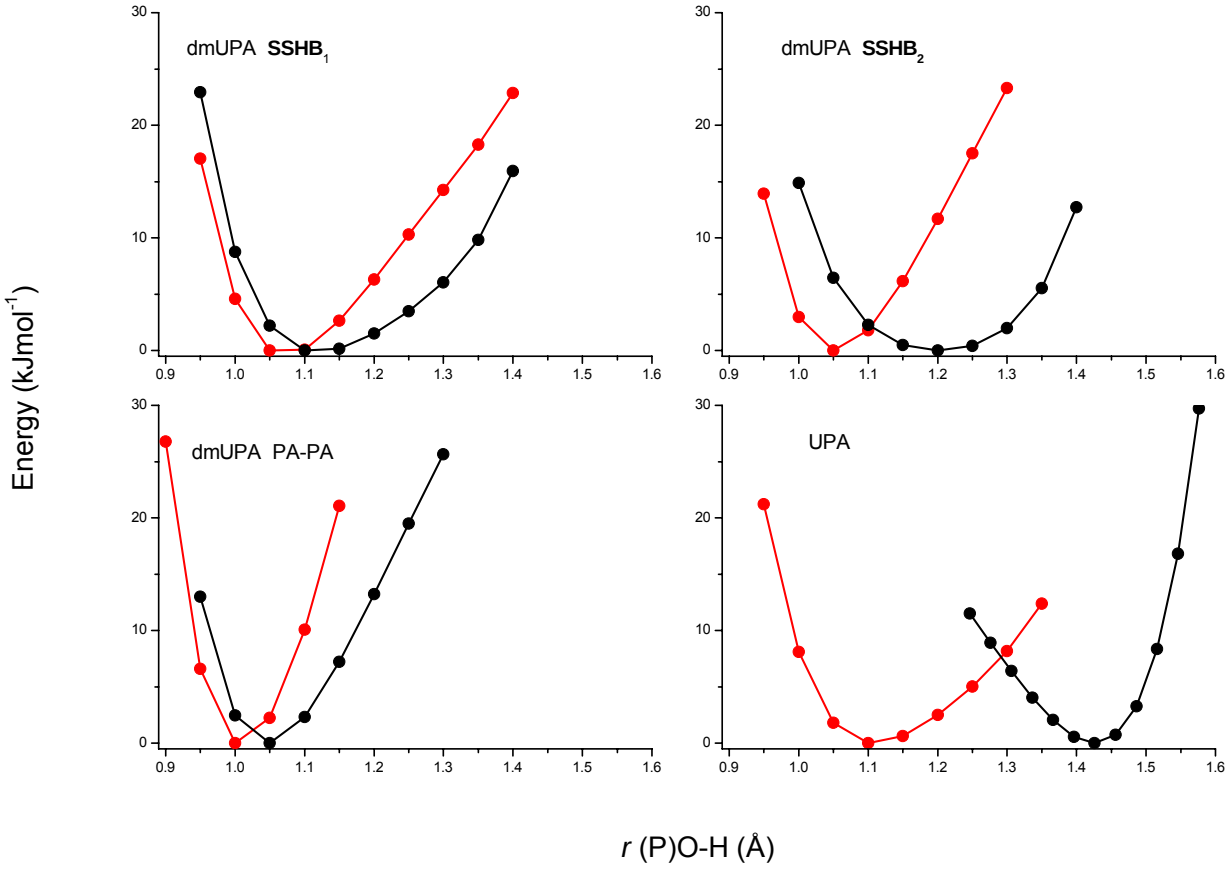

Figure 5.5. Graphs of the dmUPA and UPA PESs calculated by varying the H-atom positions along their respective SSHBs present in the unit cell. The black lines represent the crystal structure surface and the red lines the gas-phase surface.

The PESs obtained for $SSHB_1$ and $SSHB_2$ in dmUPA look quite different from those obtained for UPA, in that the minima are located closer to phosphoric acid for both the crystalline and gas-phase configurations. These become more centred, and symmetric, when going from the gas- to the solid-state, which could be attributed to packing effects. This is most striking in the case of $SSHB_2$, where the PES was found to be almost exactly centred, as also shown from the quantum expectation values of the O–H bond lengths (see Table 5.5). Nevertheless, the variation of bond length is still much less than that observed for UPA, where the solid-state PES places the minimum firmly on the side of urea. It would therefore appear that the PESs for dmUPA are less sensitive to change with respect to external conditions, when compared to UPA. Thus the calculated PESs, along with the MD simulations suggest that dmUPA will not exhibit proton migration. This in turn raises very important points regarding the phenomenon of proton migration. Two things have changed between UPA and dmUPA: the electronic effects of the base and crystal packing arrangement. This begs the question: which is responsible for "switching off" proton migration?

Table 5.5. Comparison of *r*(P)O–H quantum mechanical expectation values (Å) obtained from the equilibrium structures of UPA and dmUPA in the gas and solid states.[21]

	***r* (P)O–H**	
	gas	**crystal**
UPA	1.143	1.287
dmUPA $SSHB_1$	1.130	1.173
dmUPA $SSHB_2$	1.097	1.206

In an attempt to answer this important question, theoretical modelling was pursued still further. This involved manipulating both the UPA and dmUPA structures in order to obtain dmUPA and UPA mimic structures, respectively. In essence, this involved simply replacing the CH_3 groups for H in the dmUPA crystal structure, and the inverse for the UPA crystal structure. Thus a model was obtained for dmUPA locked in the UPA crystal lattice, and *vice versa*. This should determine whether it is the change in electronic effects or crystal packing that is the main influence on the underlying potential energy surfaces.

The resulting PESs obtained for the two mimic structures are given in Figure 5.6. They show very clearly that altering the electronic properties of the base does little to change the potential, which is itself a fascinating result. The implication is that taking the urea-phosphoric acid adduct and altering the crystal lattice from a 1:1 to a 2:1 packing arrangement completely changes the SSHB potential energy surface. The proton, rather than resting on the urea, now sits on the phosphoric acid. The proton migration effect for UPA would vanish. Similarly, changing the packing arrangement for the dimethylurea adduct from 2:1 to 1:1 shifts the proton from the acid side to the base. Proton migration for dmUPA may now be a possibility. This result therefore points strongly towards the crystal packing arrangement being a key factor in controlling the proton migration effect.

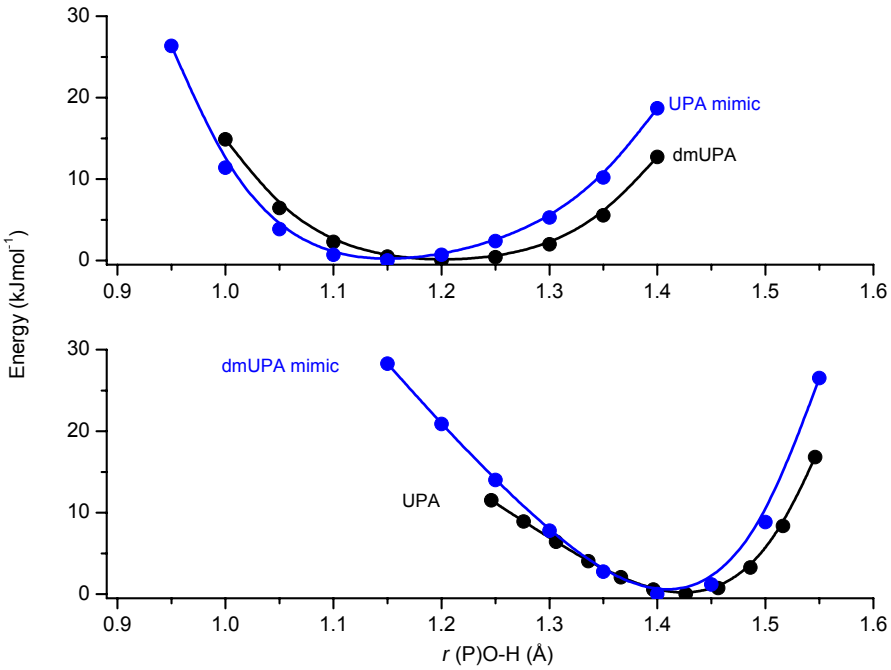

Figure 5.6. Graphs of the dmUPA and UPA crystalline PESs calculated for the H-atom position along the SSHBs of interest. The black lines represent the crystal structure surface and the blue lines represent the mimic structures.

5.4. Conclusions

Gas-phase calculations on UPA and dmUPA dimers showed that the precursors interact more strongly for the case of the latter adduct and indicate to the possibility of proton migration occurring.

Variable temperature single-crystal X-ray diffraction experiments were performed on crystals resulting from the co-crystallisation of N,N-dimethylurea with phosphoric acid. The structure obtained revealed that a 2:1 adduct was preferentially crystallised and that similarly to the parent compound (UPA) SSHBs between the precursors were maintained. However, unlike in the case of UPA proton migration was not observed in the temperature range studied (300–110 K). Despite dimethylurea being more basic than urea, the protons were found to remain on the phosphoric acid even at the lowest temperature. It was postulated that this comes from the fact that there are two molecules of dimethylurea per molecule of phosphoric acid in this system, thereby reducing the effective acidity of phosphoric acid.

Molecular dynamics simulations also show no evidence of proton migration in the temperature range studied, and a comparison of the PESs calculated for the SSHBs present in dmUPA and UPA also supports this finding. Furthermore, manipulating the two crystal structures computationally, such that the two different packing arrangements were experienced by both adducts, pointed strongly towards the change in crystal packing as the reason why proton migration was suppressed in dmUPA.

It would be of great interest to study this adduct under the influence of pressure as it might shorten the assisting N···O hydrogen bonds and consequently lead the P=O to become more involved in hydrogen-bonding. In effect the hydrogen atoms along the SSHBs would become more labile which could conceivably be translated in proton migration. Future work would also involve attempts to prepare the 1:1 adduct of dimethylurea and phosphoric acid, which should exhibit proton migration. Conversely, if the 2:1 adduct of urea and phosphoric acid were to be prepared, it seems likely that temperature-induced proton migration would not occur.

5.5. Bibliography

[1] C. C. Wilson, *Acta Cryst. B* **2001**, *57*, 435.

[2] C. C. Wilson, C. A. Morrison, *Chem. Phys. Lett.* **2002**, *362*, 85.

[3] C. A. Morrison, M. M. Siddick, P. J. Camp, C. C. Wilson, *J. Am. Chem. Soc.* **2005**, *127*, 4042.

[4] C. R. Pulham, C. Spanswick, D. S. Middlemiss, C. A. Morrison, R. M. Ibberson, K. S. Knight, *To be submitted*.

[5] SAINT Area-Detector Software Package v7.01A, Bruker - AXS, Madison, Wisconsin, USA, **2003**.

[6] G. M. Sheldrick, SADABS v2.04, University of Gottigen, Germany, **2001**.

[7] A. Altomare, G. Cascarano, C. Giacovazzo, A. Guagliardi, *J. Appl. Cryst.* **1993**, *26*, 343.

[8] D. J. Watkin, C. K. Prout, J. R. Carruthers, P. W. Betteridge, R. I. Cooper, CRYSTALS v12 ed., Chemical Crystallography Laboratory, Oxford, UK, **2003**.

[9] M. J. Frisch, G. W. Trucks, H. B. Schlegel, G. E. Scuseria, M. A. Robb, J. R. Cheeseman, V. G. Zakrzewski, J. A. M. Jr., R. E. Stratmann, J. C. Burant, S. Dapprich, J. M. Millam, A. D. Daniels, K. N. Kudin, M. C. Strain, O. Farkas, J. Tomasi, V. Barone, M. Cossi, R. Cammi, B. Mennucci, C. Pomelli, C. Adamo, S. Clifford, J. Ochterski, G. A. Petersson, P. Y. Ayala, Q. Cui, K. Morokuma, D. K. Malick, A. D. Rabuck, K. Raghavachari, J. B. Foresman, J. Cioslowski, J. V. Ortiz, A. G. Baboul, B. B. Stefanov, G. Liu, A. Liashenko, P. Piskorz, I. Komaromi, R. Gomperts, R. L. Martin, D. J. Fox, T. Keith, M. A. Al-Laham, C. Y. Peng, A. Nanayakkara, C. Gonzalez, M. Challacombe, P. M. W. Gill, B. Johnson, W. Chen, M. W. Wong, J. L. Andres, C. Gonzalez, M. Head-Gordon, E. S. Replogle, J. A. Pople, Gaussian 98, Revision A.7 ed., Gaussian Inc, Pittsburgh, PA, **1998**.

[10] M. S. Gordon, *Chem. Phys. Lett.* **1980**, *76*, 163.

[11] P. C. Hariharan, J. A. Pople, *Theor. Chim. Acta* **1973**, *28*, 213.

[12] W. J. Hehre, R. Ditchfield, J. A. Pople, *J. Chem. Phys.* **1972**, *56*, 2257.

[13] A. D. Becke, *J. Chem. Phys.* **1993**, *98*, 5648.

[14] C. Lee, W. Yang, R. G. Parr, *Phys. Rev. B* **1988**, *37*, 785.

[15] B. Miehlich, A. Savin, H. Stoll, H. Preuss, *Chem. Phys. Lett.* **1989**, *157*, 200.

[16] *CPMD version 3.11.1*, *Copyright IBM Corp. 1990-2006, Copyright MPI für estkörperforschung Stuttgart 1997-2001*.

[17] J. P. Perdew, K. Burke, M. Ernzerhof, *Phys. Rev. Lett.* **1997**, *78*, 1396.

[18] J. P. Perdew, K. Burke, M. Ernzerhof, *Phys. Rev. Lett.* **1996**, *77*, 3865.

[19] S. Nose, *J. Chem. Phys.* **1984**, *81*, 511.

[20] W. G. Hoover, *Phys. Rev. A* **1985**, *31*, 1695.

[21] C. A. Morrison, School of Chemistry and EaSTCHEM Research School, The University of Edinburgh, UK, Personal communication, **2007**.

[22] D. S. Middlemiss, Department of Chemistry and WestCHEM Research School, University of Glasgow, UK, Personal communication, **2007**.

[23] K. B. Wiberg, P. R. Rablen, *J. Comput. Chem.* **1993**, *14*, 1504.

[24] C. C. Wilson, K. Shankland, N. Shankland, *Z. Kristallogr.* **2001**, *216*, 303.

[25] A. M. Reilly, School of Chemistry and EaSTCHEM Research School, The University of Edinburgh, UK, Personal communication, **2008**.

[26] H. Flyvbjerg, H. G. Petersen, *J. Chem. Phys.* **1989**, *91*, 461.

[27] C. A. Morrison, D. S. Middlemiss, C. R. Pulham, *to be submitted*.

CHAPTER 6

Exploratory systems *en route* to engineer short, strong hydrogen bonds and proton migration

6.1. General introduction

Crystal engineering is an attractive area of research for chemists of many backgrounds.[1] It tries to rationalise and mimic what nature has perfected. In order to do so, supramolecular chemists had to distance themselves from the ideas of functional group complementarities and correlation, to a topological level where the simple relationships only dominate when interference from opposing sets of interactions are minimal.[2] For this reason non-covalent interactions, in particular hydrogen bonds and van der Waals forces, play a central role in crystal packing motifs and crystal engineering. Many studies have therefore centered around hydrogen-bonded molecular complexes. Such interactions are quite flexible and can lead to a variety of structural arrangements with small energetic differences, *i.e.* polymorphs.

This chapter documents the studies of compounds that for one reason or another did not result in the expected structures. All experiments were designed to create hydrogen-bonded adducts with short, strong hydrogen bonds (SSHBs) in order to study their potential ability for proton migration. Some of them, however, ended up reacting to create new compounds while others led to longer than intended hydrogen bonds or gave rise to new polymorphs.

6.2. Attempted co-crystallisation of methyl-substituted ureas and squaric acid

6.2.1. Introduction

Squaric acid (SQ) has been previously suggested to possess similar chemical behaviour to phosphoric acid on the basis of exhibiting similar charge distribution (see Figure 6.1).[3]

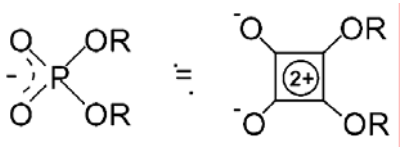

Figure 6.1. Diagram demonstrating the structural similarity of squaric acid and phosphoric acid derivatives.[3]

Co-crystallisation of SQ with various methyl-substituted urea derivatives was therefore undertaken in order to tap into a large potential of new compounds based on urea-phosphoric acid, and therefore attempt to engineer new materials that will exhibit the proton migration effect. All attempts along this route led to structures where the ureas fused with the SQ ring through a condensation reaction, forming vinylogous dicarboxylic acid derivatives (see Figure 6.2).[4, 5] There are several reports of these types of compounds in the literature and they have been implicated in physiological activity.[6, 7] The most pertinent are those synthesised by Li *et al.*,[6-9] which are N-(2-hydroxycyclobutene-3,4-dione)-urea, N-(2-hydroxycyclobutene-3,4-dione)-N'-methylurea and N-(2-hydroxycyclobutene-3,4-dione)-N'-ethylurea. It should be noted that all of these compounds were characterised in solution.

In the present work the N,N-dimethyl and N,N'-dimethyl analogues of the structures studied by Li *et al.* have been crystallised and are the focus of this subchapter.

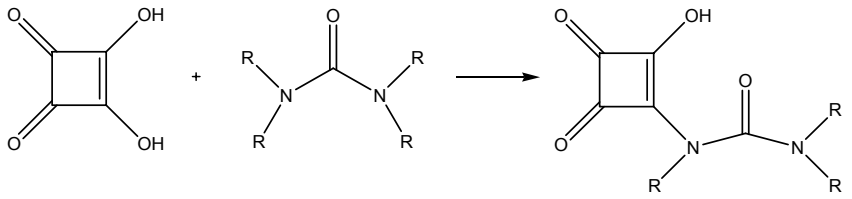

Figure 6.2 Formation of vinylogous dicarboxilic acid derivatives, where R represents H or CH_3 groups.

6.2.2. Experimental section

6.2.2.1 Materials

Squaric acid (SQ), N,N-dimethylurea (1,1-dmU) and N,N'-dimethylurea (1,3-dmU) were obtained from Sigma-Aldrich and used without further purification. Crystallisation of two derivatives [N-(2-hydroxycyclobutene-3,4-dione)-N',N'-dimethylurea (hereafter labelled **I**) and N-(2-hydroxycyclobutene-3,4-dione)-N,N'-dimethylurea (hereafter labelled **II**)] were obtained by combining equimolar quantities of both precursors [0.076 g (0.863 mmol) of 1,1-dmU with 0.095 g (0.833 mmol) of SQ, and 0.072 g (0.817 mmol) of 1,3-dmU with 0.107 g (0.938 mmol) of SQ; respectively] in the minimum amount of water that allowed for dissolution (~ 3 cm^3). The mixtures were then allowed to evaporate slowly until crystal formation was complete, which was observed after 5 days. This resulted in the crystallisation of colourless blocks in the case of **I** and colourless needles in the case of **II**.

6.2.2.2. Single-crystal X-ray diffraction

Studies of **I** were performed using a Bruker-Smart Apex CCD diffractometer equipped with an Oxford Cryosystems low temperature device at 100 K. For **II** analysis was undertaken using a Bruker-Nonius APEX 2 CCD diffractometer operating at room temperature. In both cases Mo-Kα radiation (λ = 0.71073 Å) was employed, and data reduction was performed using *SAINT* (Bruker Nonius).[10] Absorption corrections were applied using the multiscan procedure program *SADABS*.[11] Structures were solved by direct methods using the *SIR92*[12] package, and refined using full-matrix least squares against $|F|^2$ using *CRYSTALS*.[13] The non-hydrogen atoms were refined with anisotropic thermal parameters. Hydrogen atoms were, unless explicitly stated, placed geometrically and allowed to regularise with respect to Fourier difference peaks. It should be noted that for **II**, H(101) was restrained to have a similar COH angle as found in the structure of **I**.

Table 6.1. Crystal details of **I** and **II**.

	I	**II**
Chemical formula	$C_7H_8N_2O_4$	$C_7H_8N_2O_4$
M_r (g mol^{-1})	184.15	184.15
Crystal system, space group	triclinic, *P*-1	monoclinic, $P2_1/m$
Temperature (K)	100	293
a *b* *c* (Å)	9.2687(3) 9.3177(3) 10.7398(4)	7.1607(14) 6.3183(13) 8.5926(17)
α β γ (°)	79.600(2) 88.313(2) 61.938(2)	90 93.38(3) 90
V (Å^3)	803.39(5)	388.08(13)
Z	4	2
ρ_{calc} (g cm^{-3})	1.52	1.58
Radiation type	Mo *K*α	Mo *K*α
Crystal form, colour	Block, colourless	Needle, colourless
Crystal size (mm)	0.20 x 0.20 x 0.33	0.15 x 0.18 x 0.25

6.2.3. Experimental section

6.2.3.1. N-(2-hydroxycyclobutene-3,4-dione)-N',N'-dimethylurea

I crystallises with two molecules in general positions within the asymmetric unit as shown in Figure 6.3 (space group *P*-1). This leads to a unit cell (see Table 6.1) comprising four molecules that lie on the (130) planes.

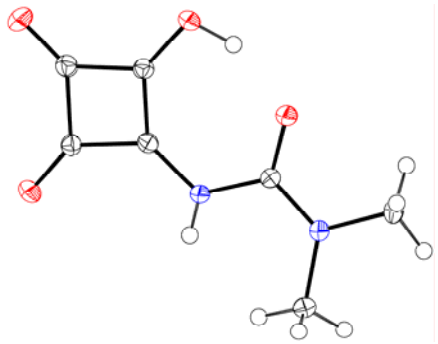

Figure 6.3. Half of the asymmetric unit cell of **I**. Displacement ellipsoids are drawn at the 50 % probability level.

The most interesting feature of this compound is the short intramolecular O–H···O bond (2.58 Å) that form an $S(7)$ graph-set (see circled motif in Figure 6.4). Molecules are connected in dimers through two N–H···O hydrogen bonds (2.84 Å), represented by a $R_2^2(10)$ ring (see rectangle in Figure 6.4).

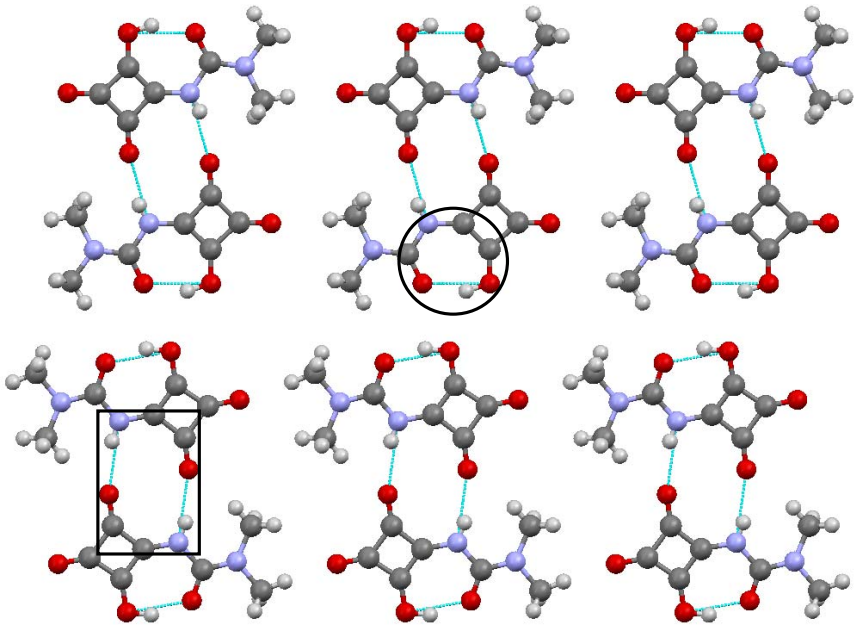

Figure 6.4. The crystal structure of **I** viewed along the *b*- axis.

The two intermolecular patterns can also be described as forming planar chains along the *a*- axis, that have close contacts between them (CH···O 2.44 Å; note the sum of the van der Waals radii of H and O is 2.72 Å). Furthermore these planes are separated by *ca.* 3.1 Å (see Figure 6.5).

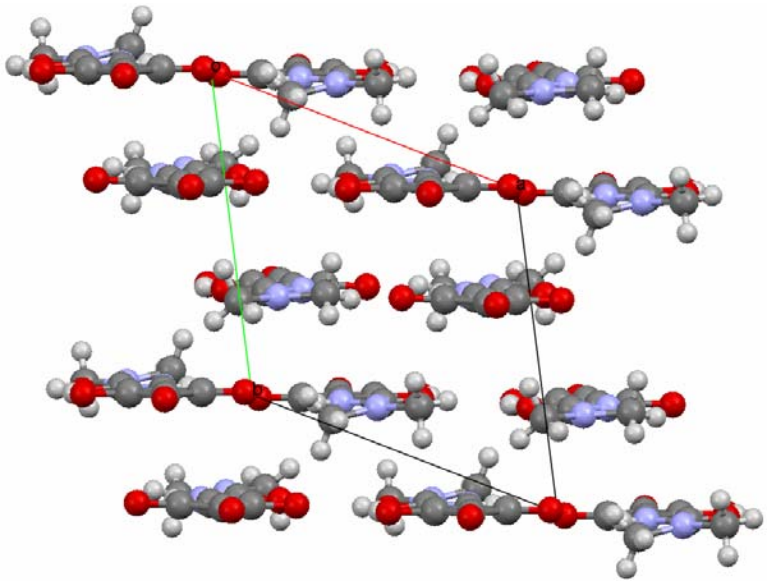

Figure 6.5. Structure of **I** viewed along the *c*- axis of the *ab* plane.

6.2.3.2. N-(2-hydroxycyclobutene-3,4-dione)-N,N'-dimethylurea

The asymmetric unit of **II** contains one molecule in a general position as shown in Figure 6.6 (space group $P2_1/m$). In the unit cell (see Table 6.1) there are two molecules that lie on the (040) planes, related by a centre of inversion positioned in the centre of the unit cell.

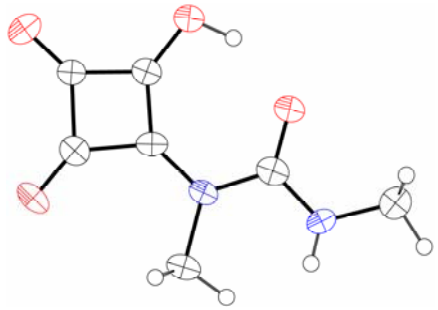

Figure 6.6. The asymmetric unit cell of **II**. Displacement ellipsoids are drawn at the 50 % probability level.

In common with the previous structure this compound also has a $S(7)$ graph-set moiety, with a short intramolecular O–H···O bond of length 2.59 Å. The intermolecular H-bond network for this compound is quite different, however, as it

has a $C(8)$ chain that spreads across the (040) plane in the direction of the *c*- axis (see Figure 6.7) arising from N–H···O bonds (3.04 Å). These chains in turn are held together by close contacts between OH···O atoms (2.28 Å; the sum of the van der Waals radii of O and H is 2.72 Å). These layers cut the *b*- axis at ¼ and ¾, leading to an interlayer distance that is slightly longer than that of **I** (3.16 Å, see Figure 6.8). This increase may also be related to the fact that the data collection was performed at higher temperature.

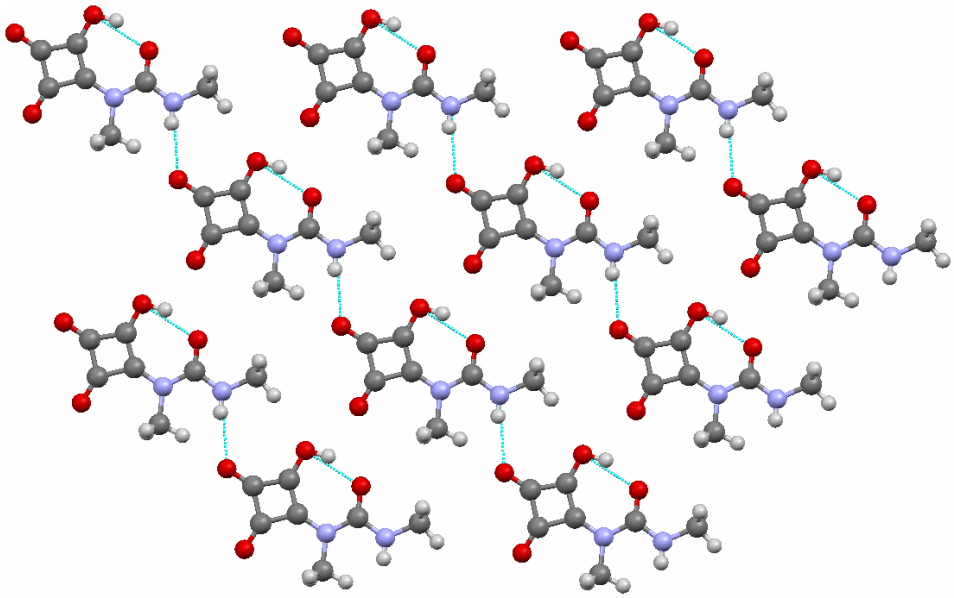

Figure 6.7. The crystal structure of **II** viewed along the *b*- axis.

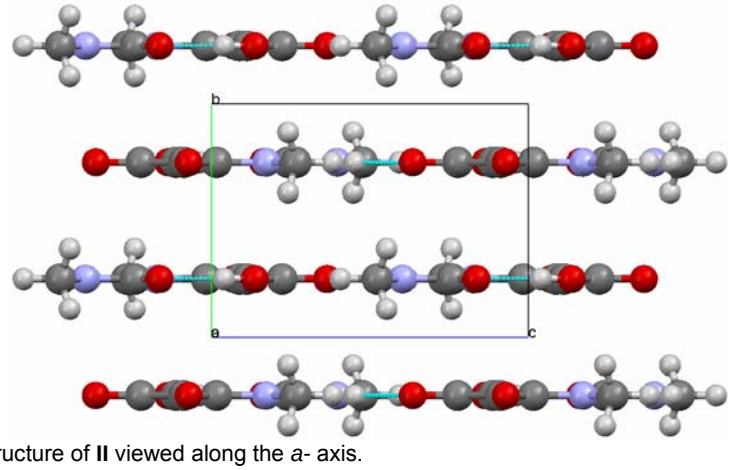

Figure 6.8. Structure of **II** viewed along the *a*- axis.

6.3. The 1:2 dihydrate of 2,2'-dimethyl-4,4'-bipyridine with oxalic acid

6.3.1. Introduction

Co-crystals of carboxylic acids and pyridine-containing compounds have yielded interesting systems linked to temperature induced proton migration and transfer.[14-18] The example most pertinent to the present work is that of the 1:1 adduct of bipyridine (BIPY) and oxalic acid, recently studied by Cowan *et al.*[19] In this system the components were linked together by three similar O–H···N short hydrogen bonds, *ca.* 2.6 Å. This, linked to the fact that O–H distances have been found by neutron diffraction data to become significantly elongated when O···N hydrogen bonds are shorter that 2.6 Å,[20] led the authors to postulate about the possibility of proton migration.

The rationale behind the choice of adduct in these experiments was to study the effect of using precursors that possess both higher acid and base characters than the ones used in the co-crystallisation of squaric acid and bipyridine (SQBP – see Chapter 3). The obvious choices were dimethyl bipyridine (dmBIPY with pKas of the conjugated acids of approximately 3.5 and 5.6),[21][22] together with oxalic acid (pK_{a1}=1.3 and pK_{a2}=4.3).[23, 24] It was anticipated that this would lead to a similar structure to SQBP, and the adduct between oxalic acid and BIPY, but hopefully with only one independent shorter and stronger H-bond. Although the co-crystallisation design did not follow the intended path (as water was incorporated in the crystal lattice), it did yield a new structure (2,2'-dimethyl-4,4'-bipyridine-oxalic acid-water, in ratio 1:2:2), which will be addressed below.

6.3.2. Experimental section

6.3.2.1. Materials

Oxalic acid and 2,2'-dimethyl-4,4'-bipyridyl (dmBIPY) were obtained from Sigma-Aldrich and Fluorochem, respectively, and were used without further purification. Crystallisation of the hydrate (labelled OXAdmBP) was obtained by

combining equimolar quantities of both adducts [0.095 g (0.516 mmol) of the base with 0.049 g (0.544 mmol) of the acid] in *ca*. 6 cm^3 of water. The mixture was then allowed to evaporate slowly until crystal formation was complete, which was observed after 3 days. This resulted in the crystallisation of colourless blocks.

6.3.2.2. Single-crystal X-ray diffraction

Studies of OXAdmBP were performed using a Bruker-Smart Apex CCD diffractometer, equipped with an Oxford Cryosystems low temperature device, at 115 K using Mo-Kα radiation (λ = 0.71073 Å). The data reduction process was performed using *SAINT* (Bruker Nonius).[10] An absorption correction was applied using the multiscan procedure program *SADABS*.[11] Structures were solved by direct methods using the *SIR92*[12] package, and refined using full-matrix least squares against $|F|^2$ using *CRYSTALS*.[13] The non-hydrogen atoms were refined with anisotropic thermal parameters. Hydrogen atoms were, unless explicitly stated, placed geometrically and allowed to regularise with respect to Fourier difference peaks.

Table 6.2. Crystal details of OXAdmBP.

	OXAdmBP
Chemical formula	$C_8H_{10}N_1O_{20}$
M_r (g mol^{-1})	200.17
Crystal system, space group	triclinic, *P*-1
Temperature (K)	115
a *b* *c* (Å)	6.7954(3) 6.9567(3) 9.3200(4)
α β γ (°)	99.533(3) 98.176(3) 90.522(3)
V ($Å^3$)	429.85(3)
Z	1
ρ_{calc} (g cm^{-3})	1.55
Radiation type	Mo *K*α
Crystal form, colour	Block, colourless
Crystal size (mm)	0.16 x 0.39 x 0.39

6.3.3. Results and discussion

The asymmetric unit of OXAdmBP (see Figure 6.9) consists of one oxalic acid molecule and one water molecule in general positions, together with half a molecule of dmBIPY that lies on a centre of inversion. As a consequence, the unit cell (space group *P*-1 as shown in Table 6.2) has two molecules of oxalic acid and water, and one of dmBIPY.

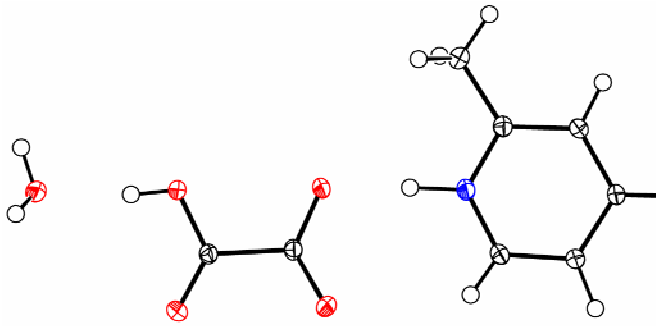

Figure 6.9. Asymmetric unit cell of OXAdmBP. Displacement ellipsoids are drawn at the 50 % probability level.

The primary hydrogen-bonding motif in the structure is a $R_4^4(14)$ ring, formed by opposing oxalic acid and water molecules that have O–H···O distances of 2.58 and 2.81 Å. The formation of these rings are presumably due to the bulky CH_3 groups attached to the BIPY molecules. The rings are, in turn, interconnected by a hydrogen bond to dmBIPY (N–H···O of 2.64 Å), giving rise to step-like chains along the (24-2) plane (see Figure 6.10).

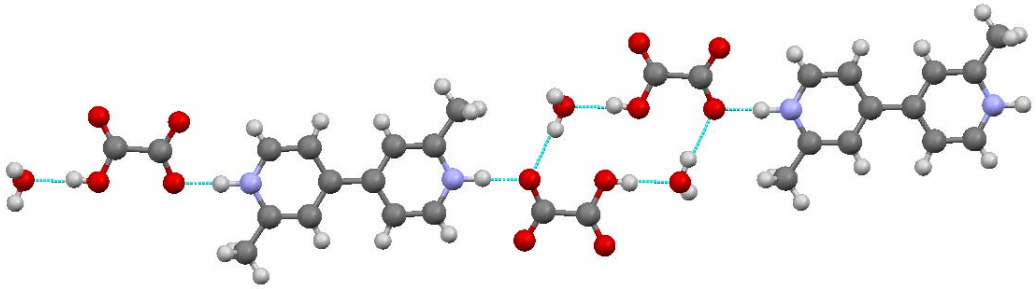

Figure 6.10. OXAdmBP viewed perpendicular to the (24-2) plane.

Perpendicular to the (24-2) planes are alternating layers that are separated by *ca.* 3.2 Å. These appear staggered throughout the aforementioned planes (see Figure 6.11). Links between neighbouring planes are due to O–H···O interactions between water and oxalic acid molecules (2.84 Å; the sum of the van der Waals radii of H and O is 2.72 Å).

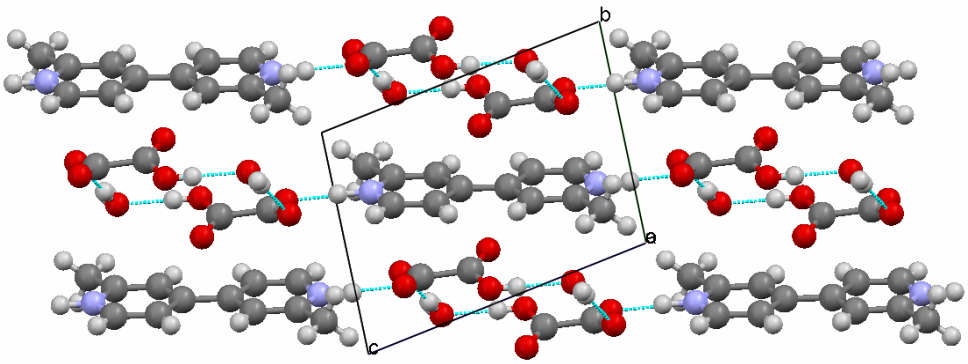

Figure 6.11. OXAdmBP view of the *bc* plane.

6.4. The 1:2 adduct of 4,4'-bipyridine with oxamic acid

6.4.1. Introduction

The oxamate anion has been shown to be an important building block for hydrogen-bonded structures with an inherent tendency towards generating extended, low dimensional, anionic motifs.[25] These are generally held together by at least two N–H···O hydrogen bonds that are permitted due to the complementary functionalities of the $–COO^-$ and $–CONH_2$ groups. The dimensionality and the precise topology of the anionic assemblies are to some extent dependent on the cation[25]. Nevertheless the predictability and flexibility of these anionic assemblies can be advantageous, since they generally allow the creation of either 1-D or 2-D infinite networks which, in turn, affect properties such as structural rigidity.

Oxamic acid is a monoprotic acid ($pK_a \sim 2.5$)[22] that is slightly weaker than that used in the preparation of SQBP (see Chapter 3). In this work it was co-crystallised with BIPY in order to pursue a systematic route, because only in such a fashion is it possible to attempt rationalisation of proton migration in systems with

SSHBs. The structure of the titled adduct will be the focus of the remaining subchapter.

6.4.2. Experimental section

6.4.2.1. Materials

Oxamic acid and 4,4'-bipyridine (BIPY) were obtained from Sigma-Aldrich and used without further purification. Crystallisation of the adduct (OMABP) was obtained by combining equimolar quantities of both adducts [0.18 g (1.153 mmol) of the base with 0.11 g (1.235 mmol) of the acid] in *ca*. 8 cm^3 of water. The mixture was then allowed to evaporate slowly until crystal formation was complete, which was observed after 10 days. This resulted in the formation of colourless plates.

6.4.2.2 Single-crystal X-ray diffraction

Studies of OMABP were performed using a Bruker-Smart Apex CCD diffractometer equipped with an Oxford Cryosystems low temperature device at 115 K using Mo-Kα radiation (λ = 0.71073 Å). The data reduction process was performed using *SAINT* (Bruker Nonius).[10] An absorption correction was applied using the multiscan procedure program *SADABS*.[11] Structures were solved by direct methods using the *SIR92*[12] package, and refined using full-matrix least squares against $|F|^2$ using *CRYSTALS*.[13] The non-hydrogen atoms were refined with anisotropic thermal parameters. Hydrogen atoms were, unless explicitly stated, placed geometrically and allowed to regularise with respect to Fourier difference peaks.

Table 6.3. Crystal details of OMABP.

	OMABP
Chemical formula	$C_{14}H_{14}N_4O_6$
M_r (g mol^{-1})	334.29
Crystal system, space group	monoclinic, $P2_1/n$
Temperature (K)	115
a *b* *c* (Å)	12.3085(4) 7.0171(3) 16.3435(5)
β (°)	101.040(2)
V (Å^3)	1385.46(9)
Z	4
ρ_{calc} (g cm^{-3})	1.60
Radiation type	Mo *K*α
Crystal form, colour	Plate, colourless
Crystal size (mm)	0.10 x 0.20 x 0.20

6.4.3. Results and discussion

The asymmetric unit of OMABP (see Figure 6.12) comprises of two oxamic acid molecules and one BIPY molecule in general positions (space group $P2_1/n$). This led to a unit cell (see Table 6.3) with three BIPY molecules and six oxamic acid molecules that zigzag along the (040) planes (see Figure 6.13).

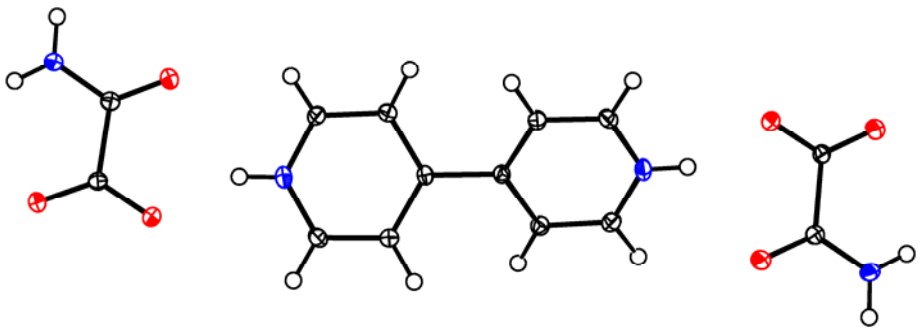

Figure 6.12. Asymmetric unit cell of OMABP. Displacement ellipsoids are drawn at the 50 % probability level.

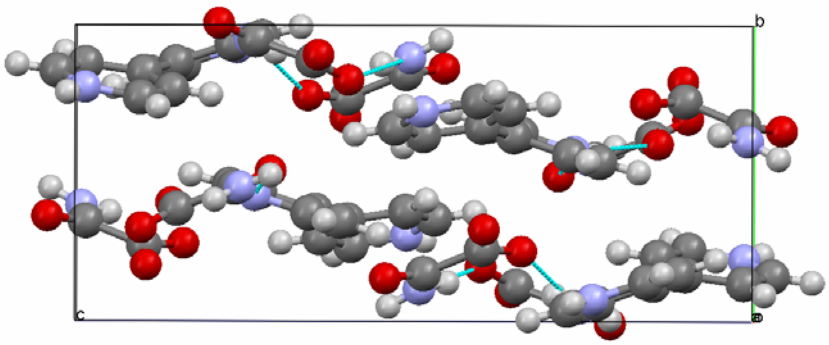

Figure 6.13. OMABP view of the *bc* plane.

The main packing moiety are the $C_3^3(18)$ ribbons that spawn from the asymmetric unit and grow in the direction of the (-103) plane. Encapsulated in these ribbons are $R_2^1(6)$ rings between BIPY and oxamic molecules that arise from a bifurcated H-bond (N–H···O distances are 2.56 and 2.87 Å), and $R_2^2(10)$ rings linking oxamic acid molecules through O–H···O hydrogen bonds that are 2.84 and 2.91 Å long (see Figure 6.14). These neighbouring chains are connected through close contacts between the oxamic molecules closest to the BIPY molecules (NH···O interactions of length 2.07 Å), creating a 2-D scaffolding.

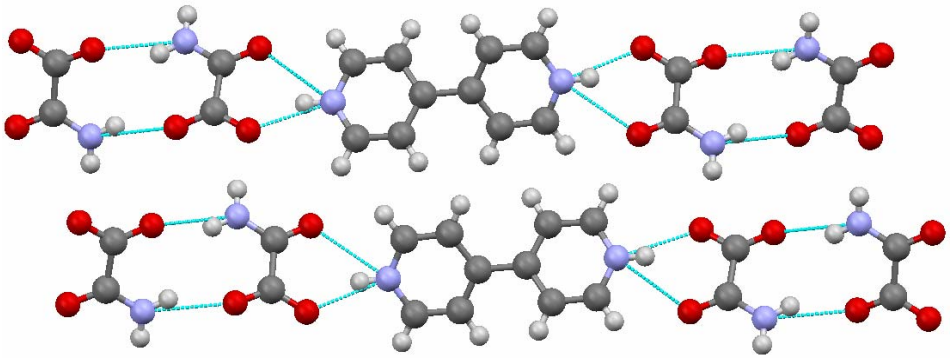

Figure 6.14. OMABP view along the *b*- axis.

6.5. A new polymorph of N,N'-dimethylurea

6.5.1. Introduction

Compounds based on urea possess the ability to form a diverse range of hydrogen-bonded networks and constitute an important series of precursors in crystal engineering applications.[26-30] Urea in form I presents a structure in which each molecule donates two hydrogen bonds to the carbonyl group of a neighbouring unit, forming one-dimensional chains with an intermolecular distance of approximately 4.7 Å.[31] Neighbouring chains alternate in the direction of orientation of their respective C=O bonds, and as a consequence the lattice is non-polar. Symmetrically disubstituted ureas tend to adopt the same characteristic packing motif, albeit with a shorter intermolecular distance of *ca.* 4.6 Å [Figure 6.15(a)].[27, 28, 32-35]

N,N'-dimethylurea (1,3-dmU), one of the simplest examples of a disubstituted urea, has been shown to be of relevance within a wide variety of scientific and industrial applications (*e.g.* in membrane transport within red blood cells and as a stabiliser of hydrated lubricating oils).[36-39] The first account of the determination of the crystal structure dates back to 1924,[40] although it should be noted that this study is not entered in the Cambridge Structural Database (CSD).[41] Pérez-Folch *et al.* are, however, generally credited with the first crystallisation of 1,3-dmU in 1997, with a structural refinement assigned to the *Cc* space group.[42] This result was unexpected, as it indicated a polar structure in contrast with that of the parent compound urea [Figure 6.15(b)]. It is worth noting that the authors also attempted a refinement in the *Fdd*2 space group, but dismissed it on the basis of the larger thermal parameters and higher *R*-factors obtained. Various crystallisation techniques were also applied in an effort to obtain a polymorph with packing more akin to that observed for urea, but these were unsuccessful, in spite of the fact that different crystallisation conditions could account for the different structures.[42] In fact, the crystalline symmetry of 1,3-dmU was subsequently reassigned to the orthorhombic *Fdd*2 space group by Marsh[43] during a survey of the CSD.

In a later study by Keuleers *et al.*[44] the solid-state vibrational spectra was computed for form I within the erroneous *Cc* space group, in which the normal modes of a cluster of 15 molecules surrounded by 6048 point charges were obtained

at the RHF/6-31++G** level. The vibrational frequencies thus obtained were subsequently transformed into a symmetry coordinate force field and then scaled against and compared with the experimental data.[44]

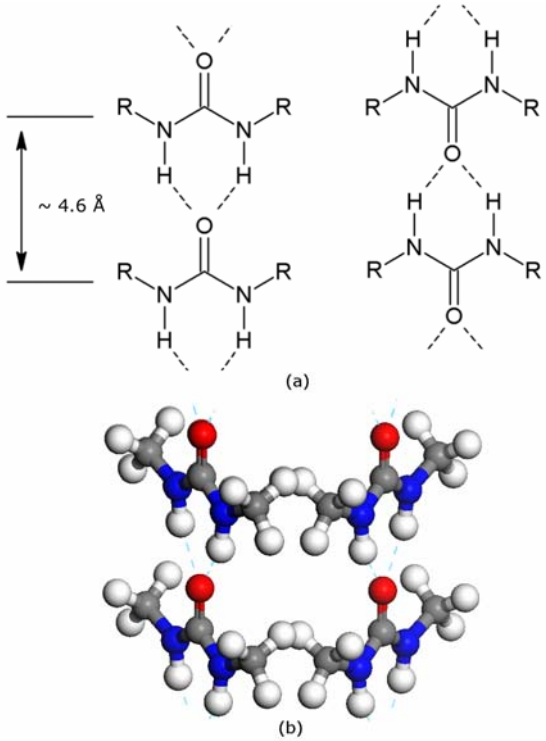

Figure 6.15. (a) Motif of symmetrical disubstituted ureas and (b) portion of the polar 1,3-dmU structure[43].

The structure of a new polymorph of 1,3-dmU (hereafter labelled form II), along with the results of theoretical calculations that were performed to obtain the relative energies of the two polymorphs and to analyse the differences in the solid-state vibrational spectra, will be presented below.

6.5.2. Experimental section

6.5.2.1. Materials

1,3-dmU and phosphoric acid were obtained from Sigma-Aldrich and used without further purification. The new polymorph of 1,3-dmU was first obtained when attempting co-crystallisation of 1,3-dmU with phosphoric acid [0.443 g (5.038 mmol) and 0.491 g (5.010 mmol), respectively] in *ca.* 5 cm^3 of water by means of slow evaporation until crystal formation occurred, which was observed after a period of 10 months. The new polymorph of 1,3-dmU was then subsequently also found through direct measurement of the commercial sample.

6.5.2.2. Single crystal X-ray crystallography

Studies of the colourless block-shaped crystals were performed using a Bruker-Smart Apex CCD diffractometer equipped with an Oxford Cryosystems low temperature device at 150 K, and a Bruker-Nonius APEX 2 CCD diffractometer at room temperature.[45] Both instruments used a Mo-Kα radiation (λ = 0.71073 Å) source. Data reduction was performed using *SAINT* (Bruker Nonius).[10] An absorption correction was applied using the multiscan procedure program *SADABS*.[11] Structures were solved by direct methods using the *SIR92*[12] package, and refined using full-matrix least squares against $|F|^2$ using *CRYSTALS*.[13] The non-hydrogen atoms were refined with anisotropic thermal parameters. Hydrogen atoms were placed geometrically and allowed to regularise with respect to Fourier difference peaks.

6.5.2.3. Computational modelling

Geometry optimisations and lattice dynamics calculations were performed for both the new polymorph (space group $P2_12_12$) and the previously reported *Fdd*2 crystal form of 1,3-dmU[42, 43] using the *CRYSTAL06* code.[46] The electron-electron interactions were approximated by use of the B3LYP[47, 48] hybrid functional, while the crystalline orbitals were expanded in terms of standard, atom-centred 6–311G** Gaussian basis sets.[49] The SCF total energy convergence tolerance was set at 10^{-9} a.u., while the reciprocal space zone was sampled upon a Monkhorst-Pack mesh with a shrinking factor of 6.[50] Optimisations were pursued to a total energy

convergence of 10^{-9} a.u., with RMS gradient and displacement tolerances of 3×10^{-5} and 1.2×10^{-4} a.u., respectively. The tolerances for individual components of the gradients and displacements were set at 1.5 times the respective RMS criterion.

The solid-state vibrational modes were also obtained from the *CRYSTAL06* code[46] through the use of lattice dynamics calculations within full periodic boundary conditions using the B3LYP hybrid density functional.[47, 48] These have been shown to provide accurate frequencies without recourse to scaling, and at low computational cost.[51-53] For the purposes of comparison with infrared (IR) and Raman spectra, the frequencies were restricted to the Γ- point of reciprocal space, for it is only the phonons with this wavevector that couple to the electromagnetic field of the probe beam. The normal modes of the two lattices were determined from a series of finite displacement calculations, in which the atoms were separately translated 0.003 Å along the Cartesian axes. The point group symmetry of the lattice is used to fill out the force constants matrix, and so only an irreducible set of atomic displacements need to be considered. In the primitive cell of 1,3-dmU, this set comprises shifts in the *x*-, *y*- and *z*-directions of each of the atoms in the irreducible fragment of a single molecule (*i.e.* $CONHCH_3$), amounting to twenty-four displacements in total. The temperature-dependent harmonic free energies of the lattices were then obtained from combination of the set of vibrational frequencies with the appropriate Boltzmann weights in the usual manner. It should be noted, however, that this approach neglects both the dispersion of the optical modes, which is likely to be small in a molecular crystal, and the dispersion of the acoustic modes, which is likely to be more substantial. However, the missing contributions would be expected to largely cancel, in the subtraction from which the difference in free energy of the two forms is obtained, lending support to the simple Γ- point model.[54] It should be noted also that vibrational modes involving hydrogen atoms are prone to significant anharmonicity. This was addressed for the stretching motions by solving a series of one-dimensional Schrödinger equations incorporating potentials derived from 6^{th}-order polynomial fits to total energies obtained at a range of N–H and C–H bond lengths. Two models were utilised for the N–H bonds, which were allowed to either conserve or break the space group symmetry, whereas all the C–H bond

displacements preserved the full lattice symmetry and thereby corresponded to the totally symmetric stretching motion.

6.5.3. Results and discussion

6.5.3.1. Single-crystal X-ray diffraction studies

Two previous publications have described the solid state structure of form I 1,3-dmU.[42, 43] In Figures 6.16 and 6.17 both the geometries of known and the new forms of 1,3-dmU are depicted in various projections. Form I forms a network in which both nitrogen atoms of one molecule are connected to an oxygen atom of the neighbouring molecule through a bifurcated hydrogen bond, forming one-dimensional chains with an intermolecular distance close to 4.6 Å. Neighbouring chains then pack into the lattice with similar orientations, forming a polar structure [see Figure 6.16 (a)]. Form II manifests the same hydrogen-bonded chains extending along the *c*- axis of the unit cell, but in this case the neighbouring chains adopt alternating orientations, forming the non-polar lattice that seems to be characteristic of the symmetrically disubstituted ureas in general, and urea form I itself [Figure 6.16 (b)].

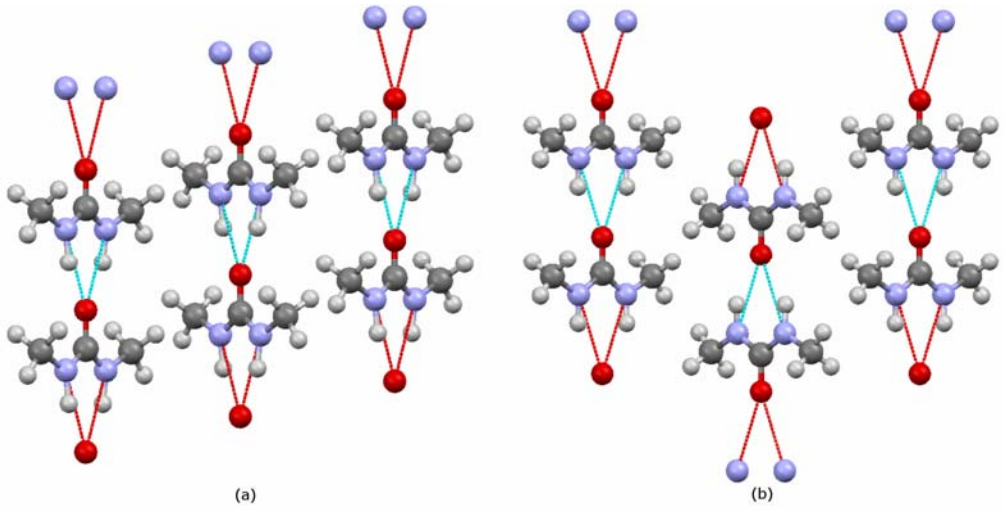

Figure 6.16. Projections of the (a) form I and (b) form II 1,3-dmU structures onto the *ac* planes.

Figure 6.17 demonstrates that the new polymorph maintains the Z,Z-configuration, and makes clear the similarities with the form I urea structure. The angles between the molecular planes of neighbouring chains were 90.0°, 70.2° and 89.6° for urea, form I and form II, respectively. It should be noted, however, that in form I urea the NCN moieties are oriented toward the C=O groups of molecules in the neighbouring chains, whereas in both form I and form II of 1,3-dmU, this moiety points toward the CH_3 groups of the adjacent chains.

The molecules in form II 1,3-dmU pack in a slightly more efficient arrangement which is translated in the density of form II being higher by some 2 % compared to that of form I, when both are at room temperature (see Table 6.4). Furthermore, form II 1,3-dmU also becomes significantly denser (5 %) at low temperature (150 K), which may be attributed to the flexibility along the *a*- axis direction which is largely dominated by van der Waals interactions. The increased density of form II suggests that another way to access it might be *via* crystallisation conducted under pressure. It should be noted, however, that direct compression of form I is unlikely to instigate a transition to the form II structure as this would require the concerted reorientation of 1,3-dmU molecules in every other chain. Considerable success in accessing new denser polymorphs has recently been obtained by *in situ* crystallisation at high pressure from the melt.[55] Initial experiments where new crystals of 1,3-dmU were grown from the melt under ambient pressure have indicated that, rather than causing a phase transition between I and II, a new (third) form may instead be obtained for this compound. Further experiments under pressure are now planned.

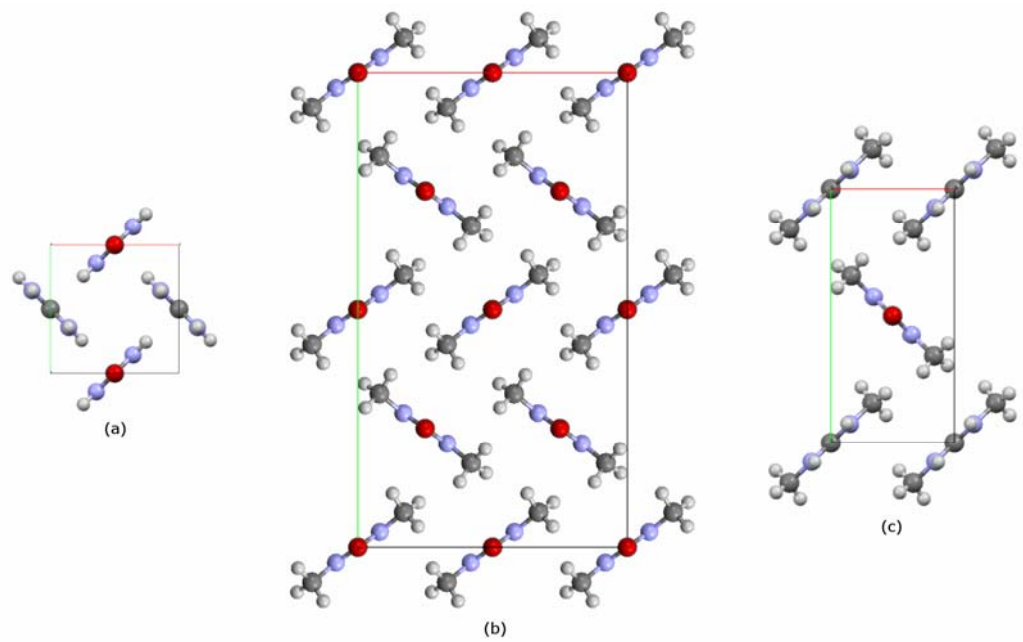

Figure 6.17. Crystal structure of (a) form I urea, (b) form I 1,3-dmU[43] and (c) form II 1,3-dmU projected on the *ab* planes.

Table 6.4. Crystal details of 1,3-dmU forms I and II.

	Form II		**Form I**[43]
Chemical formula	$C_3H_8N_2O$		$C_3H_8N_2O$
M_r (g mol^{-1})	88.11		88.11
Crystal system, space group	orthorhombic, $P2_12_12$		orthorhombic, Fdd_2
Temperature (K)	150	293	293
a *b* *c* (Å)	4.9790(9) 10.775(2) 4.5764(9)	5.2202(15) 10.769(3) 4.5952(14)	11.400(1) 20.186(1) 4.569(1)
V (Å^3)	245.52(8)	258.33(13)	1051.42(2)
Z	2	2	8
ρ_{calc} (g cm^{-3})	1.19	1.13	1.11
Radiation type	Mo *K*α	Mo *K*α	Cu *K*α
Crystal form, colour	Block, colourless	Block, colourless	Needle, colourless
Crystal size (mm)	0.22 x 0.28 x 0.31	0.14 x 0.32 x 0.34	0.16 x 0.16 x 2.01

6.5.3.2. Computational modelling – structure

A comparison of the experimental and calculated geometries for both polymorphs is presented in Table 6.5. Based on these parameters the simulations are, generally, in very good agreement with the X-ray data, having the majority of the experimental structural parameters, to within maximum deviations of 2.5 % and 1.5 % for the form I and form II structures, respectively. More substantial differences do appear for parameters related to hydrogen atom positions (*e.g.* N–H bond length). These arise from a combination of the fact that the calculations were performed in the athermal limit, along with the inherent differences of both methods in determining atomic locations (X-ray methods are based on electronic density while calculations are based on nuclear positioning).

Table 6.5. Relevant solid-state calculated and experimental[43] structural parameters (distances in Å and angles in degrees) for 1,3-dmU form I in the *Fdd*2 crystal form and 1,3-dmU form II space group $P2_12_12$. Note in both these symmetry settings molecules possess localised C_2 symmetry.

Structural parameters	Form I		Form II	
	Expt.	Calc.	Expt.	Calc.
C–O	1.242(4)	1.250	1.231(3)	1.249
C–N	1.329(11)	1.358	1.3428(19)	1.3589
N–CH_3	1.443(11)	1.451	1.432(3)	1.450
N–H	1.080(4)	1.016	0.8925(14)	1.0158
N···O' [a]	2.868(6)	2.841	2.891(2)	2.868
N–C–N	117.1(8)	115.8	116.36(19)	115.98
O–C–N–H	-175.4(9)	-179.9	-178.3(2)	-176.0
C–N–C–H	180.0(8)	163.8	175.0(2)	171.7

a – O' refers to an oxygen atom on a neighbouring molecule.

6.5.3.3. Computational modelling – phase stability

The calculations suggest form II is marginally more stable than form I, but the difference in internal energies amounts to only 0.2 J mol^{-1}. When corrected for zero-point contributions this increased to 0.5 kJ mol^{-1}, while the inclusion of the thermal and entropic contributions at 20 K gave rise to a free energy difference of 0.4 kJ mol^{-1}. It was observed also that the harmonic free energies of the two polymorphs within the Γ- point model are comparable across a wide range of

temperatures, with the new form II appearing to be less stable at values in excess of 100 K. However, the energy difference is marginal across the range of temperatures studied (see Figure 6.18).

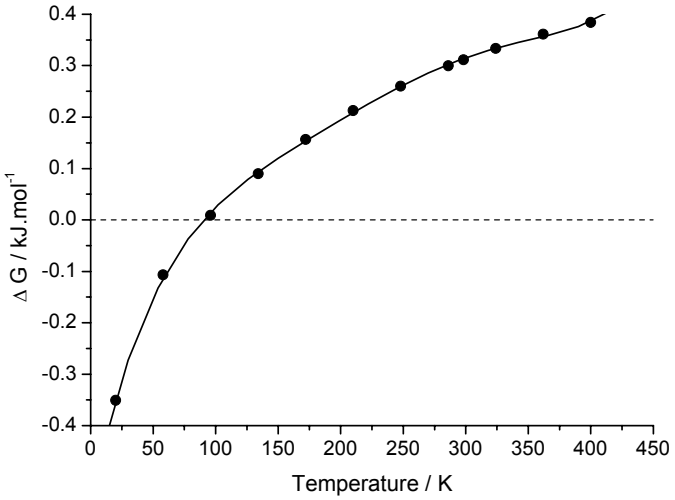

Figure 6.18. Plot of the variation of the difference ΔG=[G(form II)-G(form I)] in the Gibbs free energies of the polymorphs with temperature. Solid line shows a 5th order polynomial fit to the data.

6.5.3.4. Computational modelling – solid-state vibrational spectrum

The normal modes were calculated by lattice dynamics after successful geometry optimisations for both forms had been obtained. The primitive cells of the polymorphs contain two molecules, leading to a total of 84 normal modes in each lattice. Three of these modes correspond to acoustic motions, the frequencies of which tend toward zero at the Γ- point. Moreover, the presence of multiple molecules in the cells lead to the existence of modes composed of in-phase and out-of-phase combinations of near identical intramolecular motions. Each of these modes possesses a slightly different frequency, and the differences between them constitute the Davydov or factor group splitting (FGS).

Tables 6.6 and 6.7 contain the 36 frequencies computed for the intramolecular motions, along with the corresponding assignments, FGS magnitude, irreducible representations and IR and Raman activities. The identification of each mode was not straightforward; each assignment had to be made by visualisation of

the corresponding set of atomic displacements. The new assignments for form I were compared with those reported by Keuleers *et al.*[44] A similar analysis is provided for the low frequency modes in Table 6.8. However, strong coupling of the internal and external motions of the molecules renders the clear assignment of the latter modes difficult, and so only their symmetries, and IR and Raman activities are reported.

The frequencies calculated for form I 1,3-dmU generally overestimate the experimental values,[44, 56] but the average deviation amounts to less than 3 %. It is worth reiterating that this accuracy is achieved without resort to scaling. In the case of the four low frequency modes for which no experimental frequencies were available, comparison was instead made with the values calculated by Keuleers *et al.*[44] The agreement between the new solid-state frequencies and the values obtained from these earlier cluster calculations is less satisfactory. This is expected, however, as the lack of experimental data in this region will impact heavily on the earlier cluster calculation as they relied upon scaling to obtain meaningful comparison with the experimental data.

Turning now to the new assignments of the individual form I modes, it was found that the majority of them were in agreement with those made by Keuleers *et al.*[44] Notable differences emerge for three modes: the previous assignments δ C–O (704 cm^{-1}), τ_{as} C–N (674 cm^{-1}), and π_{as} N–H (132 cm^{-1})[57] are amended within the current study to τ_{as} C–N (731.8 cm^{-1}), coupled δ C–O/ρ_{as} CH_3 (702.7 cm^{-1}) and coupled τ_s N–R/π_s N–H (125.2 cm^{-1}), respectively (note that R represents the methyl group). Keuleers and co-workers[44] also ranked the individual components of the motion in each mode by their potential energy contribution. It was found that for the modes at 1509.2, 1464.4, 1225.3, 1206.9, 1163.7, 625.8, 153.0 and 138.9 cm^{-1}, the dominant components obtained from the present calculations do not appear to match those of the earlier study, but were nevertheless present as one of the secondary components.

The anharmonic corrections to the high frequency stretching modes amounted to -168 and -172 cm^{-1} for the symmetric and asymmetric N–H stretches respectively, and -110 cm^{-1} for the symmetric C–H stretch. It was not possible to treat the various ν_{as} C–H motions separately, and so the correction obtained for the totally symmetric mode was applied to all of the CH_3 stretches. The frequencies of the ν_s and ν_{as} N–H

modes are overestimated by 112–120 cm^{-1} in the harmonic approximation, while application of the anharmonic corrections leads to underestimation of the experimental values by some 50–60 cm^{-1}. The latter discrepancies are likely due to inaccuracies in the energies obtained from the B3LYP functional for N–H bond stretches beyond the equilibrium length. Previous studies have shown that the accurate representation of the donor-proton stretching potential requires the use of a hybrid functional containing an exact exchange component in excess of the 20 % applied here.[58] Meanwhile, application of the anharmonic correction to the various ν CH modes leads to frequencies that overestimate experimental values by small amounts in the range 30–40 cm^{-1}, thus markedly improving the agreement with experiment in the case of the donor-proton stretching vibrational modes.

So far no comparable experimental frequencies are available for the new form of 1,3-dmU, but the accuracy of the lattice dynamics approach in form I lends confidence in the form II values. It was found that there were only marginal differences in the frequencies of the two forms, in keeping with the fact that the two structures are distinguished only by the orientation of their hydrogen-bonded chains. The values in form II are generally slightly blue-shifted relative to form I, but the variations are generally 1 % or less of the latter values. The frequencies in which there are larger deviations occur at 713.1, 685.2, 601.4, 159.9, 128.6 and 112.4 cm^{-1}. These differences are often due to the fact that the modes occur in a different order in each form. For example, the δ C–O and τ_{as} C–N modes that appear at 713.1 and 685.2 cm^{-1} respectively in form II, invert to 702.7 and 731.8 cm^{-1} respectively in form I.

Given an experimental technique of sufficiently high resolution in the low frequency region, the τ_{as} C–N mode may find use as a convenient spectroscopic indicator of the structural form under investigation, as no vibration occurs in form I inside the range of 703–626 cm^{-1}. Furthermore, the blue shift of the higher frequencies could also prove to be another factor to distinguish the two forms.

Table 6.6. Calculated harmonic and anharmonic, and experimental[44, 56] frequencies, ω (cm^{-1}), mode assignments (IP indicates the in-phase FGS component, OP the out-of-phase component), irreducible representations, S, factor group splittings (FGS, cm^{-1}) and infrared (IR), Raman (R) activity of the normal modes of the form I 1,3-dmU crystal in the *Fdd*2 space group.

ω_{harm}	ω_{anharm}	ω_{exp}	Assignment [a, b, c]		S	FGS	IR	R
3468.7	3300.4	3357	ν_s N–H	OP	A_2	0.63	i	a
3454.8	3283.0	3335	ν_{as} N–H	IP	B_2	0.17	a	a
3130.8	3023.7	2994	ν_{as} CH_3	IP	B_2	0.95	a	a
3130.4	3023.3	2994	ν_s CH_3	IP	A_1	0.12	a	a
3092.7	2985.6	2947	ν_s CH_3	OP	A_2	7.69	i	a
3088.3	2981.2	2947	ν_{as} CH_3	OP	B_1	5.00	a	a
3035.7	2928.6	2904	ν_s CH_3	IP	A_1	2.40	a	a
3034.1	2927.0	2883	ν_{as} CH_3	IP	B_2	4.95	a	a
1653.4		1621	ν C–O	IP	A_1	3.08	a	a
1651.2		1595	δ_{as} N–H + ν_{as} C–N	IP	B_2	18.59	a	a
1589.8		1542	δ_s N–H	IP	A_1	0.64	a	a
1537.4		1480	δ_{as} CH_3	OP	B_1	12.98	a	a
1530.5		1477	δ_s CH_3	OP	A_2	15.98	i	a
1509.2		1453	δ_s CH_3	OP	A_2	21.93	i	a
1503.2		1445	δ_{as} CH_3	OP	B_1	14.87	a	a
1464.4		1438	δ_{as} CH_3	IP	B_2	3.47	a	a
1458.3		1422	δ_s CH_3	IP	A_1	4.84	a	a
1311.0		1273	ν_{as} C–N + δ_{as} N–H	IP	B_2	5.63	a	a
1225.3		1176	ν_s N–R	OP	A_2	1.20	i	a
1206.9		1138	ρ_s CH_3	IP	A_1	1.67	a	a
1175.4		1195	ρ_{as} CH_3	IP	B_2	3.63	a	a
1163.7		1165	ρ_{as} CH_3	IP	B_2	1.57	a	a
1155.6		1117	ρ_s CH_3	OP	A_2	2.15	i	a
1061.4		1042	ν_{as} N–R	OP	B_1	5.44	a	a
955.9		933	ν_s C–N + ρ_s CH_3	OP	A_2	1.55	i	a
788.8		776	π C–O	OP	B_1	1.74	a	a
731.8		674	τ_{as} C–N	IP	B_2	14.86	a	a
702.7		704	δ C–O + ρ_{as} CH_3	IP	B_2	3.87	a	a
625.8		505 [d]	τ_s C–N	OP	A_2	7.24	i	a
511.2		508	δ NCN	OP	A_2	1.78	i	a
346.7		351	δ_{as} N–R	IP	B_2	1.42	a	a
243.6		242	δ_s N–R	OP	A_2	1.34	i	a
169.1		199 [d]	π_s N–H + τ_s C–N	IP	A_1	2.65	a	a
153.0		136	τ_{as} N–R	OP	B_1	1.86	a	a
138.9		132 [d]	π_{as} N–H + τ_{as} N–R	IP	B_2	10.59	a	a
125.2		156 [d]	τ_s N–R + π_s N–H	IP	A_1	22.85	a	a

a – The attributed assignments correspond to the dominant motion at each frequency; where a mode comprises two or more component motions, they are presented in order of decreasing weight;
b – Intermolecular symmetrically equivalent positions were found based on the operator: *x+1/4; -y+1/4; z+1/4;*
c – R represents the methyl group;
d – Value calculated by Keuleers *et al*.[44]

Table 6.7. Calculated harmonic and anharmonic frequencies, ω (cm^{-1}), mode assignments (IP indicates the in-phase FGS component, OP the out-of-phase component), irreducible representations, S, FGS (cm^{-1}), and infrared (IR) and Raman (R) activity of the normal modes of the form II 1,3-dmU crystal.

ω_{harm}	ω_{anharm}	Assignment [a, b, c]		S	FGS	IR	R
3480.9	3313.1	ν_s N–H	OP	B_1	1.53	a	a
3466.9	3297.2	ν_{as} N–H	OP	B_2	1.16	a	a
3147.1	3039.0	ν_{as} CH_3	OP	B_2	3.59	a	a
3146.6	3038.5	ν_s CH_3	IP	A	3.08	i	a
3097.2	2989.1	ν_{as} CH_3	OP	B_2	1.84	a	a
3095.3	2987.2	ν_s CH_3	OP	B_1	0.05	a	a
3039.9	2931.8	ν_{as} CH_3	OP	B_2	5.63	a	a
3035.7	2927.6	ν_s CH_3	IP	A	1.53	i	a
1653.6		δ_{as} N–H + ν_{as} C–N	OP	B_2	26.90	a	a
1652.7		ν C–O + δ_s N–H	OP	B_1	4.67	a	a
1584.8		δ_s N–H	OP	B_1	0.68	a	a
1536.1		δ_{as} CH_3	IP	B_3	19.21	a	a
1534.7		δ_s CH_3	OP	B_1	18.48	a	a
1510.1		δ_s CH_3	OP	B_1	17.41	a	a
1496.3		δ_{as} CH_3	IP	B_3	16.37	a	a
1471.5		δ_{as} CH_3	IP	B_3	8.95	a	a
1464.2		δ_s CH_3	OP	B_1	3.45	a	a
1311.4		ν_{as} C–N + δ_{as} N–H	OP	B_2	7.80	a	a
1220.1		ν_s N–R	IP	A	0.89	i	a
1204.9		ρ_s CH_3 + ν C–O	IP	A	0.74	i	a
1173.9		ρ_{as} CH_3	OP	B_2	6.57	a	a
1164.8		ρ_{as} CH_3	IP	B_3	7.60	a	a
1160.6		ρ_s CH_3	OP	B_1	7.77	a	a
1057.9		ν_{as} N–R	IP	B_3	6.24	a	a
953.6		ν_s C–N + ρ_s CH_3	OP	B_1	3.59	a	a
785.2		π C–O	IP	B_3	0.40	a	a
713.1		δ C–O + τ_{as} C–N	OP	B_2	8.46	a	a
685.2		τ_{as} C–N + δ C–O	OP	B_2	10.45	a	a
601.4		τ_s C–N	OP	B_1	4.92	a	a
514.7		δ NCN	OP	B_1	2.46	a	a
346.7		δ_{as} N–R	OP	B_2	1.92	a	a
246.2		δ_s N–R	OP	B_1	1.28	a	a
184.7		π_s N–H	OP	B_1	10.59	a	a
159.9		τ_{as} N–R	OP	B_2	10.26	a	a
128.6		π_{as} N–H + τ_{as} N–R	IP	B_3	1.67	a	a
112.4		τ_s N–R	IP	A	3.98	i	a

a – The attributed assignments correspond to the major component at each frequency; where there is strong coupling of modes, the component motions are presented in order of decreasing weight;
b – Intermolecular symmetrically equivalent positions were found based on the operator: -x+1/2; y+1/2; -z;
c – R represents the methyl group.

Table 6.8. Frequencies, ω (cm^{-1}), irreducible representations, S, and IR and Raman activities (a=active, i=inactive) of the low frequency modes in both forms of 1,3-dmU.

Form I				Form II			
ω	**S**	**IR**	**R**	**ω**	**S**	**IR**	**R**
117.4	B_2	a	a	108.8	B_1	a	a
115.0	B_2	a	a	106.6	B_3	a	a
114.1	B_1	a	a	100.7	B_1	a	a
102.2	B_1	a	a	82.7	B_3	a	a
90.8	A_1	a	a	72.3	B_2	a	a
87.7	A_2	i	a	55.4	B_3	a	a
62.2	B_2	a	a	54.8	B_2	a	a
60.7	B_1	a	a	51.1	A	i	a
8.1	A_2	i	a	40.4	A	i	a

Finally, insight into the intermolecular interaction strengths was obtained from the examination of the N–H and H···O Mulliken overlap populations, obtaining values of 0.680 and 0.082*e* respectively in form I; and 0.682 and 0.086*e* respectively in form II.[54] It can therefore be concluded that the contribution of covalency to the hydrogen bonding interactions is similar in both forms. Furthermore, the similarity of the Mulliken charges on the N, H and O atoms, at -0.460, +0.284 and -0.529*e* respectively in form I; and -0.458, +0.278 and -0.531*e* respectively in form II, suggests that there is no appreciable difference in the electrostatic contribution in each structure.

6.6. Conclusions

The present chapter highlighted the difficulties of implementing crystal engineering as the co-crystallisations undertaken here did not follow exactly as designed. Nevertheless, this work has yielded previously unreported structures, one of which has even been expected for more than eleven years. To turn to each family of compounds studied, the conclusions are as follows.

From the attempted co-crystallisations of methyl-substituted ureas and squaric acid, two structures (**I** and **II)** were obtained. These showed different packing

motifs due to the location of the second methyl group (belonging to the urea compounds) and the subsequent steric effects and H-bond donating/accepting capabilities. However, at the intramolecular level the main characteristics of the two structures were maintained.

The 1:2 dihydrate of 2,2'-dimethyl-4,4'-bipyridine with oxalic acid was observed to differ from that of a previously reported structure where the base was bipyridine. The major differences resided in the fact that, as expected, the methyl substitution encouraged protonation of the heterocycle molecules. Furthermore, as seen in Chapter 4 where squaric acid and dimethyl bipyridine formed an adduct, the methyl substitution also led water molecules to be trapped in this crystal lattice in order to fill the voids created by the bulky methyl groups.

In the case of the 1:2 adduct of 4,4'-bipyridine with oxamic acid it was found that, as had been previously reported, the oxamate anion has the ability to form infinite aggregates that tend to be the dominate interaction. In the present study this resulted in the fact that the BIPY molecules served as fillers to cross-link the anionic scaffolding. Furthermore, the substitution of a hydrogen bond functionality (OH for a NH_2 group, when changing oxalic acid to oxamic acid) in the acid, affected the ratio of precursors and consequently the crystal packing. This in turn led to the existence of a bifurcated bond, instead of a "linear" bond, between the acid and the base.

The long anticipated 1,3-dmU polymorph, on the basis of the urea form I structure, has been found, characterised and compared with the previously known form. It has proven to be another interesting polymorph that was initially obtained by luck from the attempted co-crystallisation of N,N'-dimethylurea with phosphoric acid and *a posteriori* found to be available straight from the supplier. In practical terms this was only possible due to the technically advanced modern X-ray diffractometers that now enable data collection of smaller crystals. Despite this the most common crystallisation practice continues to be from solution, as it generally facilitates the growth of bigger and better crystals, but would have been counter-productive in this case as the solvent alone could have affected the outcome. The packing of the new form continues to be dominated by the bifurcated N–H···O hydrogen bonds that form 1-D structures, however, it differs from the known form due to orientation of these intermolecular hydrogen bonded chains assuming

alternating orientations. The approximate thermodynamics obtained from the Γ- point vibrational modes indicate that the two forms possess similar free energies. The vibrational spectrum of form I 1,3-dmU obtained from first principles lattice dynamics calculations in the reassigned *Fdd2* space group was in excellent agreement with the previous experimental data. While no experimental data currently exists for form II, comparisons with the normal modes of form I revealed only marginal differences, which was perhaps surprising given the striking change of chain orientation. However, on closer inspection, the similarities in molecular geometries naturally enforce a close agreement in the intramolecular vibrational modes for both forms. Furthermore, initial *in situ* crystallisation experiments at high pressure from the melt have indicated that a new form of 1,3-dmU may be obtained; thus further experiments under pressure should be pursued.

6.7. Bibliography

[1] C. B. Aakeröy, K. R. Seddon, *Chem. Soc. Rev.* **1993**, *22*, 397.

[2] G. R. Desiraju, *Curr. Sci.* **2001**, *81*, 1038.

[3] K. Sato, K. Seio, M. Sekine, *J. Am. Chem. Soc.* **2002**, *124*, 12715.

[4] A. H. Schmidt, *Synthesis* **1980**, *12*, 961.

[5] S. Cohen, S. G. Cohen, *J. Am. Chem. Soc.* **1966**, *88*, 1533.

[6] H. Li, J. Li, Y. Chen, *Sichuan Daxue Xuebao* **2000**, *37*, 408.

[7] H. Li, J. Li, Y. Chen, *Sichuan Daxue Xuebao* **2001**, *38*, 532.

[8] J. Gruenefeld, G. Zinner, *Arch. Pharm.* **1985**, *318*, 1062.

[9] W. Ried, U. Vitt, H. Dietschmann, *Liebigs Ann. Chem.* **1981**, 402.

[10] SAINT Area-Detector Software Package v7.01A, Bruker - AXS, Madison, Wisconsin, USA, **2003**.

[11] G. M. Sheldrick, SADABS v2.04, University of Gottigen, Germany, **2001**.

[12] A. Altomare, G. Cascarano, C. Giacovazzo, A. Guagliardi, *J. Appl. Cryst.* **1993**, *26*, 343.

[13] D. J. Watkin, C. K. Prout, J. R. Carruthers, P. W. Betteridge, R. I. Cooper, CRYSTALS v12 ed., Chemical Crystallography Laboratory, Oxford, UK, **2003**.

[14] M. T. Reetz, S. Hoger, K. Harms, *Angew. Chem. Int. Ed. Engl.* **1994**, *33*, 181.

[15] D. M. S. Martins, D. S. Middlemiss, C. C. Wilson, N. Shankland, W. G. Marshall, K. S. Knight, K. Shankland, S. Parsons, C. R. Pulham, C. A. Morrison, *manuscript in preparation*.

[16] J. A. Cowan, J. A. K. Howard, G. J. McIntyre, S. M.-F. Lo, I. D. Williams, *Acta Cryst. B* **2003**, *59*, 794.

[17] J. A. Cowan, J. A. K. Howard, G. J. McIntyre, S. M.-F. Lo, I. D. Williams, *Acta Cryst. B* **2005**, *61*, 724.

[18] A. P. Monkman, L.-O. Plsson, R. W. T. Higgins, C. Wang, M. R. Bryce, A. S. Batsanov, J. A. K. Howard, *J. Am. Chem. Soc.* **2002**, *124*, 6049.

[19] J. A. Cowan, J. A. K. Howard, H. Puschmann, I. D. Williams, *Acta Cryst. E* **2007**, *63*, 1240.

[20] T. Steiner, *Angew. Chem. Int. Ed.* **2002**, *41*, 48.

[21] pKa values of the respective conjugate acids of BIPY and dmBIPY were calculated using the ChemAxon Marvin pKa calculator. The difference between these calculated values was then added to the experimental value that has been measured for BIPY. Thus obtaining an estimate of the pKa for the conjugate acids of dmBIPY.

[22] http://www.chemaxon.com/demosite/marvin/index.html, (Ed.: Chemaxon), **2007**.

[23] R. I. Gelb, *Anal. Chem.* **1971**, *43*, 1110.

[24] G. D. Pinching, R. G. Bates, *J. Res. Nat. Bur Stand., Sect. A* **1948**, *40*, 405.

[25] C. B. Aakeröy, D. P. Hughes, M. Nieuwenhuyzen, *J. Am. Chem. Soc.* **1996**, *118*, 10134.

[26] P. S. Corbin, S. C. Zimmerman, P. A. Thiessen, N. A. Hawryluk, T. J. Murray, *J. Am. Chem. Soc.* **2001**, *123*, 10475.

[27] X. Zhao, Y. L. Chang, J. W. Lauher, F. W. Fowler, *J. Am. Chem. Soc.* **1990**, *112*, 6627.

[28] T. L. Nguyen, F. W. Fowler, J. W. Lauher, *J. Am. Chem. Soc.* **2001**, *123*, 11057.

[29] C. A. Morrison, M. M. Siddick, *Chem. Eur. J.* **2003**, *9*, 628.

[30] G. S. Papaefstathiou, L. Drakopoulou, S. P. Perlepes, C. P. Raptopoulou, A. Terzis, R. Keuleers, H. O. Desseyn, *Trans. Metal Chem.* **2003**, *28*, 548.

[31] N. Sklar, M. E. Senko, *Acta Cryst.* **1961**, *14*, 716.

[32] S. V. Deshapande, *Acta Cryst. B* **1968**, *24*, 1396.

[33] V. M. Coiro, P. Giacomello, E. Giglio, *Acta Cryst. B* **1971**, *27*, 2112.

[34] S. Stankovic, G. D. Andreetti, *Acta Cryst. B* **1978**, *34*, 3787.

[35] S. Coe, J. J. Kane, T. L. Nguyen, L. M. Toledo, E. Wininger, F. W. Fowler, J. W. Lauher, *J. Am. Chem. Soc.* **1997**, *119*, 86.

[36] B. P. Callahan, Y. Yuan, R. Wolfenden, *J. Am. Chem. Soc.* **2005**, *127*.

[37] S. Ganapathy, *Chem. Eng. World* **1998**, *33*, 110.

[38] S. Rainer, E. Heinz-Gerd, L. Leonhard, A. Sven, Germany, **2003**.

[39] A. Watanabe, Japan, **2007**.

[40] H. Mark, *Ber. Dtsch. Chem. Ges.* **1924**, *57B*, 1820.

[41] F. H. Allen, W. D. S. Motherwell, *Acta Cryst. B* **2002**, *58*, 407.

[42] J. Pérez-Folch, J. A. Subirana, J. Aymami, *J. Chem. Crys.* **1997**, *27*, 367.

[43] R. E. Marsh, *Acta Cryst. B* **2004**, *60*, 252.

[44] R. Keuleers, H. O. Desseyn, B. Rousseeau, C. Van Alsenoy, *J. Phys. Chem. A* **2000**, *104*, 5946.

[45] C. Spanswick, School of Chemistry and EaSTCHEM Research School, The University of Edinburgh, UK, Personal communication, **2005**.

[46] R. Dovesi, V. R. Saunders, C. Roetti, R. Orlando, C. M. Zicovich-Wilson, F. Pascale, B. Civalleri, K. Doll, N. M. Harrison, I. J. Bush, P. D'Arco, M. Llunell, CRYSTAL06, University of Torino, Torino, **2006**.

[47] A. D. Becke, *J. Chem. Phys.* **1993**, *98*, 5648.

[48] C. Lee, W. Yang, R. G. Parr, *Phys. Rev. B* **1988**, *37*, 785.

[49] R. Krishnan, J. S. Binkley, R. Seeger, J. A. Pople, *J. Chem. Phys.* **1980**, *72*, 650.

[50] H. J. Monkhorst, J. D. Pack, *Phys. Rev. B* **1976**, *13*, 5188.

[51] W. Koch, M. C. Holthausen, *A Chemist's Guide to Density Functional Theory*, Wiley-VCH, New York, **2000**.

[52] F. Pascale, C. M. Zicovich-Wilson, F. Lopez, B. Civalleri, R. Orlando, R. Dovesi, *J. Comput. Chem.* **2004**, *25*, 888.

[53] C. M. Zicovich-Wilson, F. Pascale, C. Roetti, V. R. Saunders, R. Orlando, R. Dovesi, *J. Comput. Chem.* **2004**, *25*.

[54] D. S. Middlemiss, Department of Chemistry and WestCHEM Research School, University of Glasgow, UK, Personal communication, **2007**.

[55] F. P. A. Fabbiani, C. R. Pulham, *Chem. Soc. Rev.* **2006**, *35*, 932.

[56] Y. Mido, M. Hiromu, *Bull. Chem. Soc. Jpn.* **1969**, *42*, 3372.

[57] Value calculated by Keuleers et al. as no experimental value was available.

[58] J. Poater, M. Sola, M. Duran, J. Robles, *Phys. Chem. Chem. Phys.* **2002**, *4*, 722.

CHAPTER 7

Final Conclusions and Future Work

During the course of this research, the phenomena of proton migration and proton transfer have been studied by experimental and computational methods. In the case of the longer hydrogen bonds (greater than 2.6 Å) proton transfer was seen to take place [*e.g.* in the adduct formed between squaric acid and bipyridine (SQBP)], whereas proton migration occurs in short, strong hydrogen bonds (SSHBs), [such as those seen in the adduct formed between dimethylurea and phosphoric acid (dmUPA)]. This research suggests, however, that a SSHB is not the only criterion required for proton migration. The underlying potential energy surface must be particularly sensitive to the crystal packing environment, such that when an external stimulus is applied the proton can migrate.

The following short sections summarises the results obtained during this work, and includes suggestions for further work.

Adduct of squaric acid with 4,4'-bipyridine

This system was highlighted some fourteen years ago and the study of the single-crystal to single-crystal phase transition that is induced *via* temperature has now been completed. In order to achieve this, a combination of various methodologies was applied. From these it was shown that this transition was

associated with proton transfer where the bipyridine molecules changed from monoprotonated to doubly protonated, which resulted in a change in colour from yellow to red. Variable pressure experiments were also pursued and showed that a similar colour change was observed, thereby indicating that proton migration might also be induced by pressure. It was concluded that the structures of the two new high-pressure forms were different from the high-temperature form, but all attempts to index the powder patterns of the new forms were unsuccessful. Future work would therefore involve the determination of these two high-pressure structures.

Co-crystals of squaric acid and 2,2'-dimethyl–4,4'-bipyridine

This system (SQdmBP) crystallised as two different red co-crystals that encapsulated water molecules. Both of the co-crystals contained doubly protonated dimethyl bipyridine molecules, which meant that the rationale of designing a proton transfer system where this phenomenon could occur at lower temperature than its parent structure (SQBP) was successful. However, it was found that substituting two H-atoms for methyl groups increased the basicity of the heterocycle to such an extent, that both protons remained on the heterocycle at all temperatures studied (down to 100 K). Future work would involve data collection at even lower temperatures, perhaps with the use of neutron diffraction. Furthermore, water was incorporated into these systems presumably to fill the voids caused by the bulky CH_3 groups. It would therefore be interesting to attempt these co-crystallisations in methanol and ethanol to discover whether other solvates could be obtained. Moreover, it would be interesting to co-crystallise squaric acid with monosubstituted bipyridine in an attempt to lower the basicity of the heterocyclic molecule.

Adduct of N,N-dimethylurea with phosphoric acid (dmUPA)

The design of this material followed on from the urea-phosphoric acid (UPA) adduct which has been shown previously to exhibit proton migration by theory and experiments. The new material system was found to crystallise as the 2:1 adduct and maintained the short, strong hydrogen bonds characteristic of the parent structure. However, unlike the case of UPA temperature induced proton migration was neither

observed in the experimental data nor in the theoretical calculations. It was postulated that this suppression was due to the fact that there were two molecules of dimethylurea interacting with one molecule of phosphoric acid and as a consequence the acidity of the phosphoric acid was reduced. Furthermore, the theoretical calculations showed that the difference in the crystal packing arrangement had a much stronger effect than the electronic factors in controlling proton migration. Future work would involve the study of this adduct under the influence of pressure as it seems possible that proton migration could occur. Furthermore, it would be extremely useful to prepare the 1:1 adduct of dimethylurea and phosphoric acid, as it should exhibit proton migration. Conversely, if the 2:1 adduct of urea and phosphoric acid was to be prepared, it seems likely that temperature-induced proton migration would not occur.

Exploratory systems

A series of co-crystallisation experiments were undertaken to engineer short, strong hydrogen bonds by systematically changing the nature of the acid and base. The following new structures were subsequently characterised:

- an adduct between oxalic acid and 2,2’-dimethyl-4,4’-bipyridine,
- an adduct between oxamic acid and 4,4’-bipyridine,
- dimethyl ureas fused to squaric acid, giving N-(2-hydroxycyclobutene-3,4-dione)-N’,N’-dimethylurea and N-(2-hydroxycyclobutene-3,4-dione)-N,N'-dimethylurea,
- a new polymorph of one of the precursors on its own (N,N’-dimethylurea).

The resulting co-crystallisations did not all follow the design quite as intended. They did, however, yield interesting new structures, some of which with the potential to be proton migration and transfer systems and for that reason were included in this thesis. For the future, variable pressure experiments of N,N’-dimethylurea are needed to characterise possible further new phases that were apparent in the preliminary work. Finally, the co-crystallisation of dimethyl bipyridine with oxalic acid from methanol and ethanol could explore the possible existence of new solvates.

Appendix A

Conferences and Courses Attended

Conferences:

- BCA[1] Spring Meeting
  Loughborough University, Leicestershire, UK, April 2005
  Poster presentation: Combined experimental and theoretical studies of solid-state proton migration

- XX Conference of the IUCr[2]
  Fortezza da Basso, Florence, Italy, August 2005
  Poster presentation: Experimental and theoretical studies of proton migration in the solid state

- 11th International Conference on the Applications of Density Functional Theory
  Université de Genève, Geneva, Switzerland, September 2005
  Poster presentation: Experimental and theoretical studies of proton migration in the solid state

[1] The British Crystallographic Association

[2] International Union of Crystallography

- IX Jornadas Nacionais de Química Industrial
  Universidade da Beira Interior, Covilhã, Portugal, March 2006
  Invited oral presentation: Combined experimental and computational studies of solid-state proton migration

- BCA Spring Meeting
  Lancaster University, Lancaster, UK, April 2006
  Poster presentation: Combining experiment and theory to study proton migration in the solid state

- ScotCHEM Computaitonal Chemistry Symposium
  University of St. Andrews, St. Andrews, UK, April 2007
  Poster presentation: Combining experiment and theory to study proton migration in the solid state

- 12th International Conference on the Applications of Density Functional Theory
  Universiteit van Amsterdam, Amsterdam, September 2007
  Poster presentation: The combined theoretical and experimental study of solid-state proton migration

Courses:

- Unix 1: An introduction to Unix, 2004
- Unix 2: Intermediate Unix, 2005
- HTML and Web Authoring, 2005
- Photoshop, 2005
- 10th BCA/CCG[3] Intensive Teaching School in X-ray Structure Analysis, University of Durham, Durham, UK, 2005
- Fortran 90, 2005

[3] Chemical Crystallography Group

- Unix 3: Shell Programming, 2005
- Dreamweaver, 2005
- CCP5[4] Summer School: The Computer Simulations of Condensed Phases, Cardiff University, Cardiff, UK, 2005
- Academic Paper Writing, 2006
- Thesis workshop, 2007
- Procter & Gamble Business Game, 2007
- Procter & Gamble Project Management Workshop, 2007

[4] Collaborative Computational Project 5 - The Computer Simulation of Condensed Phases

Appendix B

Publications

Temperature-induced Proton Transfer in the 1:1 adduct of Squaric Acid and 4,4'-Bipyridine.

Martins, D. M. S., Middlemiss, D. S., Pulham, C. R., Wilson, C. C., N., Shankland, Shankland, K., Marshall, W. G., Knight, K. S., Parsons, S., Morrison, C. A., *J. Am. Chem. Soc.* **2008** *submitted.*

A new polymorph of N,N'–dimethylurea characterized by X–ray diffraction and first principles lattice dynamics calculations.

Martins, D. M. S., Spanswick, C. K., Middlemiss, C., Morrison, C. A., Pulham, C. R., *manuscript in preparation for J. Phys. Chem. A.*

Towards understanding solid-state proton migration: the study of dimethylurea-phosphoric acid.

Martins, D. M. S., Morrison, C. A., Pulham, C. R., *manuscript in preparation.*

Towards understanding of solid-state proton transfer: the study of squaric acid-dimethyl bipyridine.

Martins, D. M. S., Parsons, S., Morrison, C. A., Pulham, C. R., *manuscript in preparation.*

Structure of ureas fused into the SQ ring: N-(2-hydroxycyclobutene-3,4-dione)-N',N'-dimethylurea and N-(2-hydroxycyclobutene-3,4-dione)-N,N'-dimethylurea.

Martins, D. M. S., Parsons, S., Morrison, C. A., Pulham, C. R., *manuscript in preparation for Acta Cryst. E.*

Structure of the 1:2 dihydrate of 2,2'-dimethyl-4,4'-bipyridine with oxalic acid.

Martins, D. M. S., Parsons, S., Morrison, C. A., Pulham, C. R., *manuscript in preparation for Acta Cryst. E.*

Structure of the 1:2 adduct of 4,4'-bipyridine with oxamic acid.

Martins, D. M. S., Parsons, S., Morrison, C. A., Pulham, C. R., *manuscript in preparation for Acta Cryst. E.*

Appendix C

List of Symbols, Terms, Abbreviations and Acronyms Used

1,3 dmU	N,N'-dimethylurea
B	Becke's 1988 exchange functional
B3	Becke's three-parameter hybrid functional
B3LYP	functional composed of Becker's three parameter exchange functional and LYP correlation functional
BIPY	4,4'-Bipyridine
BIPY-d_8	deuterated 4,4'-bipyridine
$BIPYH^+$	protonated form of 4,4'bipyridine
$BIPYH^{2+}$	diprotonated form of 4,4'bipyridine
BLYP	functional composed of Becker's exchange functional and LYP correlation functional
BSQB	bis(squaryl)biphenyl
BTA	1:2 adduct of benzene-1,2,4,5-tetracarboxylic acid with 4,4'-bipyridine
co-crystal I (chapter 4)	2,2'-dimethyl-4,4'-dipyridine-squaric acid-water, in ratio 1:2:2
co-crystal II (chapter 4)	2,2'-dimethyl-4,4'-dipyridine-squaric acid-water, in ratio 1:1:3

CSD	Cambridge Structural Database
∠	torsion angle (in degrees)
DAC	diamond-anvil cell
DFT	density functional theory
dmBIPY	2,2'-dimethyl–4,4'-bipyridine
dmUPA	adduct between N,N-dimethylurea and phosphoric acid
DSC	differential scanning calorimetry
E	energy
ESRF	European Synchrotron Radiation Facility
FGS	factor group splitting
GGA	generalised gradient approximation method of DFT
GTO	Gaussian type orbital
h	Planck's constant
H	Hamiltonian operator
HF	Hartree-Fock theory
HRPD	high-resolution powder diffractometer
HT	high temperature
I (chapter 6)	N-(2-hydroxycyclobutene-3,4-dione)-N',N'-dimethylurea
II (chapter 6)	N-(2-hydroxycyclobutene-3,4-dione)-N,N'-dimethylurea
ILL	Institut Laue-Langevin
IR	infrared (spectroscopy)
k_B	Boltzmann constant
LDA	local density approximation method of DFT
LT	low temperature
LYP	correlation functional developed by Lee, Yang and Parr
MD	molecular dynamics
MP	Monkhorst-Pack grid used for density sampling
NVT	type of MD simulation where the number of particles, volume and temperature are constant
OMABP	adduct between oxamic acid and 4,4'bipyridine
OXAdmBP	adduct between oxalic acid and 2,2'-dimethyl-4,4'bypyridine

p	momenta of a particle
PA	phosphoric acid
PBE	gradient corrected functional of Perdew, Burke and Ernzerhof
PDA	1:1 adduct of urea with pyridine-3,5-dicarboxylic acid
PES	potential energy surface
PW	planewave
PW91	functional developed by Perdew and Wang
r	interatomic distance
SCF	Self Consisten Field
SQ	squaric acid
SQ^{2-}	squarate di-anion
SQBP	squaric acid bipyridine adduct
SQBP-d_{10}	perdeuterated squaric acid bipyridine adduct
SQ-d_2	deuterated squaric acid
SQdmBP	squaric acid dimethylbipyridine adduct
SQdmBP	co-crystal of squaric acid and dimethyl bipyridine
SQH^-	hydrogen squarate anion
SQH_2	neutral squaric acid molecule
SSHB	short, strong hydrogen bond
STFC	Science and Technology Facilities Council
STO	Slater type orbital
T	temperature
τ	angle (in degrees)
UPA	1:1 adduct of urea with phosphoric acid
UV	ultraviolet (spectroscopy)
VT	variable temperature
XRD	X-ray diffraction
φ	phase of diffracted waves
Ψ	molecular wavefunction